

Nanoscale Advances

Accepted Manuscript

This article can be cited before page numbers have been issued, to do this please use: R. Rajeev, A. Varghese, M. Kaur, S. Garg and A. Nakai, *Nanoscale Adv.*, 2026, DOI: 10.1039/D5NA00936G.



This is an Accepted Manuscript, which has been through the Royal Society of Chemistry peer review process and has been accepted for publication.

Accepted Manuscripts are published online shortly after acceptance, before technical editing, formatting and proof reading. Using this free service, authors can make their results available to the community, in citable form, before we publish the edited article. We will replace this Accepted Manuscript with the edited and formatted Advance Article as soon as it is available.

You can find more information about Accepted Manuscripts in the [Information for Authors](#).

Please note that technical editing may introduce minor changes to the text and/or graphics, which may alter content. The journal's standard [Terms & Conditions](#) and the [Ethical guidelines](#) still apply. In no event shall the Royal Society of Chemistry be held responsible for any errors or omissions in this Accepted Manuscript or any consequences arising from the use of any information it contains.

Electrocatalytic Advancements with Trimetallic Nanoparticles: Design Strategies and Roadmap

Sonali Garg^{a†}, Aafreen Nakai^{b†}, Rijo Rajeev^{b*}, Anitha Varghese^{b*}, Manvinder Kaur^{ac*}

^aDepartment of Chemistry, Chandigarh University, Gharuan, Punjab-140413, India

^bDepartment of Chemistry, CHRIST University Bangalore, Karnataka- 560029, India

^cChitkara University Institute of Engineering and Technology, Chitkara University, Rajpura-140401, Punjab, India

[†] Equally contributed to the manuscript

Abstract

Trimetallic nanoparticles (TMNPs) have emerged as a versatile class of nanomaterials whose multifunctional and synergistic properties surpass those of mono- and bimetallic systems. This review examines the recent advancements in TMNP synthesis, bridging conventional top-down techniques with state-of-the-art bottom-up strategies that provide precise control over atomic ordering while addressing concerns related to sustainability. This review provides a systematic discussion of the structural and synthetic innovations resulting in their rapid adoption in electrochemical applications, including fuel cells, oxygen and hydrogen electrocatalysis, supercapacitors, and electrochemical sensing. Particular emphasis on the influence of interfacial and compositional engineering in TMNPs, ameliorating superior catalytic activity and stability over conventional catalysts, has been comprehensively highlighted. Finally, key challenges, including scalability, long-term stability, biocompatibility, and miniaturization, have been outlined for future opportunities for designing sustainable, application-oriented TMNPs. By linking fundamental structure–property relationships with electrochemical performance, this review contributes a unified framework for fabricating next-generation TMNPs towards energy conversion, catalysis, and advanced sensing applications.

Keywords Trimetallic nanoparticles, Functionalized Nanostructures, Electrocatalytic activity, Electrochemical Sensors, Fuel Cells, Supercapacitors



*Corresponding author Email address: rijo.rajeev@res.christuniversity.in (Rijo Rajeev); manvinder.2k50@gmail.com (Manvinder Kaur); anitha.varghese@christuniversity.in (Anitha Varghese)

Introduction

Trimetallic nanoparticles (TMNPs) have garnered widespread attention recently, given their notable applications in various fields such as cancer therapy/diagnosis, bioimaging, and catalysis.

¹ TMNPs are discrete nano-objects with cartesian dimensions less than 100nm, which possess distinct physical and chemical properties. TMNPs are produced using three different metals to reduce metal consumption, achieve atomic ordering, and customize the size and morphology of these NPs. ² The TMNPs catalysis is highly beneficial in several aspects, such as decreasing the concentration of carcinogenic chemical compounds formerly used in industrial and chemical compounds by a hefty percentage in a minimal contact time. ³ Compared to monometallic and bimetallic NPs, TMNPs have novel physiochemical features owing to their multifunctional and synergistic effects for various applications. TMNPs have found unique catalytic, active food packaging, biomedical, antimicrobial, and sensing applications; they preserve an ever-superior level of catalytic activities and selectivity compared to monometallic and bimetallic nanomaterials. TMNPs are produced using three different metals to reduce metal consumption, achieve atomic ordering, and customize the size and morphology of these NPs. ⁴ In various biomedical, antimicrobial, catalytic, active food packaging, and sensing applications, TMNPs have displayed improved catalytic selectivity/activity and efficiency. ⁵ In addition, three metals pave the way for various topologies and morphologies, including multishell, mixed structure, segregated subclusters, and core-shell. ⁶ By modifying the atomic distribution and surface compositions of multiple metals, TMNPs can be further designated as alloys and intermetallic NPs to adjust their catalytic performance. ⁶ Compared to monometallic and bimetallic NPs, TMNPs have novel physicochemical features because of their synergistic or multifunctional effects for various applications. A "top-down" or "bottom-up" approach is typically used to create and stabilize nanoparticle. ⁷ In the "bottom-up" approach, nanoparticles are created by self-assembling atoms into nuclei, which then grow into tiny particles. This method involves biological and chemical synthesis, whereas the top-down approach uses different physical and chemical processes for breaking bulk material into small particles. ⁸ The physical techniques for the top-down approach



include thermal ablation, milling, and grinding, while the chemical methods include chemical reduction, electrochemistry, and photochemical reduction. The physical techniques are more capital-intensive because they require high energy, resulting in low yield.⁸ Recently, chemical methods have become more popular because they require less energy during the formation and reduction steps. Moreover, they produce nanoparticles with high yield and high preciseness in shape and size.⁹ However, using several dangerous chemicals responsible for cytotoxicity, genotoxicity, and carcinogenicity makes chemical procedures environmentally hazardous.¹⁰ Due to toxicity, instability, and low biocompatibility, chemical techniques have been constrained to manufacture nanoparticles for biomedical applications.¹¹ Therefore, the current main emphasis of nanoparticle synthesis research is establishing an environmentally friendly approach that successfully controls the size, shape, stability, and properties of the synthesized NPs.¹²

Wang and colleagues, in their paper, tune the strain in Pt-Co-Zn TMNP for oxygen reduction reactions; however, the work fails to elucidate how the same structural combination works for various electrochemical reactions.¹³ Cheng and workers reported how chemical etching works as a post-synthetic technique to enhance the photocatalytic activity.¹⁴ Hashem et al explore the biosynthesis of TMNPs and related biological applications, but fail in explaining the mechanistic connection of green synthesis towards the surface chemistry of TMNPs.¹⁵ Merjan and colleagues showcased a green synthesis technique for lead removal via Fe/Cd/Cu TMNPs, but it fails to address the control of the topology of TMNPs.¹⁶ Despite the broad number of reviews and research papers on mono, bi, and TMNPs providing an independent view of choice of metals, catalytic performance and synthetic treatments, most existing works fail to provide a unified roadmap of structure-property relationship with catalytic functions. Hence, this review puts forth a streamlined discussion of firstly the mechanistic understanding behind several combinations of TMNPs. Secondly, we provide a thorough evaluation of synthesis methods (top-down, bottom-up up and green routes). Lastly, it provides a comparative study of existing works based on design, composition and catalytic activity. Therefore, we present a practical application-oriented framework that supports the rational design of TMNPs by combining these aspects.

Fig. 1(a) represents the number of articles published in journals by searching the keywords trimetallic nanoparticles, fuel cells, supercapacitors, electrochemical sensors, and electrocatalysis for water splitting using the logical operations “AND” in the Web of Science. The bar graph



represents the number of journal articles based on the electrocatalytic applications of TMNPs published since 2021.

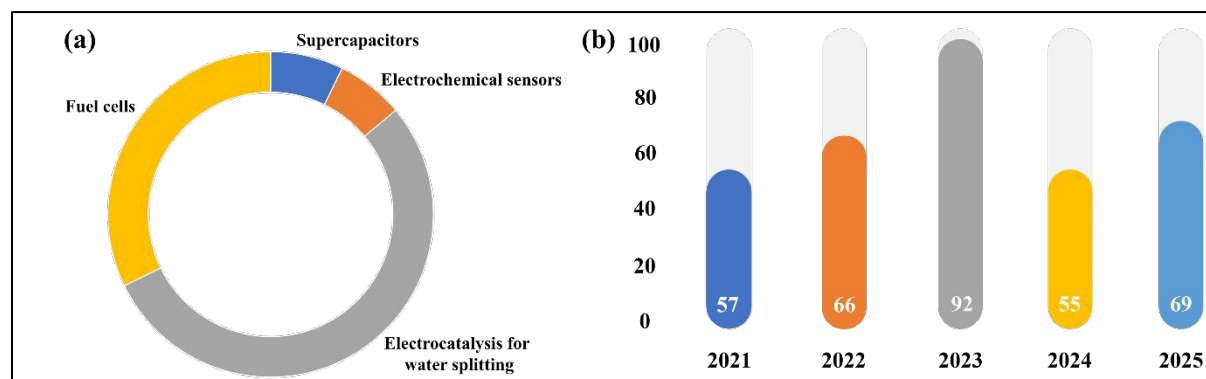


Fig. 1 – (a) Pie chart representation of articles in the past five years based on the electrocatalytic applications of TMNPs (By searching the keywords trimetallic nanoparticles, fuel cells, supercapacitors, electrochemical sensors, and electrocatalysis for water splitting using the logical operations “AND” (Web of Science). (b) A bar graph representing the number of articles published in journals involving TMNPs in the previous five years.

Evolution from Monometallic to TMNPs

TMNPs are now widely used in various catalytic processes and have attracted attention for their unique applications in catalysis.¹⁷ Compared to monometallic nanoparticles, TMNPs have higher catalytic activity, more selective detection and sensitivity, increased antibacterial activity, excellent stability, various morphologies, and chemical transformation.¹⁸ These properties are attributed to the synergistic doping of bimetallic and TMNPs in metals, which change their catalytic characteristics.¹⁹ Synthesizing metal nanoparticles using a biogenic or green synthetic method is extremely difficult. The template for creating metal nanoparticles is a polysaccharide hydrogel or sodium alginate hydrosol.²⁰ The synthesis of these multimetallic or alloy catalysts is mainly based on conventional preparation techniques, such as impregnation, mechanical alloying, melt spinning, hydrothermal preparation, microwave irradiation, co-reduction, and electro-deposition.²¹ Due to improved geometric effects, lattice strain, and electronic charge transfer, these synthesized multimetallic nanoparticles have shown to be suitable catalysts with greater chemical reactivity than their monometallic counterparts.²² The nature and selectivity of catalysis have been improved by adding another metal to bimetallic nanoparticles.²³ As a result, adding extra metals



to bimetallic nanoparticles has been noticed as a revolution in the increased catalytic process. The active reducing agents for the chemical synthesis of TNPs are hydrazine, oleylamine, trisodium citrate, triton X, N, N-dimethyl formamide (DMF), glucose, L-ascorbic acid, and formaldehyde. According to a prior study, alloy nanoparticles do not exhibit the same anticancer effect as core-shell nanoparticles.²⁴ By forming a hollow-like shape, the two phases of TNPs will boost their stability and dye-decolorizing catalytic activity.²⁵ Simultaneous and sequential metal reductions are helpful for synthesizing TNPs' core-shell/hollow-like structure throughout the synthesis process.²⁶ Additionally, many studies have been conducted on the fabrication and application of TMNPs. Due to the superior performance of TNPs compared to MNPs and BNPs, they are continuously in demand.^{25,27} Many TNPs, including Ag/Au/Pd²⁵, Au/Ag/Cu²⁸, and Pt/Ru/Co²⁹, have been chemically synthesized. In fuel cells, Pt@Fe@Ni trimetallic nanocatalysts increase oxygen reduction reaction (OER) activity compared to the Pt electrode catalyst³⁰. TMNPs such as Pt@Pd@Bi nanowires, Al₂O₃@Ag/Au core-shell, and Cu@Ni@Pt dendrites have been utilized to reduce 4-nitrophenol.³¹ Similarly, Zhang et al. discovered TMNPs of Au-Pt-Pd with significantly increased catalytic activity for glucose oxidation compared to monometallic and bimetallic nanoparticles.³² Compared to standard Pt/C catalyst, Matin et al. designed core-shell TMNPs of Pd/Co@Pt, which showed improved electrocatalytic performance in the ORR³³. Wang et al. synthesized trimetallic Ni@Au@Pd nanoparticles showed excellent performance against the dehydrogenation of formic acid.³⁴ Additionally, Tayal et al. found that the Ir@Pt@Sn electrocatalyst had more excellent activity for ethanol oxidation than the comparable bimetallic nanoparticles.³⁵ Similarly, Fe@Ag@Pd trimetallic nanocatalyst for formic acid degradation maintains its catalytic property after six applications.³⁶

Various Types of TMNPs

Pt-Based TMNPs

Pt Nanoparticles are already employed in the forthcoming generation of automotive catalytic converters because of their high surface area. As a result, using less platinum is needed to create them. Even though the Oxidation Reduction Reaction (ORR) kinetics are slow and result in energy loss, Pt-based materials are used to make the majority of critical electrodes.³⁷ The development and exploration of platinum-based materials for ORR are currently being pursued with significant



interest by researchers of electrode materials. Pt-based TMNP catalysts are created to improve the performance of Pt-based electrodes.³⁸ Core-shell-shaped catalysts are employed in catalytic applications, and they contain only trace quantities of platinum and palladium.³⁹ There are numerous methods now being utilized to make Pt catalysts for proton exchange membrane fuel cells (PEMFC) and direct methanol fuel cells (DMFC), including colloidal⁴⁰, micro emulsion⁴¹, impregnation, and others. The urea-burning preparation seems an innovative and promising way to quickly, easily, and at no expense obtain high-quality (nanosized) crystalline powders. In Pt-based catalyst research, adding another metal to the Pt catalyst might not merely reduce the use of the noble metal Pt and enhance the catalytic capacity.⁴²

Pd-Based TMNPs

Compared to pure palladium, palladium-based alloys have better hydrogen solubility and permeability. Pd-rich surfaces catalyze the hydrogenation reaction by dissociating H₂ and acting as a catalyst. Pd, though, is the most effective electrode for ORR in acidic media. Pd alloys of different bi- and trimetallic elements, such as Pd-Co, Pd-Fe, Pd-Cr, Pd-Co-Au, and Pd-Co-Mo, can increase activity.⁴³ Observedly, the rise in the ORR activity for Pd alloys has been reported, and many theories have been proposed to explain the increase in Pd alloy activity related to that of Pd.⁴⁴ The observed increase in the ORR activity of Pd alloys may be attributed to the electrical properties of Pd, such as Pt-alloys.

Ni-Based TMNPs

Among non-noble metals, Ni is the most common, and due to the synergistic interaction of Ni and Pd-Pt, the catalyst's stability and activity have improved.⁴⁵ The nickel, copper, and cobalt powder are widely used because of their excellent catalytic, magnetic, and electrical capabilities. As a result, research has determined that when two metals are combined to produce a trimetallic compound, the quality of the resulting material can be enhanced compared to that of hygienic metals. Due to its superior selectivity and catalytic mobility compared to monometallic nickel, the fabrication of Ni-based alloy nanoparticles has recently gained wide attention. Nickel-containing catalysts are the most widely utilized due to their inexpensive cost, quick turnover rate, and excellent stability.⁴⁶ Active sites can be found in nickel metal particles, accelerating carbon



deposition on material surfaces.⁴⁷ Nickel catalysts are less expensive than rhodium or palladium catalysts, which is advantageous for significant research and commercial applications.

Ag-Based TMNPs

The chemical purity of these catalysts is perfect, and they have a low bulk density in a particular area, resulting in a decrease in the catalyst's use for that specific process. A catalyst made of Ag helps produce formaldehyde from methanol and acetaldehyde from ethyl alcohol, among others. Due to their strong ORR activity and good methanol tolerance, Ag or Ni-based alloy catalysts have also been studied as cathode electrocatalysts in earlier research. It has been discovered that alloying Pt with Ag or Ni produces the best ORR activity. Ag can dramatically reduce the Gibbs free energy of the electron transfer stages in ORR for a multi-component alloy catalyst, enhancing ORR kinetics.⁴⁸

Cu-based TMNPs

The main technological problem for the fuel-cell-based hydrogen economy is the development of straightforward and reasonably priced heterogeneous catalysts for hydrogen release. This issue can be swiftly solved by developing novel techniques to synthesize Cu-based TMNPs.⁴⁹ Cu-based TMNPs were synthesized using a metal displacement plating method. Khan and coworkers showed the effective utilization of Cu-based Cu–Ag–Ir, Cu–Pd–Ir, and Cu–Ag–Pd TMNPs for effective hydrogen generation.^{4,50} This eccentric TMNPs combination in the literature supports high selectivity and increased catalytic activity. The as-prepared NPs demonstrated 100% hydrogen selectivity because of the high synergistic impact among the three metals. The composition of the middle and outer metal layers covering a Cu inner metal determines this catalytic activity of various materials.^{51,52} Compared to other TMNPs, Cu unprecedentedly displays superior selectivity towards hydrogen, excellent electrical and magnetic properties, and is economical for industry houses to operate with.⁴⁹



Various Methods for the Synthesis of TMNPs



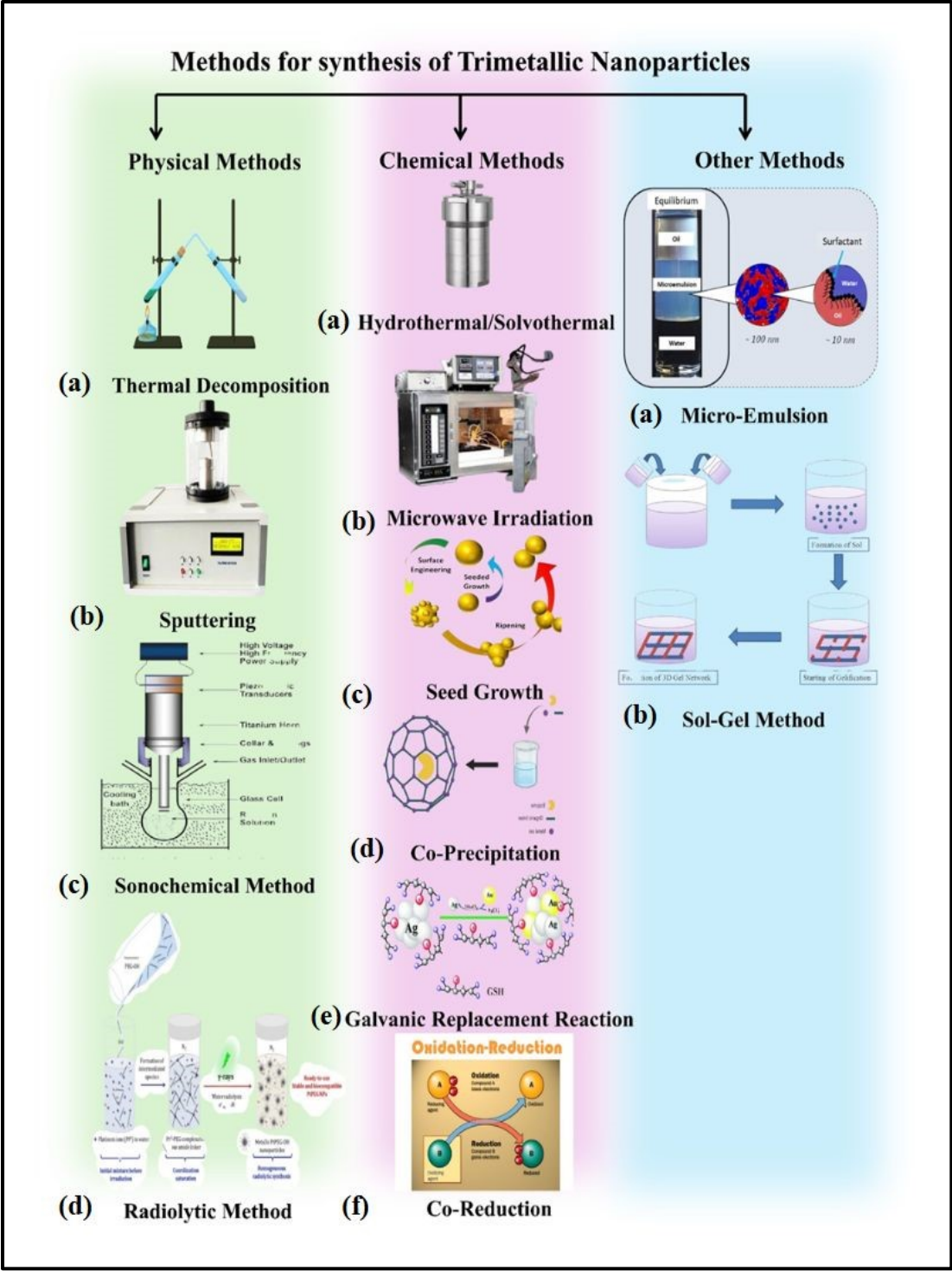


Fig. 2 Various Methods for the Synthesis of TMNPs are listed above, namely, under Physical methods (a) Thermal Decomposition, (b) Sputtering, (c) Sonochemical Method and (d) Radiolytic Method. Chemical methods include (a)Hydrothermal/Solvothermal synthesis, (b)Microwave

Irradiation, (c) Seed Growth, (d) Co-Precipitation, (e) Galvanic Replacement Reaction and (f) Co-Reduction, as well as Other Methods, including (a) Micro emulsion and (b) Sol-Gel Method.

Physical Methods-Based Nanoparticle Synthesis

The synthesis of multicomponent nanoparticles has not been thoroughly investigated or examined. Most investigations demonstrated that the synthesis of TMNPs is done using thermal heating techniques.⁵³ The synthesis method involves top-down and bottom-up approaches, physical methods come under the top-down approach.⁵⁴ This technique uses physical forces to break apart large materials into smaller molecules and eventually nanoparticles to produce high-quality and pure nanomaterials.⁵⁵ However, they are produced with low yields of around 20-30% because of the elevated pressure and temperature (>600-1200°C) requirements. Nanomaterials are synthesized using various physical techniques, including sputtering, thermal decomposition, sonochemical, and radiolytic methods, as shown in **Fig. 2**.⁵⁵ However, few studies have been reported on synthesizing TMNPs employing the methods above.

Sputtering

Sputtering involves bombarding the target metal with high energy to produce nanoparticles.⁵⁶ The three fundamental processes involved in atom beam sputtering are the migration of atoms from material surfaces, nucleation and formation of nanoparticles, and absorption onto another material in an electric field.⁵⁷ Using a high-rate vacuum coating process, magnetron sputtering includes sputtering in a magnetic field in which one or more materials are coated on the surface of another material, such as ceramics or metal.⁵⁸ This process can produce materials with a high degree of purity; however, controlling the shape of the nanoparticles consumes an excessive amount of energy.⁵⁹ Liu et al. explained the synthesis of PtTiMg alloy nanoparticles via a facile one-pot, three-target magnetron co-sputtering technique. The PtTiMg-30 nanofilms were uniformly deposited at room temperature on Toray carbon paper (TCP) substrates, forming a thin film of PtTiMg-30 alloy.⁶⁰ Zhu et al. synthesized CuPt/Ag TNPs via an aco-sputtering technique onto liquid PEG to evaluate ORR activity. The designed TNPs showed higher ORR performance than the corresponding bi- and mono-metallic NPs due to the synergic effect of incorporating a third metal.⁶¹ Despite sputtering being an excellent method to control the composition of the nanoparticles, the technique has some limitations, such as low scalability under high vacuum (>10-



3-10-6 Torr), very high energy consumption of power densities of (100-500 W) and also the usage of non-economical precursors such as Pt, Au which are comparably expensive than precursors used in most of the chemical methods.

Thermal Decomposition

The synthesis of NPs in this method is based on temperature, as transition metals requires a high temperature for synthesis because they are not stable at room temperature. The process begins with forming particles of the metal precursor, which have a low decomposition temperature, and later, the second metal precursor decomposes when the temperature is increased.⁶² This process is used to create crystals of high grade or crystals with a high commercial value. The primary drawbacks of this method include the need for extremely high temperatures and the challenge of isolating unstable NPs from the reaction at high temperatures.⁵⁹ Gao et al. designed a facile, low-cost, stable, and highly active nanocatalyst Pt₂Fe₃Ni₃/C for enhancing ORR performance in PEMFCs by the two-step reaction. The first step involved the addition of Fe and Ni metals on Pt-based NPs via the microwave-assisted polyol method, which further underwent a thermal annealing process at various temperatures. The designed nanocatalyst was stable and more durable than Pt/C, and it possessed more active sites due to alloying Pt metal with others.⁶³ Kahnamouei and Shahrokhian reported the synthesis of NiCoFe nanocatalyst with an open-cage/3D frame-like structure for OER. It was prepared by the sequential thermal treatment on the cage structure of CoFe Prussian blue (CoFe-PBA) under an argon (CoFeA-TT) atmosphere, followed by the electrochemical deposition of Ni-Co-sulphide (NiCo-S) nanosheets forming a shell layer on it. The electrochemical data indicated that the deposition of NiCo-S on CoFeA-TT (NiCo-S@CoFeA-TT) showed the best catalytic performance.⁶⁴ Although this technique produces high-quality crystals, there are several issues with regard to the scalability of this method, as it requires extremely high temperatures (300-800°C), and results in a moderate yield, owing to the volatility of the precursors.

Sonochemical Method

This method is based on an ultrasound technique that raises the pressure or temperature in the solution, forming small NPs. Hollow NPs can be produced by ultrasound by causing the formation or collapse of small bubbles in a solution. Moreover, the synthesis process of metal NPs is generally based on the generation of oxidizing and reducing radicals.⁶⁵ Elayappan et al. worked



on the ultrasonication-dry synthesis of gold (Au) NPs-supported copper ferrite (CF) on rGO(Au-CF@rGO). A modified Au-CF@rGO/GCE electrode was also created to conduct the electrochemical analysis to detect dopamine in banana milk samples.⁶⁶ Xie et al. successfully synthesized the PtAuRu nanostructures with perpendicular pore channels and extremely porous characteristics via a facile ultrasonic-assisted synthetic approach to improve the electro-oxidation of formic acid using ascorbic acid (AA) and PVP as a reducing agent and a stabilizer.⁶⁷ Basavegowda et al. synthesized FeAgPt alloy NPs via ultra-sonication techniques extracted from the roots of *Platycodon grandiflorum*. The NPs exhibited high catalytic action to reduce 4-nitroaniline to p-phenylenediamine.⁶⁴ This method stands to offer several advantages over the others: it's highly scalable due to the wide availability of sonochemical reactors, moderate operating temperatures are required, and the yields can reach up to 80%.

Radiolytic Method

Radiolytic synthesis explains how metal nanoparticles are synthesised using radiation. In this, the electron beam or gamma (γ) rays reduce metal ions in soluble precursors to produce metal NPs. The generated alloy NPs are not stable when formed by thermal breakdown. The amount of radiation used determines the type of alloy nanoparticle produced. A low dose can create nanoparticles made of core-shell alloys, whereas a more significant dose governs the formation of mixed alloy nanoparticles.⁶⁹ The radiolytic process has a challenge in controlling the form of the nanoparticles. Irradiation-based approaches, on the other hand, are inexpensive, environmentally friendly, and appear promising for use in large applications.⁶²

Among the processes mentioned above, the most facile way to synthesize TMNPs is via the sonochemical and radiolytic methods. While the former is a process that leads to the reduction of both employment of high temperatures and consumption of excessive amounts of energy, the latter proves economical and eco-friendly. On the contrary, sputtering and thermal decomposition are two techniques that accompany several drawbacks, including the challenge of isolating unstable NPs, using high temperatures, and consuming excessive amounts of energy.

Chemical Methods



The bottom-up approach is favorable and potent for the synthesis of the TMNPs, because of its scalability, simplicity, and low cost, which enables the building up of either atoms or molecules to form nanostructures using various approaches viz., galvanic replacement,⁷⁰ seed growth,⁷¹ hydrothermal,⁷² solvothermal,⁷³ co-decomposition,⁷⁴ photo-deposition,⁷⁵ microwaves,⁷⁶ microemulsions,⁷⁷ ultrasonic irradiation,⁷⁸ co-reduction,⁷⁹ coprecipitations,⁸⁰ and biological methods. The synthesis of nanomaterials by chemical synthesis involves reducing agents to reduce metal ions. Most of the stabilizing, reducing, or capping agents utilized in these chemical processes are toxic and unacceptable from green chemistry's perspective.⁷⁷ Moreover, a significant issue in chemical synthesis is the purification of the produced nanomaterial from the reaction mixture of the reagents and organic solvents.⁷⁸

Microwave (MW) irradiation

For the synthesis of TMNPs, the microwave (MW) dielectric heating approach is a quick and frequently used methodology. The morphology and size of the TMNPs can be easily adjusted using the MW heating process.⁷⁹ The MW irradiation technique is helpful as it produces uniform nucleation nanomaterial with a narrow size distribution and quick crystal growth by evenly heating the precursor materials to the reaction solution.⁸⁰ The MW technique is helpful in the synthesis of quality nanomaterial by reducing toxic organic solvents, side reactions, and chemicals with defined reaction parameters.⁸¹ Bi₂O₃-SrO-FeO@SiO₂ trimetallic NCs were synthesized to remove organic dyes from aqueous water via a simple MW approach in 3 minutes by switching the ON/OFF method. Further, the adsorption technique was used to remove dyes using the designed nanocomposite effectively, and the reusability of NCs was evaluated by studying six consecutive cycles.⁸⁶ Similarly, Au/Pt/Ag TMNPs were prepared by Yadav and the team using the MW irradiation approach via successive reduction. The mixture was heated in the oven for 4 minutes in cyclic mode with continuous 10s OFF and 20s ON. These NPs were further used to evaluate the antimicrobial activities.⁸⁷

Hydrothermal Method/Solvothermal Method



This method is used to prepare single crystals and involves the solubility of precursor minerals in the solvent at high pressure in an autoclave. The temperature gradient of the chemical process affects the growth of crystal formation. The hydrothermal approach has advantages over other crystal development processes due to its tendency to produce unstable crystalline phases at the melting point. This method is also frequently employed to grow large and high-quality crystals. Hydrothermal conditions have generated compounds from nearly all classes, comprising elements, tungstates, molybdates, carbonates, silicates, simple and complex oxides, and germinates. Usually, synthetic quartz, gems, and other materials are grown using hydrothermal synthesis. For instance, the MnNiFe alloy nanoparticles were prepared on reduced graphene using a one-pot hydrothermal approach for the electro-oxidation of urea. The designed nanocatalyst exhibited superior electrocatalytic properties compared to commercial Ni/C. the catalyst exhibited mass activity of $1753.97 \text{ mA mg}^{-1}_{\text{Ni}}$, which was 4.2 and 9.8 times better than Ni/rGO and Ni/C, respectively.⁸⁸ Safdar et al. synthesized a star-shaped CuMnCoO_4 via a hydrothermal approach, resulting in a promising energy storage device candidate. The CuMnCoO_4 contained bundles of orderly layer and loosely bound needles because of which the structure contained increased active sites which were responsible for the enhanced capacitance ($1,715 \text{ F g}^{-1}$ at 1 A g^{-1}) and excellent cycling stability as compared to mono- and di-metallic oxides.⁸⁹ Wang and co-workers synthesized hierarchical PtCoIr TNPs via a solvothermal method that was used for the detection of septicemia biomarkers in human serum.⁹⁰ Li and co-workers designed trimetallic Ni-Co-Mn fluoride supercapacitors synthesized by a solvothermal approach.¹ These SCs resulted in the formation of high-performance aqueous electrochemical energy storage systems.⁹¹

Co-precipitation method

Co-precipitation is among the most accessible and popular techniques for synthesizing TMNPs with regulated sizes and magnetic characteristics in various forms, including hydroxides, oxides, sulfides, carbonates, formates, citrates, and oxalates. In this technique, the oxo-hydroxide is precipitated using aqueous salt solutions such as chlorides or nitrates in an inert atmosphere. A quick nucleation burst begins when the solution reaches a critical concentration, after which the growth phase begins. Depending on the desired crystal size, different bases, such as NaOH and KOH at $(\text{C}_2\text{H}_5)_4\text{NOH}$, at room temperature, are used to create magnetite TMNPs. The ratio of agglomeration also supports the production of mesoporous structures. This method does not



require high temperatures or pressure, so it is the most preferable method among researchers, and even the impurities are removed just by washing. Tyagi and co-workers designed Al-substituted MnFe_2O_4 -based ternary oxide on rGO via a simple hydrothermal technique after co-precipitation, which showed outstanding ORR activity compared to commercial Pt/C.⁹²

Co-reduction method

Co-reduction is a straightforward process that can be used to design mono-, bi-, and TMNPs as well as multi-metallic NPs. The two metal precursors and the stabilizing agent are first mixed in a suitable solvent, leaving the transitional metals in their ionic forms. Then, the reducing agent is introduced to change them into zerovalent states. However, light transitional metals experience less reduction because of their lower reduced capacity. These mild transition metals are unstable because they readily oxidize when present in their zerovalent forms. Several techniques have been developed to create transition metal NPs because these metals are essential in catalysis. When compared to thermal decomposition, the co-reduction process has milder reaction conditions. No harmful organic solvents are employed, and the reaction occurs at low temperatures and in an air atmosphere.⁵⁸ Ravichandran et al. fabricated the trimetallic ordered mesoporous nanostructure (OMNs) using KIT-6 as a surfactant via chemical reduction method by using NaBH_4 as a reducing agent for enhancing MOR performance.⁹³ Similarly, Peng et al. used a facile two-step co-reduction approach for the synthesis of trimetallic PtPdCr nanoparticles with minimal platinum loading (5 wt%) supported on Vulcan carbon (PtPdCr/C), which showed improved methanol oxidation activity in acidic medium.⁹⁴ Elsheikh et al. synthesized trimetallic PdAgNi NPs on carbon support via a co-reduction technique using borohydride as a reducing agent.⁹⁵ The TNPs exhibited enhanced EOR activity compared to mono- and bi-metallic NPs.

Seed Growth

The NPs prepared using the seed growth method involve the preparation of seed (nucleation) followed by subsequent growth. The TMNPs created utilizing the seed growth approaches have a high yield and narrow size. By using this technique, core-shell types of nanostructures are formed. The core (seed metal) reduction potential is greater than the layer and shell metal reduction potentials during the synthesis of the TMNPs, employing the seed growth approach to avoid a galvanic reaction.⁹⁶ Using the seed growth technique, well-defined multi-metallic nanostructures



of 1D and 2D have been created.⁹⁷ Ahmed et al. designed AgAuPd ternary core-shell nanostructures for water treatment application via the seed growth method using sodium alginate as a reducing agent. These TMNPs were used to degrade methyl blue (MB). The TMNPs had the highest MB degradation rate constant compared to monometallic Ag and bimetallic Ag-Pd nanostructures.⁹⁸ PdCuIr NCs were synthesized by Chen et al. via the seed-mediated growth method for the oxidation of glycerol and ethylene glycol (EG). The designed NCs exhibited enhanced durability and mass activity compared to standard Pd/C. The heightened electrocatalytic activity was due to the addition of Cu and Ir atoms on the Pd surface.⁹⁹

Galvanic replacement Reaction (GRR)

The GRR method uses the change in reduction potential at a moderate temperature between the replaced and replacing metals, decreasing the homonucleation of independent NPs.^{100,101} The GRR approach is generally used to generate hollow multi-metallic structures, core-shell or hybrid, using one metal NP as a template, followed by the reduction and deposition of other metals with higher reduction potentials on the template. Qui et al. designed the trimetallic PtAuAg nanotubes via GRR at 75 °C for a methanol oxidation reaction (MOR). In this, Ag NRs were used as a precursor, followed by the response with H₂AuCl₄ or H₂PtCl₆. Further, a part of Ag was galvanically replaced by Pt or Au, which resulted in the formation of PtAg, AuAg, or PtAuAg alloy shell, which was carried out because of the variations in reduction potentials.¹⁰² Another reported work illustrates the formation of trimetallic (Pt-Pd-Co/rGO/GCE) via GRR for the oxidation of EG.¹⁰³ The reduction potential of Co was less than Pt and Pd, so it undergoes GRR, resulting in the formation of desired Nanocatalysts.

Among the chemical methods mentioned above, the most preferred methods are co-precipitation and seed growth. Co-precipitation requires moderate temperature and pressure, yielding controlled-sized transition metal nanoparticles (TMNPs). Seed growth produces nanoparticles of sufficient size, ensuring high yield and durability. In contrast, co-reduction is underutilized due to uneven reduction rates and instability in transition metal oxidation. In terms of scalability, galvanic replacement and seed growth are less scalable due to high precursor costs and multistep processes, respectively. However, Hydrothermal/Solvothermal and co-reduction are scalable. The



Hydrothermal/Solvothermal method can make use of industrial autoclaves with higher volumes (>5L) and higher yields up (70-90%).

Sol-Gel Method

Compared to other physical and chemical approaches, the sol-gel method helps produce metal oxide NPs at low temperatures. As the name suggests, this technique is based on the condensation reaction followed by the hydrolysis of organometallic compounds in an alcoholic medium, which converts a solution into a gel. The sol-gel approach has great potential for controlling the kinetics of the reaction as well as the surface properties of the oxides. Besides this, it enables easy compositional changes, the introduction of many functional groups, and adjustable microstructure. This process can be carried out easily at low temperatures.¹⁰⁰ Various TMNPs have been prepared using this approach.¹⁰¹ The $\text{Co}_3\text{O}_4\cdot\text{CdO}\cdot\text{ZnO}$ -based tri-metallic oxide NPs (CCZ) were prepared by the sol-gel method for sensing methanol in a buffer solution. The sensor showed an ultra-low detection limit of 32.8 ± 0.1 pM, a wide linear range of 1.0 nM–2.0 mM, and an excellent sensitivity of $1.3842 \mu\text{A} \mu\text{M}^{-1}\text{cm}^{-2}$ in just 11 s.¹⁰⁶ Gonçalves et al. designed NiVCe-layered double hydroxide NPs, which were synthesized by the sol-gel method, and the designed material turned out to be the best electrode material for sensor applications, OER, and hybrid supercapacitors. The NiVCe- LDH NPs had shown promise as a material for hybrid energy storage electrodes, delivering a specific charge of 740 C g^{-1} at 10 A g^{-1} and charge storage of 68.7% at 100 A g^{-1} .¹⁰⁷ Although this method results in a yield with good purity but it has an inherent limitation, which is that the gel ageing can hinder scale-up processes.

Micro Emulsion

In its most basic form, the micro-emulsion method comprises three elements: a small droplet (dispersed phase), an immiscible solvent (continuous phase), and a surfactant that covers the droplet. There are many different forms of micro-emulsions, including water-oil, oil-water, and water-Triton X-100, depending on the characteristics of the dispersed phase, continuous phase, and hydrophilic-lipophilic balancing value of the surfactant. The metal nanoparticles are formed inside droplets that can be modified for composition and size, and this technique has been broadly used to synthesize bi- and TMNPs. Overall, in terms of scalability, this method produces low-volume output and requires costly surfactants.



Electrocatalytic applications of TMNPs

With the rapid increase in population and thus an increase of energy demand, which led to the absence of traditional fossil fuels and the rise of pollutant emissions, the requirement of new clean and cheap energy sources in place of fossil fuels has become a vital problem.¹⁰⁸ The world population is expected to grow by 26% to around 9.7 billion by the year 2050, whereas primary energy consumption will increase by almost 50%¹⁰⁹. So, to limit the use of fossil fuel, hydrogen was measured as a clean and sustainable fuel that has high calorific value and does not leave any harmful side products on heating¹¹⁰. Hydrogen gas is considered a perfect source of clean energy for the future due to its high energy density and pollution-free benefits.¹¹¹ The most efficient ways to limit fossil fuel use on a big scale are fuel cell oxidations, water electrolysis¹⁰³ refer Table 1, or supercapacitors¹¹² see **Fig. 3**.



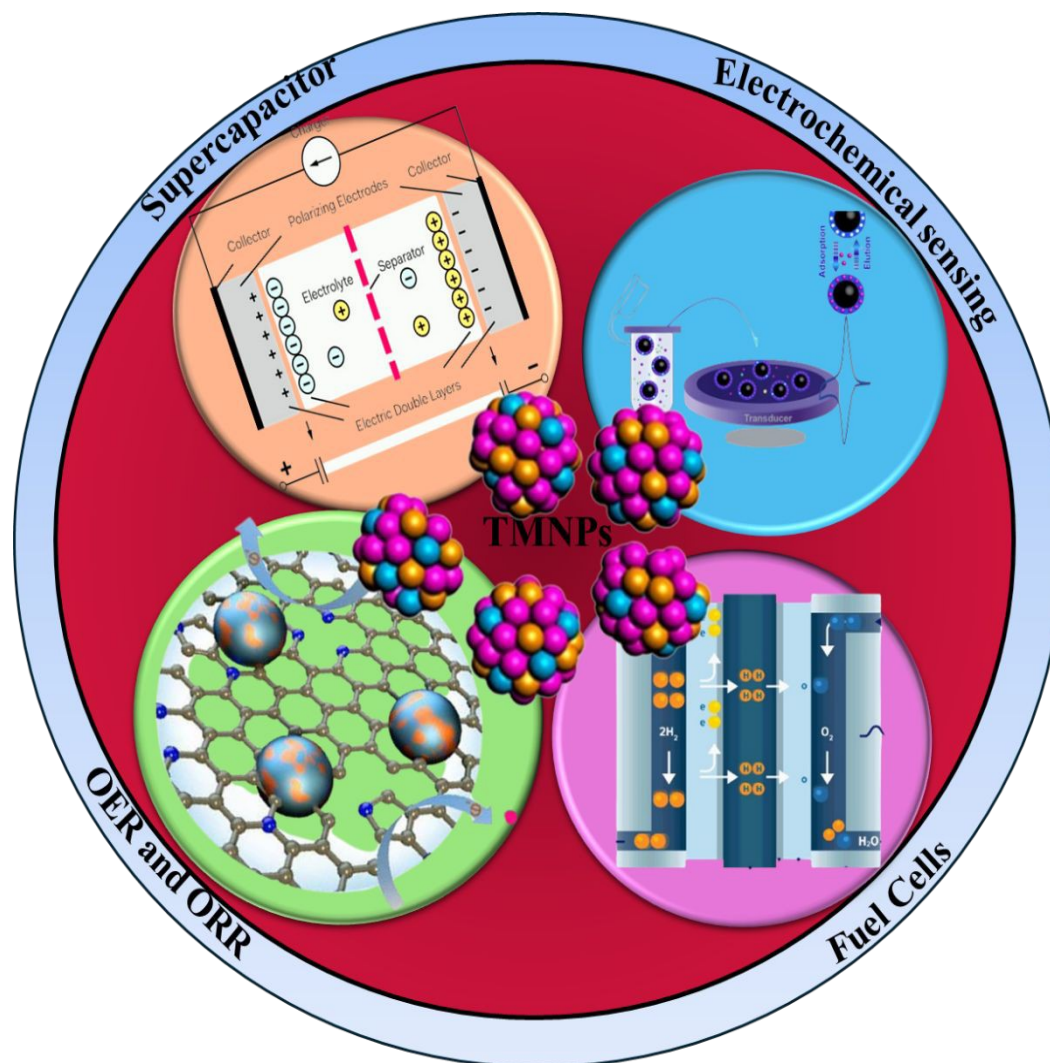


Fig. 3 Different electrocatalytic applications for TMNPs.

Fuel Cell-based applications

A fuel cell is one of the eco-sustainable technologies that can replace fossil energy resources.¹¹³ Because of their high energy density, low environmental impact, and high efficiency, fuel cells have received much attention from the engineering and scientific communities.¹¹⁴ Fuel cells generate electricity through the electro-oxidation of hydrogen or tiny molecules like formic acid, methanol, ethanol, and EG.^{114,115} To improve fuel cell performance, recent investigations on the hydrogen-fueled proton exchange membrane fuel cells (H₂-PEMFC) and direct alcohol fuel cell



(DAFC) technologies have been conducted in-depth. The DAFC reaction occurs at the anode, while the PEMFC reaction occurs at the fuel cell cathode. However, several issues concerning the effectiveness of fuel-cell systems still haven't been resolved.¹¹² However, the expensive and low-efficient catalyst is a substantial obstacle to the broad commercial use of fuel cells.¹¹⁷

Direct Alcohol Fuel Cell

The most popular active components in the research of DAFC anode catalysts are Pt or Pt-based materials¹¹⁸ severely restricted by low reserves and poor toxicity resistance.¹¹⁹ A recent study observed that the electro-catalytic activity of Pd and Pd-based materials is similar to that of Pt, which has around 50 times more reserves than Pt on Earth.¹²⁰ The synergistic effects of the multi-metallic alloys are indeed promising methods for enhancing the oxidation resistance and catalytic performance of metal Pd in the electro-oxidation of alcohol. This approach not only alters the physicochemical and electrochemical properties of the designed nanocatalysts but also enhances the electrocatalytic ability of oxidation of alcohols¹²¹ as explained by bi-metallic Pt-Pd¹²¹ and Pd-Sn¹²², tri-metallic Pd-Au-Ag¹²³, Pd-Ru-Bi¹²⁴, Pt-Pd-Co¹²⁵, and Pd-Ni-Au.¹²⁶

Formic Acid Electrooxidation

Direct formic acid fuel cells (DFAFCs) are receiving more attention among fuel cells because they have a higher theoretical open-circuit potential (1.48 V) and produce a higher yield than direct methanol fuel cells (DFMC) (1.18 V) and hydrogen-oxygen fuel cells (1.23 V).¹²⁷ As a result, developing an electrocatalyst with high activity for the electro-oxidation of formic acid is essential. DFAFCs are, therefore, very promising.¹²⁴ It is a prevalent belief that formic acid electro-oxidation occurs via two distinct mechanisms. These are the indirect (dehydration) and direct (dehydrogenation) pathways. Dehydrogenation is the favored method for formic acid electrooxidation because CO species are highly adsorbed on the electrode and close to the catalyst's active sites in the first pathway.¹²⁹ Recently, several nanocatalysts have been designed to improve the direct oxidation pathway, including modified Pt nanocrystals and Pd-based alloys.¹³⁰ Mainly, Pt-based nanocrystals have made remarkable developments in direct oxidation activities by surface modification and shape engineering.¹³¹ However, their utilization is limited because of the high cost of Pt, less natural abundance, and tendency to form poisonous CO as an intermediate at the anode.¹²⁸ Due to these reasons, investigating highly effective electrocatalysts with excellent



electrocatalytic activity and endurance has become a significant research topic. One of the most widely used approaches to improve their electrocatalytic performances while also lowering the cost of Pt is to alloy Pt with different transition metals, like Au¹³³, Ag¹³⁴, Cu¹³⁵, and Ru¹³⁶. Xie et al. successfully synthesized the PtAuRu nanostructures with perpendicular pore channels and extremely porous characteristics via a facile ultrasonic-assisted synthetic approach to enhance the electro-oxidation of formic acid using ascorbic acid (AA) and PVP as a reducing agent and a stabilizer⁶⁷. The resulting PtAuRu nanocrystals with the highly optimized atomic ratio exhibited improved electrocatalytic performance toward the FAOR with the SA and MA of 14.5 mA cm⁻² and 1044.1 mA mg⁻¹, which were 2.2 and 4.1 times higher than that of standard Pt/C, respectively. It exhibited the highest ECSA 7.2 m²g⁻¹ value compared to Pt/C and other mono- and bi-metallic nanoparticles. This catalyst can be used for industrial purposes because it demonstrates higher performance towards FAOR than standard one. Li et al. used a simple one-pot approach to prepare the defect-rich dendritic Pd₅₉Cu₃₀Co₁₁ nanoalloy, which was used to design high-performance non-Pt nanocatalysts for ORR and FAOR. The designed Pd₅₉Cu₃₀Co₁₁ nanoalloy exhibited SA towards FAOR, and ORR was 9.06 mA cm⁻² and 0.90 mA cm⁻², which were 4.04 higher in the case of FAOR than Pd black and 16.1 and 3.76 times higher than Pt/C.¹²⁶ The MA towards FAOR and ORR was 5.32 Amg⁻¹_{Pd} and 0.38 Amg⁻¹_{Pd}, 13.6 and 3.1 times higher than Pd black and 15.2 and 3.45 times higher than standard Pt/C. The designed nanoalloy represented more durability towards FAOR as after 10.000 cycles, the standard Pt/C catalyst showed a loss of MA by 72.7%, whereas the designed catalyst represented zero loss. This increase in performance was due to the presence of a defect-rich dendritic structure. Ulas et al. designed PdAgNi/C nanocatalysts via the NaBH₄ reduction approach by different atomic ratios for DFAFC.¹³⁷ It had a maximum current density of approximately 1.92 times greater than Pd/C's. Compared to Pd/C, the MA of Pd₇₀Ag₂₀Ni₁₀/C was 428.3 mA/mg Pd, which increased by 21.7 times. The insertion of Ag metal to Pd increases the electrocatalytic activity by increasing the synergistic effect between the two metals. The designed catalyst possesses long-term stability and higher electrocatalytic activity for an extended period. Intermetallic PtSnBi nanoplates with adjustable compositions, comprising Pt₄₅Sn₃₄Bi₂₁, Pt₄₅Sn₂₅Bi₃₀, and Pt₄₇Sn₁₆Bi₃₇, were synthesized by Luo et al. to boost formic acid electro-oxidation.¹³⁸ These nanoplates significantly outperformed binary PtSn and PtBi intermetallic while taking advantage of the coadjuvant effects of the selected three metals. The intermetallic Pt₄₅Sn₂₅Bi₃₀ nanoplates were designed via a simple wet-chemistry method, which was based on



the thermal decomposition of bismuth acetate [Bi(act)₃], stannous chloride (SnCl₂), and platinum acetylacetonate [Pt(acac)₂], in the mixture of octadecene (ODE) and oleylamine (OAM). The delicately constructed ordered PtSnBi nanoplates exhibited noticeably increased activity and selectivity toward the direct oxidation pathway due to repeated complexing-reducing-ordering operations carried out in a single step. In particular, atomically organized Pt₄₅Sn₂₅Bi₃₀ nanoplates display a record-breaking mass activity (MA) of 4394 mA mg⁻¹_{Pt}, which was 39 times higher than Pt/C and retained 78% of the initial activity even after 4000 potential cycles, making it a cutting-edge catalyst for the oxidation of formic acid.

The PdPtAu/CNT catalyst has not yet been studied, even though several trimetallic Pd-based catalysts were employed to evaluate their effectiveness for formic acid electrooxidation. Ulas et al. in PdPtAu/CNT nanocatalysts via the NaBH₄ reduction method.¹³³ X-ray diffraction (XRD) and N₂ adsorption-desorption techniques were implemented to characterize the designed catalysts. The effectiveness of the catalysts for FAOR was assessed by using electrochemical impedance spectroscopy (EIS), cyclic voltammetry (CV), linear sweep voltammetry (LSV), and chronoamperometry (CA) techniques. Pd₇₅Pt₅Au₂₀/CNT demonstrated a current density of 36.8 mA cm⁻² and MA of 1909.8 mA mg⁻¹_{Pd} in acidic media, improving its utility as a promising anode catalyst for DFAFC. Zhang et al. fabricated nanotwin-rich PdCuW trimetallic nanochains using a modified polyol method for formic acid electro-oxidation, as shown in **Fig. 4**.¹³⁹ The considerable lattice mismatch between Pd, Cu, and the newly introduced W was connected with the formation of nanotwin crystalline defects. It was found that the nano twins might serve as excellent active sites to boost the peak current density of formic acid oxidation significantly. Additionally, the Cu and W-tailored PdCuW nanochains alter the electronic structure of Pd by lowering the charge-transfer resistance with sufficient binding energy, leading to heightened improvement in catalytic activity. It possessed the lowest Tafel slope of 132.2 mV/dec compared to standard Pd/C (192.6 mV/dec). The MA and SA of the formed nanocatalyst were 2250 and 2750 mA mg⁻¹, the highest compared to the corresponding mono- and bi-metallic NPs. Compared to PdCu NCs, PdCuW NCs exhibited 1.3-fold higher electrochemically active surface area (EASA) and 1.8-fold higher oxidation peak current density because of nanotwin crystalline defects on PdCuW.



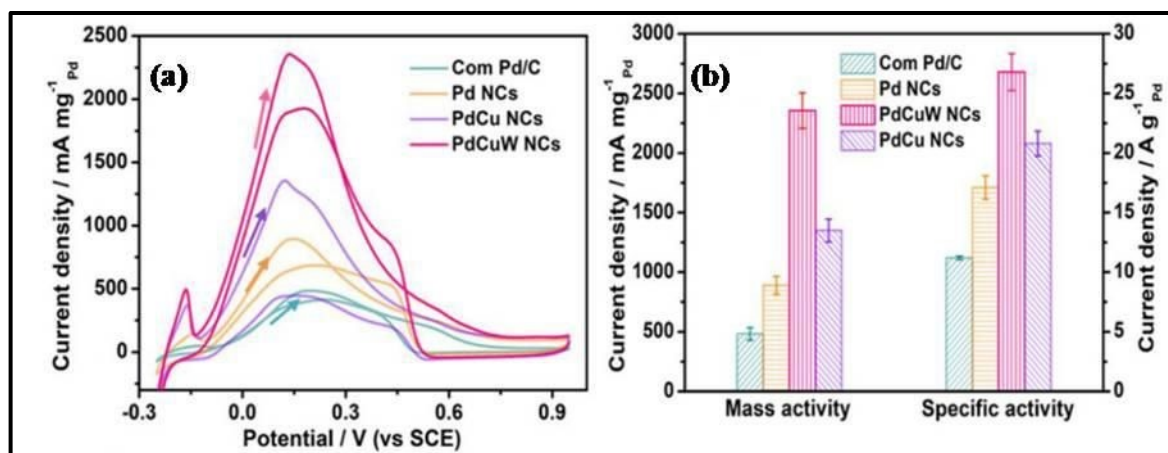


Fig. 4 (a) CV curves of Pd-based catalysts measured in 0.5 M H₂SO₄ + 0.5 M HCOOH solution. (b) Activity comparisons at peak potentials. This figure has been adapted/reproduced from ref 135 with permission from Elsevier, copyright 2020.

Pei et al. reported the development of ultra-low Au (0.075 wt%) decorated PtNi alloy nanoparticles on carbon (Pt_{10.9}Au_{0.2}Ni_{88.9}/C trimetallic catalyst) for the FAOR and MOR in an acidic medium, see **Fig. 5**.¹⁴⁰ The Pt_{10.9}Au_{0.2}Ni_{88.9}/C trimetallic alloy nano-catalyst was produced at room temperature by facile hydrazine hydrate reduction reaction and galvanic replacement reaction without the addition of any surfactants. The ECSA and MA of Pt_{10.9}Au_{0.2}Ni_{88.9}/C towards MOR were 38.52 m² g⁻¹ and 3.44 mA/ mg_{PtAu} and the SA of the catalyst towards MOR was 1.21 folds more than Pt/C, whereas the ECSA, MA, and SA of Pt_{10.9}Au_{0.2}Ni_{88.9}/C towards FAOR were 75.3 m² g⁻¹, 3.44 mA/ mg_{PtAu}, and 4.54 mA/ mg_{PtAu} respectively. In comparison to Pt_{11.1}Ni_{88.9}/C, Au_{11.1}Ni_{88.9}/C, and standard Pt/C, the Pt_{10.9}Au_{0.2}Ni_{88.9}/C trimetallic nanocatalyst displayed improved stability, activity, and anti-toxicity towards the FAOR and MOR.



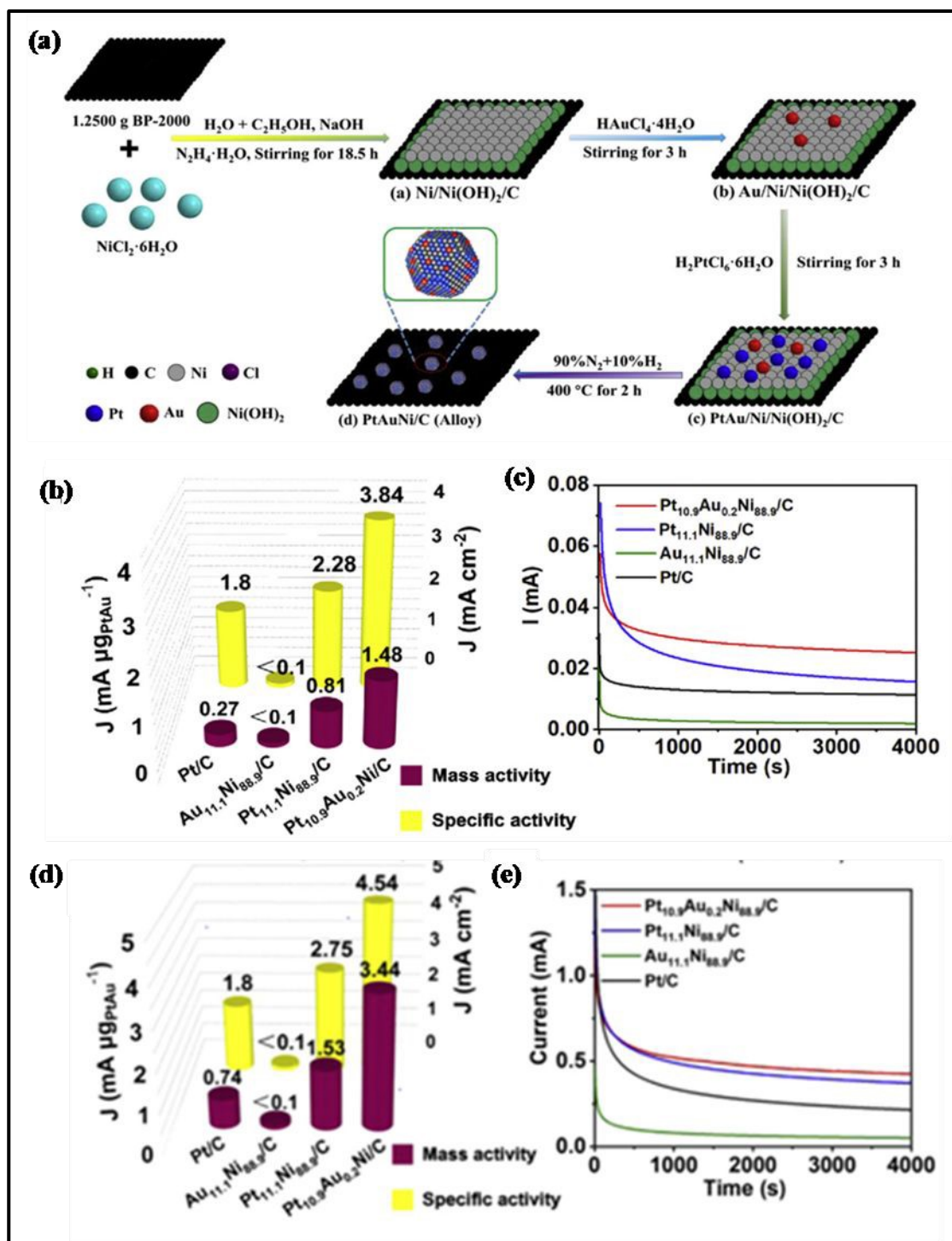


Fig. 5 (a) The systematic route for the synthesis PtAuNi/C-Pt_{10.9}Au_{0.2}Ni_{88.9}/C; (b) MA and SA towards MOR; (c) chronoamperometry at 0.75 V for MOR; (d) MA and SA towards FAOR; (e) chronoamperometry at 0.75 V for FAOR. This figure has been adapted/reproduced from ref 136 with permission from Elsevier, copyright 2020.



Hu et al. reported the fabrication of Ru@Au-Pt trimetallic core-shell nanoparticles to study the synergic effect for enhancing formic acid electro-oxidation.¹⁴¹ The trimetallic used in this study was formed via sequential ethanol reduction. Further research based on the Williamson-Hall method demonstrated that the shell thickness and Au/Pt atomic ratio cause an evident variation in the CO binding energy and microstrain of Ru@AuPt nanoparticles. In contrast, the catalytic activity for the electrooxidation of formic acid showed a linear dependence on the microstrain. The SA and MA of Ru@Au-Pt catalysts were 4.14 mA cm⁻² and 1.2 A mg⁻¹, 17 times and 52 times more than Pt/C.

Another work reported that the combined effects of both strain and electronic effects induced by alloying lead to further refinement of the reaction pathway, which can result in higher catalytic activity and efficiency of PtFeNi. Upon calculation of the lattice compressibility employing XRD and further correlation with XPS binding energy shift and DFT adsorption energy for quantification of the relative contributions of strain (77.4%) and electronic effects (22.65%) was revealed.¹⁴² PtCoZn trimetallic catalyst with adjustable Pt strain have shown to improve catalytic performance towards ORR, which is reported to be comparable to current state-of-the-art Pt-based alloy catalyst systems. The compressive strain in Pt would weaken the binding strength of oxygen in intermediates and lead to an enhancement in ORR activity, which was majorly induced by the incorporation. Similarly, doping of Co suppresses Zn leaching and would enhance PtCoZn stability via anchoring Zn atoms inside inner layers of the alloy particles.¹⁴³

Ethanol Oxidation Reaction (EOR)

A crucial recent approach in the research field is the direct introduction of ethanol into the fuel cell anode.¹³⁸ As ethanol is inexpensive, renewable, easy to transport, and has a high current density, the researchers are particularly interested in studying the ethanol electro-oxidation reaction.¹⁴⁴ Additionally, it has a lower probability than methanol of crossing the anode-to-cathode membrane. In contrast, it is less harmful than methanol, and forming direct ethanol fuel cells (DEFCs) represents a viable research objective.¹⁴⁵ Despite these benefits, there are still limitations associated with the production of DEFCs, including the lack of Pt reserves.¹⁴¹ Due to improved reaction kinetics, the ability to use a less-or-noble metal catalyst, and a less corrosive environment, using an alkaline medium instead of an acidic one has shown benefits for the overall fuel cell efficacy and cost-effectiveness.¹⁴⁷ An inert support material with a high surface area is typically



needed to produce the fuel cell catalyst to scatter the small metal nanoparticles and increase the reaction area. The most often researched support materials are carbon-based, such as graphene, nanofibers, and Vulcan carbon.¹⁴⁸ Pd is mainly used to prepare DEFCs as it is almost three times greater than Pt in the earth's crust and less poisonous. Among the different transition metals, Ni, Sn, Ir, Au, and Cu are the different metals that can enhance the electrocatalytic activity of Pd towards EOR.¹⁴⁹ Even with the benefits of having two metals in a bimetallic system, there is still plenty of room for improvement in performance and cost-effectiveness in the case of DEFCs for widespread utilization. Therefore, some researchers have explained the need for a trimetallic catalyst to increase the use of Pd towards EOR.¹³⁷ It has been demonstrated that adding Ir¹⁵⁰ or Ni¹⁴⁵ as a cocatalyst to Pd/C is highly advantageous for EOR as shown in Table 1.

Lv et al. designed a simple one-pot solution-phase method for the synthesis of uniform nanostructures and monodisperse sub-100 nm trimetallic PdAgCu mesoporous nanospheres (MNSs) using DODAC (dioctadecyldimethylammonium chloride) as a surfactant. Further, they evaluated their size dependency on EOR.¹⁵¹ The resulting Pd-based MNSs were precisely tailorable in terms of elemental ratios and compositions (PdAgPt, PdAgCu, PdPtCu, PdAgFe, and PdCuRu) as well as size (from 21 to 104 nm). For instance, in the electrocatalytic EOR, trimetallic PdAgCu MNSs with just an average size of 36 nm showcased the best MA of 4.64 A mg⁻¹_{Pd}, which was 1.1-1.7 times higher than that of MNSs with larger or smaller sizes and 5.9 times more than that of commercially available Pd black catalyst. Thus, this method offered a simple yet effective way to assess the size effect of trimetallic MNSs in electrocatalytic performances. Castagna et al. fabricated a carbon-based PtCuNi electro-catalyst to study the effect of surface composition and structure on EOR in an acidic medium.¹⁵² The required electrocatalysts were prepared via a two-step reaction route, which involves the simultaneous reduction of the copper and nickel in the presence of the reducing agent NaBH₄. Pt further replaced them with the partial galvanic replacement of the electroactive surface areas of each as-prepared electrocatalyst range from 93 to 117 m² g⁻¹. The two catalysts that performed the best for the EOR were the alloy nanomaterial with a Pt_{36.8}:Cu_{57.0}:Ni_{6.2} surface atomic ratio and the pseudo-core-shell material with a Pt_{18.0}:Cu_{43.6}:Ni_{38.4} surface atomic ratio. Compared to a commercial PtRu/C catalyst, these nanostructured catalysts had reduced onset potentials, fourfold greater mass activities (MA), and 8–10 tenfold higher specific activities in the case of EORs. Almeida et al. designed core-shell catalysts, Pd-Ni and Pd-Ni-Rh, in an alkaline medium by successively reducing Ni, Pd, and Rh



metallic chlorides with NaBH_4 to study the improved catalytic property due to an increase in synergic effect between metal and core-shell catalysts Pd-Ni-Rh on EOR. ¹⁵³ This study briefly explained the increase in catalytic activity towards EOR by adding Ni and Rh on the Pd/C catalyst. The $\text{Ni}_{20}@\text{Pd}_{60}\text{Rh}_{20}/\text{C}$ catalyst exhibits current densities that were revealed to be 9.3 times higher than those of the Pd/C catalyst, according to chronoamperometric experiments. Even after 2000 voltammetric cycles, the loss of active area in Ni@PdRh/C catalysts was just 17.5%, while in standard Pd/C catalysts, it was 51.5%.

Ren et al. used a straightforward one-pot solvothermal approach in an alkaline medium to create 3D star-shaped PdPtNi nanostructures (NSs) with spiky surfaces to enhance the catalytic activity for EOR, see **Fig. 6**. ¹⁵⁴ The surfactant PF-127 significantly influenced the NSs' morphology in this reaction system. The PdPtNi NSs for EOR had a peak mass activity (MA) and current density of 1195.81 mA mg^{-1} and 206.93 mA cm^{-2} , respectively. These values were much more significant than those of Pt black catalysts and binary NPs.

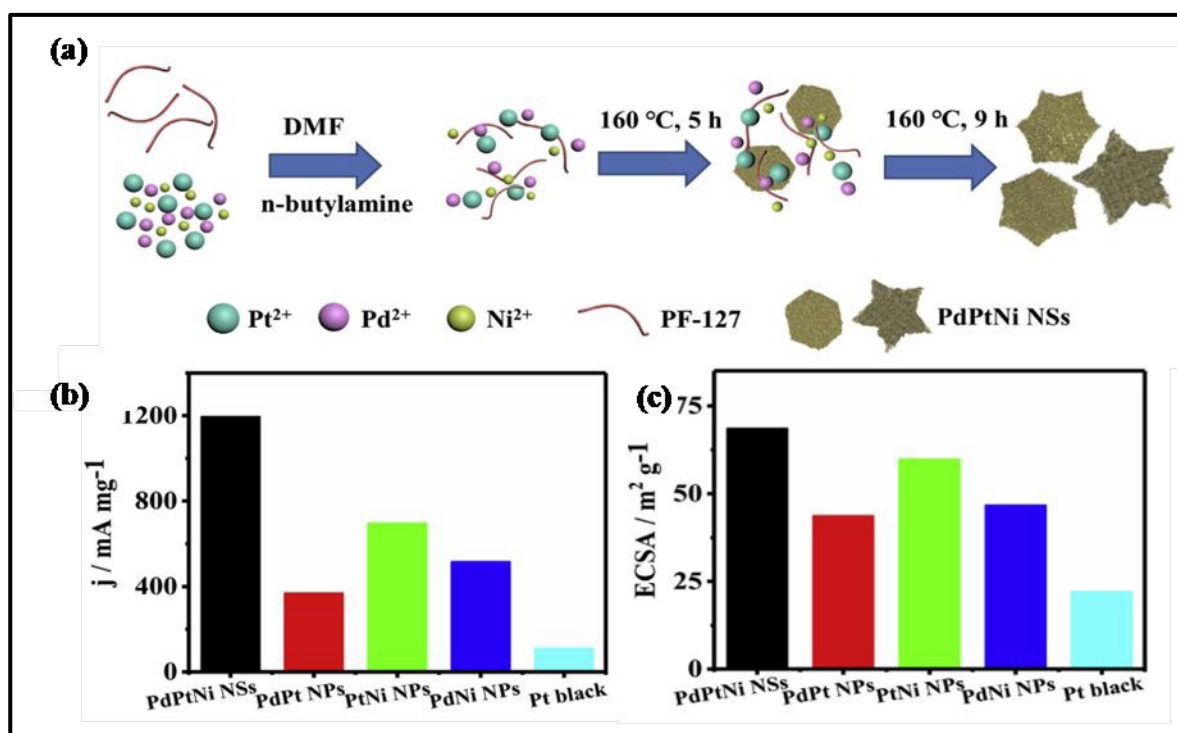


Fig. 6. (a) Synthesis procedure for star-like PdPtNi NSs; (b) histograms of MA for EOR in an alkaline solution for different PdPtNi NSs; (c) histograms of ECSA values for different PdPtNi



NSs. This figure has been adapted/reproduced from ref 149 with permission from Elsevier, copyright 2020.

Song et al. fabricated PdCu-SnO₂ nanowires and PdCu alloy nanowires in an alkaline medium via galvanic replacement synthesis method to study their enhanced effect on EOR compared to the standard Pd/C catalysts.¹⁵⁵ The designed PdCu-SnO₂ nanowire catalysts displayed an MA of 7770.0 mA mg⁻¹ and ESCA-normalized activity of 27.21 mA cm⁻², which were 7.6- and 5.8-times higher than that of Pd/C catalysts towards EOR. This was due to their one-dimensional structure, advanced PdCu/SnO₂ interface, electronic effect, and rough surfaces with non-homogeneous edges. The electrochemical experiments showcased that the SnO₂ was added to the PdCu/SnO₂ interface, thereby promoting ethanol oxidation at a lower potential and accelerating Pd-COads (Adsorption) oxidation via SnO₂-OHads to restore the active sites. Yang et al. explained the synthesis of trimetallic SDS-modified Pt/Ti₃C₂Tx nanocatalyst by two-step reaction procedures for evaluating EOR activity.¹⁵⁶ Firstly, the Ti₃C₂Tx nanocatalyst was prepared using an etching method; further, a solution of Pt was added to form Pt/Ti₃C₂Tx. In the second step, SDS acts as a surfactant, which was added to the mixture to limit the formation of aggregation of Pt nanoparticles. The electrochemical properties of SDS-modified nanocatalysts were evaluated both in acidic and essential mediums. The ECSA of 100-SDS- Ti₃C₂Tx/Pt was 9.02 m²g⁻¹. This is explained by the increased number of active sites for electrochemical reactions caused by the more excellent dispersion of catalyst NPs on the surface of Ti₃C₂Tx with more SDS surfactant. Liu et al. explained the synthesis of PtTiMg alloy nanoparticles via a facile one-pot, three-target magnetron co-sputtering technique.⁶⁰ The PtTiMg-30 nanofilms were uniformly deposited at room temperature on Toray carbon paper (TCP) substrates, forming a thin film of PtTiMg-30 alloy. The ECSA of the formed catalyst was 239.5 m²g⁻¹, which was around 3.5 times better than that of Pt/C (67.5 m²g⁻¹). The structure showed improved stability and durability in acidic media and retained 91% of its properties after 3000 cycles. The distinctive structure of the PtTiMg-30 alloy was responsible for better electrochemical performance than commercially available pure Pt.

Methanol Oxidation Reaction (MOR)

DMFCs are incredibly promising power sources for portable electronic devices and electric vehicles because they can be conveniently acquired, offer convenient fuel storage, and produce



minor environmental damage. ¹⁵⁷ Pt is typically regarded as the most effective MOR catalyst. ¹⁵⁸ However, platinum's widespread use is restricted due to its high price and ease of poisoning. As a result of the generation of intermediates amidst the oxidation reaction of methanol, Pt catalysts lose catalytic activity and stability. ¹⁵⁹ Pt is alloyed with less expensive metals, including Cu, Co, Zn, Ni, and Fe, to create PtM alloys for addressing the abovementioned limitations. ¹⁶⁰ Due to potential synergistic effects in Pt-based alloy nanostructures, PtM alloys not only improve the MOR activity and stability but also contain the use of less precious metals. ¹⁶¹ One of the best methods is to design bimetallic or trimetallic Pt-based alloy nanocatalysts by doping with other noble and transition metals. These results in the formation of Pt-Rh¹⁶², Pt-Co¹⁶³, Pt-Ir¹⁶⁴, Pt-Pd¹⁶⁵, Pt-V¹⁶⁶, Pt-Fe¹⁶⁷, Pt-Ni¹⁶⁸, Pt-Ru-Fe¹⁶⁹ and Pt-Pd-Co¹⁷⁰ systems demonstrating excellent electrochemical properties towards MOR.

Li et al. presented an effective technique for the direct synthesis of tri-metallic PtPdAu mesoporous nanoparticles (PtPdAu MNs) for MOR and ORR, which was achieved by simply heating the reaction mixture's aqueous solution to 40 °C for 4 hours. ¹⁷¹ The PtPdAu MNs were synthesized using AA as a reducing agent and F127 as a surfactant. According to calculations, the ECSA of the PtPdAu MNs towards MOR was 55.2 m² g⁻¹, which was higher than that of PtPd MNs (38.8 m² g⁻¹) and Pt/C (53.8 m² g⁻¹) catalyst respectively. PtPdAu MNs had a peak current density of 1.29 mA cm⁻², which was approximately 2.22 and 1.43 times greater than Pt/C catalyst (0.58 mA cm⁻²) and PtPd MNs (0.90 mA cm⁻²) towards MOR. The designed trimetallic PtPdAu MNs had an MA of 1.01 mA g⁻¹_{Pt}, which was higher than that of Pt/C catalyst (0.42 mA g⁻¹_{Pt}) and PtPd MNs (0.40 mA g⁻¹_{Pt}) for MOR. The MOR performance of the designed trimetallic (PtPdAu MNs) was also better than that of a few published Pt-based trimetallic catalysts, such as Au@PtPd mesoporous spheres (0.415 mA μg⁻¹_{Pt})¹⁷², mesoporous PtPdRu (0.249 g⁻¹_{Pt})¹⁷³ and nanoporous PtPdCu structures (0.43 mA g⁻¹_{Pt}). ¹⁷⁴ It also represents the enhanced ORR performance with a tafel slope of 66.8 mV/dec, which was near to that of Pt/C (66.9 mV/dec) and also possessed the greatest E_{onset} as compared to corresponding bimetallic and Pt/C. The enhanced properties were due to the combination of mesoporous nanoparticles and TMNPs. Luo et al. designed CoAuPd nanocatalysts using a classical successive reduction method using NaBH₄ as a reductant and P123 as a protectant for MOR and ORR. ¹⁷⁵ The catalyst showed enhanced MOR properties during dealloying and ORR properties after dealloying. The obtained results demonstrate the existence of two different super three-dimensional (3D) structures in the trimetallic CoAuPd nanocatalysts: the



unique nanocluster structures and nano-thornbush. The improved electrocatalytic activity of the designed nanocatalyst was attributed to the electrochemical dealloying process, which was responsible for increased active reaction sites, catalytic activity, and ECSA areas MOR and ORR. The CoAuPd nanocatalysts had a specific activity (SA) of 3.63 times and 2.37 times higher and an MA of 3.78 times higher and 2.86 times higher than commercial Pd black and Pd/C catalysts for MOR. In contrast, in the case of ORR, the dealloyed CoAuPd nanocatalysts had SAs that were respectively 1.506 and 1.180 times greater than those of commercial Pd black and Pd/C catalysts and MAs that were 1.304 and 1.229 times more significant than commercial Pd black and Pd/C catalysts, respectively.

Liu et al. fabricated trimetallic Pt-based (PtAuCu) alloy nanowires via solvothermal synthesis to determine the enhanced electrocatalytic activity towards MOR due to the synergic effect of different metals.¹⁷⁶ Introducing Cu metal significantly lowered the utilization of the expensive and poisonous Pt metal. Additionally, the dealloying process that results in the dissolution of Cu atoms from the PtAuCu surface during the MOR process generates additional Pt active sites for MOR, increasing the electrochemical activity. The MA, SA, and ECSA of the Pt₅₀Au₁₀Cu₄₀ alloy catalyst were found to be 0.9281 A mg⁻¹_{Pt}, 0.8786 mA cm⁻², 105.62 m² g⁻¹_{Pt}, which was around 4.34, 2.9, and 1.4 times more than those of commercial Pt/C catalysts, respectively. Moreover, compared to the other catalysts, it showcased higher stability and durability after 10,000 seconds for MOR. Xu et al. fabricated PtPdCo mesoporous nano polyhedrons trimetallic with a hollow cavity by a two-step strategy.¹⁷⁰ The first step involved directly fabricating Pd@PtPdCo core-shell mesoporous nanopolyhedrons (Pd@PtPdCo MNPs) via a straightforward chemical reductive procedure. The second stage involved selectively etching the Pd cores of Pd@PtPdCo MNPs in acidic media to create PtPdCo MHNPs. Compared to Pd@PtPtCo MNPs and standard Pt/C catalysts, the PtPdCo MHNPs exhibit improved electrocatalytic activity and durability for MOR. The increased SA, MA, and ECSA were 1.71 mA cm⁻², 0.91 A mg⁻¹, and 53.2 m² g⁻¹, higher than standard Pt/C. Chen et al. fabricated trimetallic nanocatalysts (NiPtPd-HNCs) by introducing Ni elements into PtPd hollow nanocrystals (HNCs) with high activity and superior CO tolerance for MOR.¹⁷⁷ The designed trimetallic NiPtPd-HNCs exhibited excellent MA and SA of 3.95 A·mg_{Pd+Pt}⁻¹ and 10.68 mA·cm⁻², respectively, 4.2 and 4.5 times greater than standard Pt/C. Notably, trimetallic NiPtPd-HNCs were revealed to have better CO tolerance than their bimetallic



counterparts, as demonstrated by CO-stripping tests and rigorous 3000 s chronoamperometry tests in a CO-saturated medium.

The high efficiency of Pt-based alloy nanoporous structures toward alcohol oxidation reactions has received a lot of interest. Particularly, Pt alloying with Earth metal can reduce the cost of the catalyst. Therefore, Lan et al. presented a one-pot hydrothermal method for producing porous bimetallic PtCu and trimetallic Ni-doped PtCu nanoalloys by using a small amount of Ni dopants to increase the stability and activity of PtNiCu alloys towards MOR.¹⁷⁸ The Ni-doped Pt₆₀Ni₃Cu₃₇ nanoalloys exhibited the best electrochemical properties for MOR in an acidic medium. For methanol oxidation in 0.2 M methanol solution, the MA of the synthesized Pt₆₀Ni₃Cu₃₇ nanoalloys was 5.3 and 3.6 times that of commercial Pt black and Pt₅₅Cu₄₅ bimetallic nanoalloys, respectively. Additionally, the stability of the Pt₆₀Ni₃Cu₃₇ nanoalloys was significantly higher than that of Pt₅₅Cu₄₅ nanoalloys and standard Pt black. Moreover, the residual values of the Pt₆₀Ni₃Cu₃₇ nanoalloys after a 3600 s chronoamperometry test were 11.0 times and 3.7 times that of standard Pt/C and Pt₅₅Cu₄₅ nanoalloys, respectively. Peng et al. used a facile two-step co-reduction approach for the synthesis of trimetallic PtPdCr nanoparticles with minimal platinum loading (5 wt%) supported on Vulcan carbon (PtPdCr/C), which showed improved methanol oxidation activity in an acidic medium.⁹⁴ The improved MA and ECSA of the designed nanocatalyst were 969 mA mg⁻¹_{Pt} and 55 m² g⁻¹_{Pt}, respectively, while that of Pt/C were 581 mA mg⁻¹_{Pt} and 55 m² g⁻¹_{Pt}. The developed catalyst displayed higher durability and catalytic activity for MOR than standard Pt/C. Nie et al. fabricated a trimetallic AuPdPt nanocomposite enriched with tungsten carbide (WC) to boost the performance of MOR compared to commercially available Pt/C¹⁷⁹. The desired trimetallic (AuPdPt@WC/C) was prepared via a two-step reaction that involved intermittent microwave heating (IMH) and direct chemical reduction. The trimetallic nanostructures were evenly spread on WC, which SEM, TEM, and EDX confirmed. Further, the electrocatalytic performance was evaluated by CV and chronopotentiometry in an alkaline medium. The SA of AuPdPt@WC/C was 1350 mA cm⁻², which was around 44.3% more than that of Pt/C (752 mA cm⁻²). The outcomes showed that WC-enhanced trimetallic AuPdPt nanocomposites performed better in MOR and stability than standard Pt/C catalysts. Yin et al. designed PtRuCu nano frames (NSc) using BF₄NO as an etching reaction to precisely etch Cu out of PtRuCu NPs.¹⁸⁰ The generated PtRuCu NFs' catalytic performance was examined in methanol and an acidic electrolyte. The ECSA of Pt/C was 51.91 m²g⁻¹, much higher than that of the designed catalyst,



which was $27.39 \text{ m}^2\text{g}^{-1}$. The ECSA of PtRuCu NFs' was due to the largest size of Pt as compared to Pt/C. The SA and MA of PtRuCu NFs were 2.17 mA cm^{-2} and $990 \text{ mA mg}^{-1} \text{ Pt}$, while that of Pt/C were 0.63 mA cm^{-2} and $320 \text{ mA mg}^{-1} \text{ Pt}$; the increased SA and MA were due to the increase in synergetic effect between the elements. Compared to standard Pt/C and the comparable NFs made using the universal acetic acid etching approach, the results demonstrated that PtRuCu NFs had improved catalytic activity and stability in MOR. The designed trimetallic PtRuCu NFs/C possessed superior durability with only 21% decay for MOR catalytic activity after 800 CV cycles.

Liu et al. fabricated two trimetallic NiPtAu-SR_{Au} HNCs with different surface exposure percentages of Au using a simple synthesis method to improve the electrocatalytic performance and anti-CO poisoning capability for MOR as shown in **Fig. 7**.¹⁸¹ Compared to other HNCs, the trimetallic NiPtAu-SR_{Au} HNCs have high catalytic performance and CO tolerance. NiPtAu- HNCs had a MOR-specific activity (31.52 mA cm^{-2}) that was seven times greater than Pt/C (4.50 mA cm^{-2}), while the MA was $1184 \text{ mA mg}^{-1} \text{ Pt}$, which was 1.58 times higher than Pt/C.

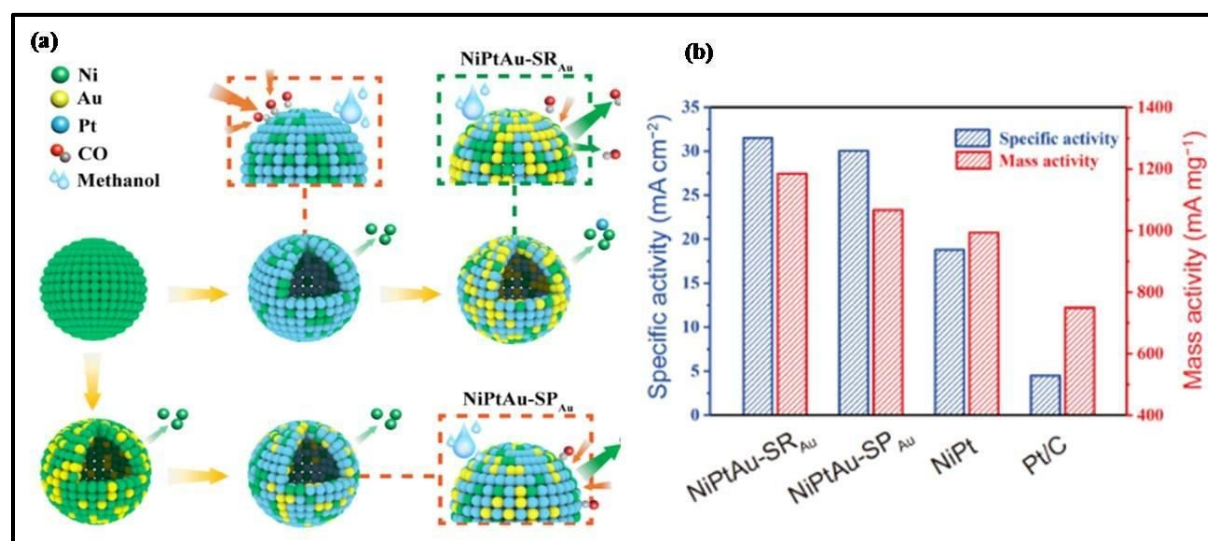


Fig. 7 (a) Synthesis of NiPtAu-SR and NiPtAu-SP HNCs; (b) summary of SA and MA of comparable NPs. This figure has been adapted/reproduced from ref ¹⁸¹ with permission from Springer, copyright 2021.

Wang et al. designed Ag nanocubes (NCs) surrounded by PtRh nanoparticles using a simple one-pot solvothermal reduction approach to function as a trimetallic Ag@PtRhAg NC core-shell



catalyst for MOR, see **Fig. 8**.¹⁸² Notably, the presence of NandN-dimethylacetamide causes the NC core-shell catalyst to function more favorably towards the MOR. The development of the cubic shape was, in turn, regulated by the bromide ions produced by cetyltrimethylammonium bromide. The SA, MA, and ECSA of Ag@PtRhAg NCs were found to be 3.78, 4.22, and 1.17 times more significant when compared to standard Pt/C, respectively, because of the pleated exterior offering more active sites and the synergistic impact between Pt, Rh, and Ag. Due to the higher CO tolerance, Ag@PtRhAg NCs exhibit improved durability by sustaining 84.9% MA even after 1000 MOR cycles compared to the initial value.

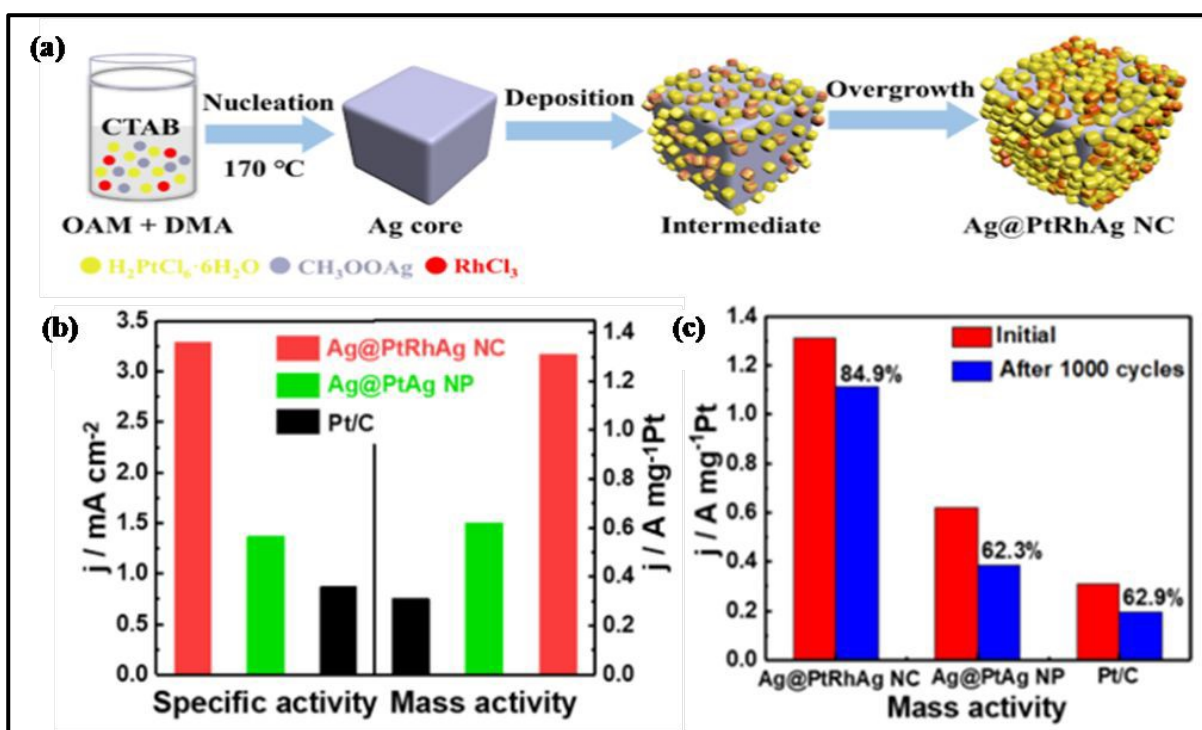


Fig. 8 (a) Schematic illustration of the formation of Ag@PtRhAg NCs; (b) histograms of SA and MA of Ag@PtRhAg NCs, Ag@PtAg NPs, Pt/C; (c) histogram of MA before and after 1000 cycles of Ag@PtRhAg NCs, Ag@PtAg NPs, Pt/C. This figure has been adapted/reproduced from ref¹⁸² with permission from American Chemical Society, copyright 2021.



Shih et al. designed a trimetallic PtNiCo/rGO nanocomposite (NCs) by heating EG solution for 20 min via a simple one-step microwave-assisted technique for enhancing the performance of the catalyst towards MOR as shown in **Fig. 9**.¹⁸³ The Pt-Ni-Co nanoparticles were evenly distributed on the reduced graphene oxide (rGO) without aggregation and displayed a restricted particle size distribution. The electrocatalytic properties of PtNiCo/rGO NCs were better compared to PtNiCo catalyst, including a large ECSA, high catalytic activity of methanol, exceptional anti-toxic qualities, and good electrochemical stability. The average size of the produced PtNiCo/rGO nanoparticles was 17.03 ± 1.93 nm, and at a scan rate of 50 mV/s, the ECSA can be as high as $87.41 \text{ m}^2/\text{g}$. The MA of PtNiCo/rGO NCs was $102.96 \text{ mA mg}^{-1}$ while that of PtNiCo was 44 mA mg^{-1} , whereas the exceptional high ECSA of PtNiCo/rGO NCs was $87.41 \text{ m}^2/\text{g}$ as compared to Pt/C ($58.8 \text{ m}^2/\text{g}$). The homogeneous dispersion of PtNiCo nanoparticles on the rGO surface, superior conductivity, stability, and large specific surface area of the rGO carrier were the reasons behind the exceptional high electrochemical performances.

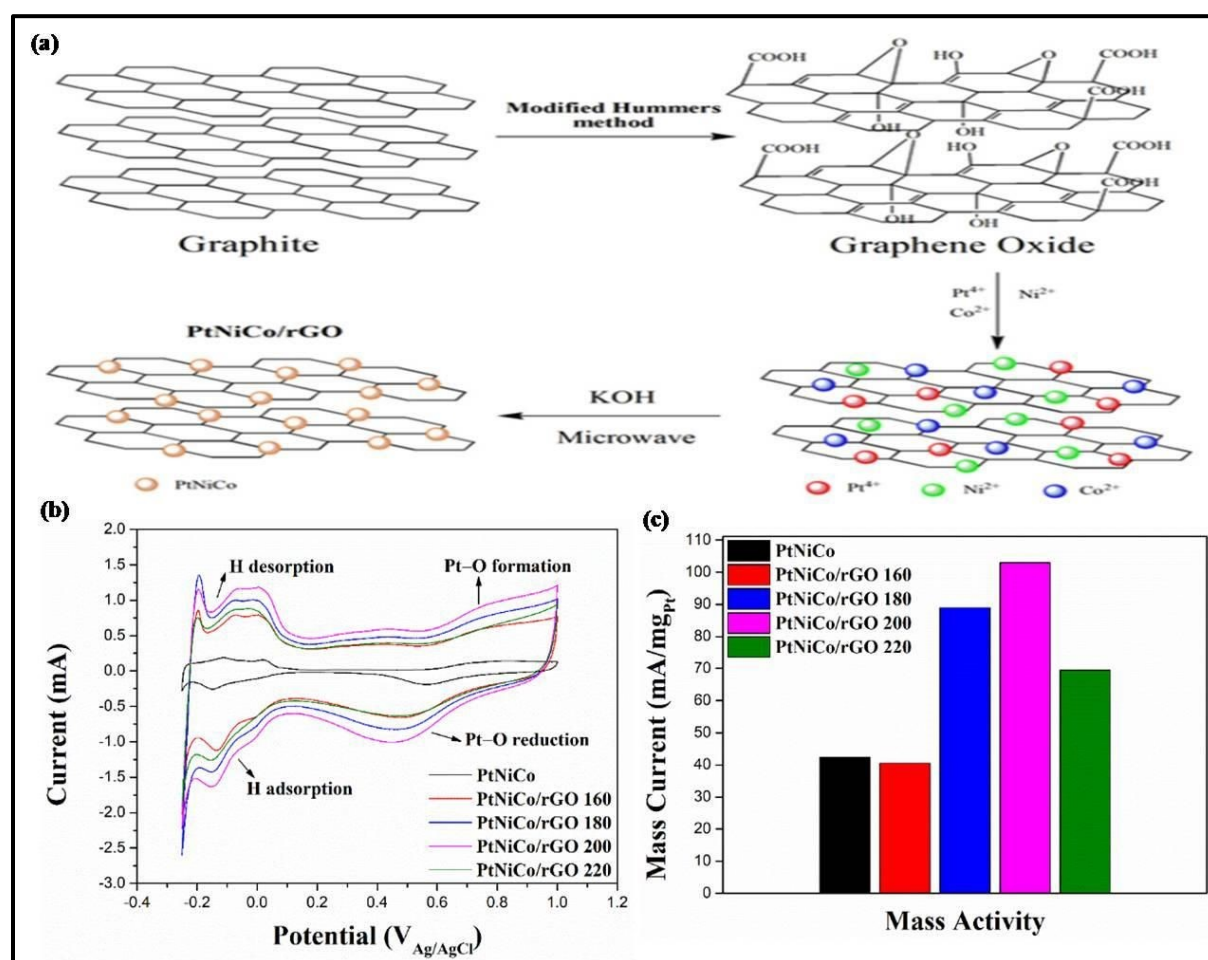


Fig. 9 (a) Illustration of synthesis of the PtNiCo/rGO NPs; **(b)** electrocatalytic performance of PtNiCo, PtNiCo/rGO 160, PtNiCo/rGO 180, PtNiCo/rGO 200, and PtNiCo/rGO 220 catalysts in N₂-purged 0.5 M H₂SO₄ aqueous solution at a scan rate of 50 mV/s; **(c)** histogram of MA of different catalysts for MOR. This figure has been adapted/reproduced from ref¹⁸³ with permission from MDPI, copyright 2021.

Ravichandran et al. fabricated the trimetallic ordered mesoporous nanostructure (OMNs) by using KIT-6 as a surfactant via chemical reduction method and NaBH₄ as a reducing agent to enhance MOR performance.⁹³ Additionally, due to Pt's ordered bifunctional mechanism and mesoporous shape, the oxides of both Ir and Ru significantly improved Pt's electrocatalytic activity by producing more active sites. The OMNs of the Pt_{0.7}Ru_{0.25}Ir_{0.05} electrocatalyst also have an ECSA of 78.35 m² g⁻¹ and MA of 1721 mA mg⁻¹, which were comparably greater than standard catalyst Pt/C (ECSA = 165 m² g⁻¹ and MA = 77.01 m² g⁻¹). The ECSA loss of designed nanocatalysts was only 19.5 % after 5000 durability cycles, significantly less than Pt/C.

The ensemble effect, which arises as a result of variations in local atomic arrangements, can also influence configuration and adsorption strength, ultimately affecting catalytic kinetics.¹⁸⁴ Two series of Ag_x/Au/Pt trimetallic nanoparticles (Ag_xAu₁Pt₂ with *x* ranging from 1–5 and Ag₄Au₁Pt_y with *y* ranging from 1–3) were synthesised via a sequential chemical reduction method involving Pt deposition on preformed Ag/Au core-shell particles. These NPs were then subsequently deposited on MWCNTs for evaluating their electrocatalytic activity towards MOR. It was reported that Ag₄/Au₁Pt_y systems showcased higher electrocatalytic activity compared to typical Pt on the MWCNTs. Particularly, Ag₄Au₁Pt₂ NPs showcased the highest electrocatalytic property towards MOR. In addition, it was observed that the series of Ag_xAu₁Pt₂ catalysts deposited on MWCNTs could promote CO oxidation on Pt owing to existence of Ag and Au, wherein Au was responsible for increasing the adsorption of CO, and Ag could simultaneously weaken the CO bond from Au and Pt, resulting in facile release of CO in the form of CO₂ which is a prime example of the ensemble effect.¹⁸⁵

Ethylene Glycol Oxidation Reaction (EGOR)

The simplest dibasic alcohol, EG, has numerous advantages over other dibasic alcohols, including a high theoretical energy capacity, ease of production, and practical storage and transportation.¹⁸⁶



EG is the ideal liquid fuel for DAFCs in both acidic and alkaline conditions out of all the fuels regularly utilized in modern industry. The EGOR on the anode of DAFCs is a significant half-reaction.¹⁸⁷ However, there aren't many studies on long-chain alcohols like ethanol, EG, and glycerol.¹⁸⁸ According to reports, long-chain alcohol oxidation is more promising than DMFC in energy density, fuel crossover, and electromotive force due to their high electromotive force and energy density.¹⁸⁹ However, it has been noted that the complete oxidation of long-chain alcohols, like EG, is a lengthy and multi-step process when carried out at room temperature.¹⁹⁰ However, the EGOR on conventional Pt-based catalysts resulted in low efficiency and poor current density because it is arduous to break the C-C bond in C2 –alcohols.¹⁹¹ In addition, regardless of the kind of small alcohol molecule used, the strongly adsorbed intermediates (particularly CO_{ads}) poison the active Pt sites and eventually inactivate the electrocatalysts.¹⁹² Developing Pt-based electrocatalysts with broad fuel adaptability, high activity, and outstanding CO anti-poisoning properties continues to be complicated.

Bhunia et al. showed the successful fabrication of PtPdNi trimetallic nanocatalysts supported on rGO for glycerol, EG, and ethanol via single-step solvothermal technique.¹⁹³ Adding Ni to PtPd, bimetallic, improved the electronic structure of the surface, electrochemical surface area, and kinetics. Additionally, the hydrophilic properties of Ni revealed its importance in the creation of anode catalysts for alcohol fuel cells by promoting alcohol electro-oxidation and by the removal of carbon impurities built up on the catalyst surface, which could reduce the catalyst poisoning. The EASA value of the designed electrocatalyst Pt₇₀Pd₂₄Ni₆/rGO (185 m²g⁻¹) was higher than the corresponding bimetallic and standard Pt/C. Additionally, EG has a higher mass activity of all electrocatalysts than the other two alcohols. Moreover, Pt₇₀Pd₂₄Ni₆/rGO nanocatalyst had the MA of 7.75 A mg⁻¹ for EG, which was around 4.96 times greater than that of standard Pt/C and around seven times higher than RGO-PtPd nanoflower (1.72 A mg⁻¹),¹⁹⁴ and PtPd@Pt nanocrystals/rGO (1.16 A mg⁻¹).¹⁹⁵ Lu et al. designed the synthesis of Pt₆₆Ni₂₇Ru₇ dendritic nanostructures (DNSs) for the electro-oxidation of various alcohols in an acidic medium.¹⁹⁶ For the electrooxidation of EG, ethanol, and methanol, The MA and SA on the Pt₆₆Ni₂₇Ru₇ DNSs were 2.37 and 2.28 times, 3.55 and 3.42 times, and 4.57 and 4.34 times, respectively, as compared to the standard Pt black. The C-C bond in C₂-alcohols can be successfully broken by the PtNiRu DNSs, which display a wide range of applications for fuel-flexible fuel cell technology. Duan et al. described the fabrication of porous dendritic PtRuPd nanospheres (PtRuPd NSs) by a simple



hexadecylpyridinium chloride (HDPC)-mediated one-step aqueous method using ascorbic acid (AA) as the reducing agent for EGOR and ORR.¹⁹⁷ The designed trimetallic exhibited enlarged MA (1.368 A mg^{-1}) for EGOR compared to standard Pt/C (1.100 A mg^{-1}). The ECSA of the PtRuPd NSs ($23.168 \text{ m}^2\text{g}^{-1}$) was lower than Pt/C ($48.12 \text{ m}^2\text{g}^{-1}$) because in PtRuPd NSs, the particle size is more significant than Pt/C. The E_{onset} and half-wave potential ($E_{1/2}$) of PtRuPd NSs were 0.930 V and 0.852 V , which were more favorable as compared to that of Pt/C ($E_{\text{onset}} = 0.910 \text{ V}$ and $E_{1/2} = 0.822 \text{ V}$) which was primarily responsible for the enhanced OER activity. The unusual dendritic-like spheres with enriched active reaction sites, coupled with the strain effects and electronic modulation amidst the trimetals, were the factors that were primarily accountable for the enhanced catalytic performances and durability of the constructed PtRuPd NSs for EGOR and ORR.¹⁹⁸ Zhu et al. designed trimetallic PtPbBi hexagonal nanoplates (HNPs) having a hexagonal close-packed structure via solvothermal technique for EG and ethanol oxidation reaction, as shown in **Fig. 10**.¹⁹⁹ In an alkaline ethanol solution, the designed PtPbBi HNPs exhibited good MA ($8870 \text{ mA mg}^{-1}_{\text{Pt}}$) towards the ethanol oxidation reaction, which was 12.7 times, while the MA ($10,225 \text{ mA mg}^{-1}_{\text{Pt}}$) towards EGOR was 1.85 times more than standard Pt/C. Moreover, the designed trimetallic exhibited better durability and catalytic activity than the reported Pt-based catalyst and standard Pt/C. A mass activity of 42.7% was maintained for the EGOR even after a 3600s chronoamperometric test, which was unusual for other Pt-based catalysts.



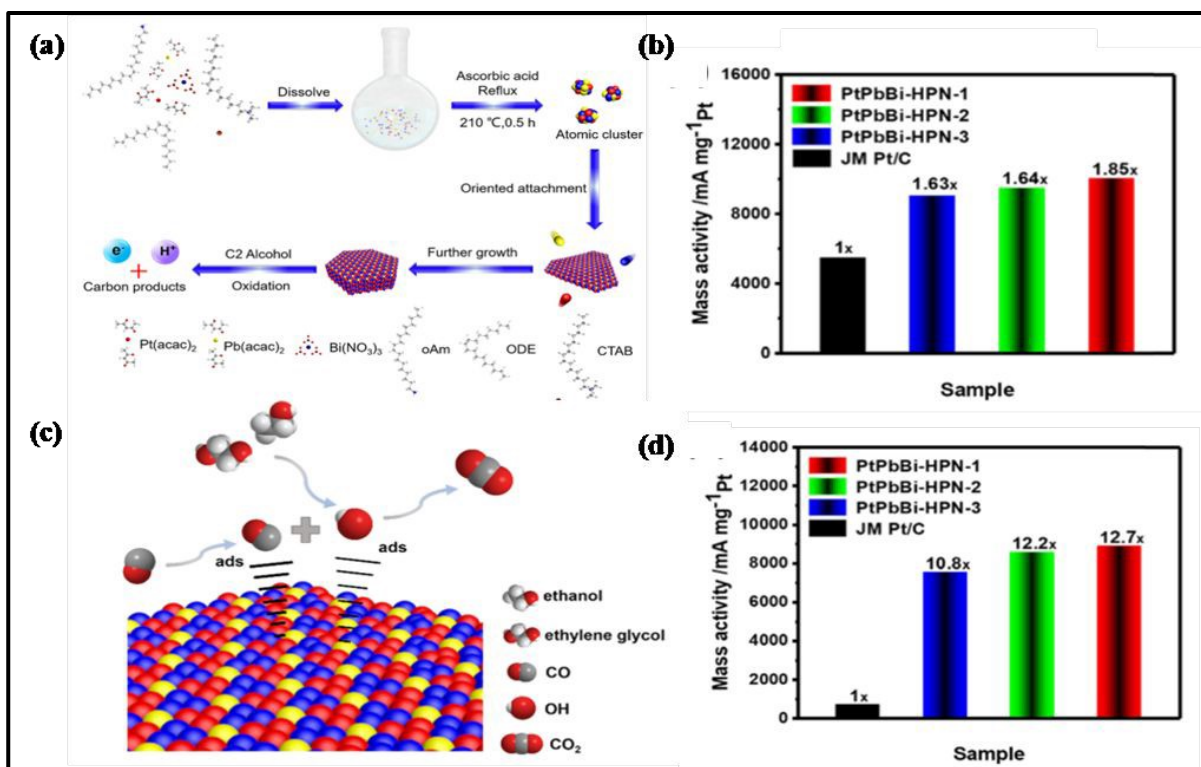


Fig. 10 (a) Schematic diagram for synthesis of PtPbBiHNP electrocatalysts; (b) MA of all catalysts in EGOR; (c) proposed mechanism of PtPbBi HNPs for EOR and EGOR; (d) MA of all catalysts in EOR. This figure has been adapted/reproduced from ref ¹⁹⁹ with permission from American Chemical Society, copyright 2020.

Chen et al. demonstrated the fabrication of PtRhCo petal-assembled alloyed nanoflowers (PtRhCo PAANFs) for EGOR and HER via the solvothermal method.²⁰⁰ The designed nanocatalysts possess significantly improved CO tolerance and recoverability and increased SA and durability for the HER in the alkaline electrolyte by incorporating Rh. The SA of PtRhCo PAANFs nanocatalyst (9.57 mA cm⁻²) was 3.3 times higher than that of Pt/C (2.93 mA cm⁻²) towards EGOR. In addition to this, the MA of PtRhCo PAANFs (2.221 A mg⁻¹) was roughly around 3.5 and 1.8 times higher than those of PtCo NDs (0.627 A mg⁻¹) and Pt/C (1.242 A mg⁻¹).

Ferreira et al. designed the synthesis of trimetallic PtRhNi nanocatalysts supported on carbon for electro-oxidation of ethanol, EG, glycerol, and methanol in acidic media via a reduction method with different atomic rates.²⁰¹ The way in which the nanocatalysts catalyze the electro-oxidation



of glycerol, EG, methanol, and ethanol was categorized using the alcohol oxidation current density and the onset potential obtained after 3600s of chronoamperometry. The ECSA values for the ternary catalysts Pt₆₀Rh₂₀Ni₂₀/C, Pt₄₃Rh₄₃Ni₁₄/C, and Pt₅₄Rh₂₈Ni₁₈/C are respectively 0.923 cm², 0.956 cm², and 0.803 cm², indicating that they have more available active sites for the alcohol oxidation. When compared to Pt/C Alfa Aesar catalyst, Pt₄₃Rh₄₃Ni₁₄/C showed a current density that was 2.2 times higher after 3600 seconds towards EG. Wan et al. designed the synthesis of novel GO/CoMoO₄ nanocatalyst for EG, ethanol, and methanol via hydrothermal technique followed by calcination. Then, Pd-Ni-Ag alloy NPs were deposited on GO/CoMoO₄ nanocatalyst surface by impregnation-reduction approach.²⁰² The peak current density of the designed electrocatalyst (PdNiAg@rGO/CoMoO₄) for electro-oxidation of EG was 7.28 times greater than that of Pd/C while, for methanol and ethanol, it was 5.23 and 4.69 times higher than that of Pd/C, respectively. Moreover, even after 250 cycles, the PdNiAg@rGO/CoMoO₄ catalyst possesses the highest durability and catalytic activity.

Proton Exchange Membrane Fuel Cells (PEMFC)

The PEMFC has garnered much interest in academics and industries for the past ten years. PEMFCs comprise a cathode, anode, and proton exchange membrane. Hydrogen is injected into the anode as fuel, oxygen is oxidized at the cathode, and water is produced as a by-product.²⁰³ PEMFC is one of the classes of fuel cells that has drawn interest in sustainable energy owing to its elevated energy conversion efficiency of 60% and capacity to produce more than 80% of electrical and thermal energy, thus causing zero pollution.²⁰⁴ Furthermore, H₂-PEMFCs can be created for various applications, including portable, stationary, and automotive systems.²⁰⁵ However, just like other emerging technologies, H₂-PEMFCs also have some drawbacks, such as slow oxygen reduction reaction (ORR) kinetics occurring at the cathode of the fuel cell. To speed up the cathodic process, it is necessary to enhance the performance of nanocatalysts.²⁰⁶ Platinum (Pt) and Pt-based nanomaterials as electrocatalysts have been extensively used in fuel cells, including PEMFCs, as the best electrocatalysts.²⁰⁷ Under operational conditions, Pt electrocatalysts may quickly dissolve in the solution due to the acid electrolyte's low pH, which corrosively affects Pt-based materials used as the cathode of PEMFCs.²⁰⁸ So, the primary focus of current research is the synthesis of electrode materials that can improve kinetics and durability while lowering the



price of Pt-based cathode catalysts.²⁰⁹ So, various efforts have been put in by researchers to limit the use of Pt in PEMFCs.

Oxygen Reduction Reaction (ORR)

Wang et al. designed a trimetallic Pd-based branched nanocatalyst to enhance ORR activity in aqueous media.²¹⁰ The PdCuAu nanothorn assemblies (PdCuAu NAs) were formed using the facile one-step method. It exhibited the enhanced ECSA of $38.1 \text{ m}^2 \text{ g}^{-1}$, around 2.4, 1.7, and 1.1 folds better than PdCuAu-H NAs, PdCuAu-L NAs, and standard Pt/C. The highly branched nanostructure of the PdCuAu NAs was primarily responsible for the greater ECSA because of the presence of more vacant active sites. Compared to commercial Pt/C catalysts (0.93, 0.83 V), PdCuAu-H NAs (0.88, 0.82 V), and PdCuAu-L NAs (0.85, 0.80 V), the PdCuAu NAs catalyst exhibited the most positive E_{onset} and half potential ($E_{1/2}$) values (0.96, 0.86 V) which further suggests that the PdCuAu NAs had superior catalytic activity for ORR.

Cruz-Martinez and co-workers reported the synthesis of $\text{Ni}_{60}\text{Pd}_{20}\text{Pt}_{20}/\text{C}$ NPs mixed with Vulcan carbon for enhancing ORR activity in an acidic medium.²¹¹ During the synthesis, oleyamine and oleic acid were used as the surfactant, solvent, and mild reducing agent. The ECSA was calculated in acidic media based on CV, rotating disk electrode (RDE), and CO-stripping and was compared to Pt/C. The NiPdPt/C possessed ECSA of $80.78 \pm 3.5 \text{ m}^2 \text{ g}^{-1}_{\text{Pt}}$, which was around 1.4 times higher than the other ($58.70 \text{ m}^2 \text{ g}^{-1}_{\text{Pt}}$), while the SA and MA of the designed nanocatalyst were around 1.2 and 1.7 times higher than that of Pt/C. The Tafel slope of NiPdPt/C was 68.9 mV dec^{-1} , which was lower than that of Pt/C (81.2 mV dec^{-1}). All these electrochemical activities explained the enhanced ORR activity of NiPdPt/C in an acidic medium. Wang et al. explained the synthesis of PtPdNi trimetallic mesoporous octahedral nanocages (PtPdNi MTONs) via a two-step reaction procedure for enhancing ORR activity, see **Fig. 11**.²¹² In the first step, Pd@PtPdNi MTOs were prepared by the one-step co-reduction method using F127 as a surfactant, followed by the etching of the Pd cores with the help of nitric acid to form the final nanocage PtPdNi MTONs. It showed the enhanced electrochemical properties of ORR were due to its surface morphology. The electrochemical performance of PtPdNi MTONs towards ORR was evaluated based on more positive onset potential and half-wave potential, greater ECSA, MA and SA, and lower Tafel as compared to standard Pt/C and Pd@PtPdNi MTOs. It showed a more positive E_{onset} (1.04 V) and



$E_{1/2}$ (0.942V) as compared to Pt/C ($E_{\text{onset}} = 0.95$ V; $E_{1/2} = 0.873$ V) and Pd@PtPdNi MTOs ($E_{\text{onset}} = 0.97$ V; $E_{1/2} = 0.884$ V). The Tafel slope of the designed nanocage (67.5 mV dec⁻¹) was less than that of Pd@PtPdNi MTOs (80.1 mV dec⁻¹) and was quite similar to the Pt/C catalyst (68.7 mV dec⁻¹). The MA, SA, and ECSA of PtPdNi MTONs were 1.14 mA mg⁻¹_{Pt}, 1.52 mA cm⁻², and 55.7 m²g⁻¹ which were higher than Pt/C and Pd@PtPdNi MTOs, respectively. Hence, the designed catalyst is more durable and stable than the others because it showed negligible degradation after 1000 cycles in LSV.

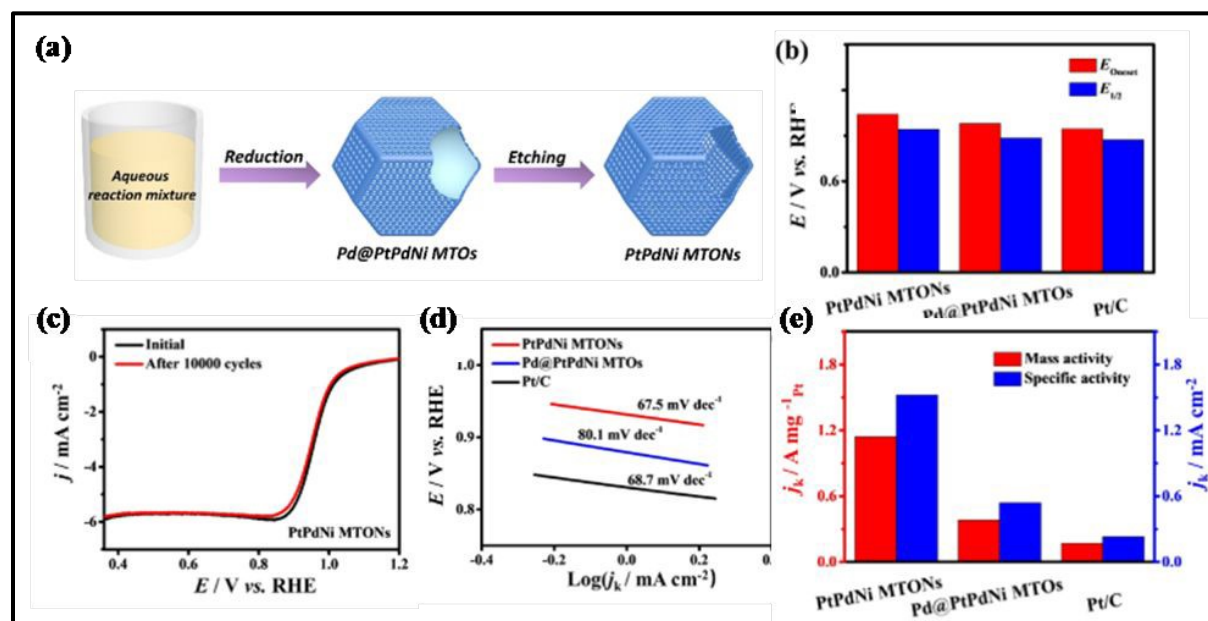


Fig. 11 (a) Schematic illustration for synthesis of PtPdNi MTONs; (b) comparison of E_{onset} and $E_{1/2}$ potential; (c) ORR polarization curves of PtPdNi MTONs before and after the durability tests; (d) Tafel plots of different catalysts; (e) MA and SA of different catalysts at 0.9 V (vs RHE). This figure has been adapted/reproduced from ref²¹² with permission from American Chemical Society, copyright 2019.

Li et al. designed Au@PdPt core-shell NPs based on the Au catalytic reduction method followed by a metallic replacement reaction.²¹³ The designed NPs (Au@Pd_{1.1}9Pt₁) were ultrathin and were stable in an acidic medium towards ORR. It possessed SA and MA around 1.31 and 6.09 times greater than a standard Pt/C catalyst. Moreover, these NPs exhibited higher durability in an acidic medium as there was no change in ORR activity even after 3000 potential cycle range potential between 0.1 and 0.7 V (vs. Ag/AgCl). This was considered one of the best results for designing



simple and cost-effective NPs for ORR. It was observed that by increasing the Pd content, the PdPt shell protects the Pt surface from corrosion and improves the electrochemical stability of Au@PdPtNPs. The one-step synthesis of PtPbPd ultrathin nanowires by octylphenoxypolyethoxyethanol was designed using hydrogen bubbles produced in situ in an aqueous medium by Duan et al.²¹⁴ The as-obtained nanowires (PtPbPd) performed better than commercial Pt/C (20 wt%), PtPb NWs, PtPd NWs, and PdPb NWs in terms of their electrocatalytic characteristics for the EOR and ORR. The designed catalyst had the higher MA, SA, and ECSA of 1.20 A mg^{-1} , 2.78 mA cm^{-2} , and $43.32 \text{ m}^2 \text{ g}^{-1}_{\text{Pt}}$ as compared to that of Pt/C (0.86 A mg^{-1} , 1.79 mA cm^{-2} , and $80 \text{ m}^2 \text{ g}^{-1}_{\text{Pt}}$) in 0.5 M KOH solution. Additionally, the catalyst showed a positive shift in the E_{onset} and $E_{1/2}$ (E_{onset} , 0.993 V, $E_{1/2}$ = 0.891 V) for ORR over Pt/C (0.895 V; $E_{1/2}$ = 0.829 V) in 0.1 M KOH electrolyte. Gao et al. designed a simple, low-cost, stable, and highly active nanocatalyst $\text{Pt}_2\text{Fe}_3\text{Ni}_3/\text{C}$ for enhancing ORR performance in PEMFCs by the two-step reaction.⁶³ The first step involved the addition of Fe and Ni metals on Pt-based NPs via the microwave-assisted polyol method, which further underwent a thermal annealing process at various temperatures. The MA of the $\text{Pt}_2\text{Fe}_3\text{Ni}_3/\text{C}$ catalyst at 675°C was 0.73 A/mgPt, which was around 3.5 times higher than that of the standard Pt/C catalyst, whereas the SA and ECSA of the $\text{Pt}_2\text{Fe}_3\text{Ni}_3/\text{C}$ -675 was $0.77 \text{ mA cm}^{-2}_{\text{Pt}}$ and $110 \text{ m}^2 \text{ g}^{-1}_{\text{Pt}}$ while that of Pt/C was $0.55 \text{ mA cm}^{-2}_{\text{Pt}}$ and $80 \text{ m}^2 \text{ g}^{-1}_{\text{Pt}}$. The designed nanocatalyst was stable and more durable than Pt/C, and it possessed more active sites due to the tendency of alloying Pt metal with others. Hilda M. et al. the synthesis of $\text{Pt}_2\text{NiCo}/\text{C}$ nanocatalyst in an organic medium was designed using two steps to enhance ORR activity in acid media.²¹⁵ In the first step, Pt_2NiCo NPs were formed under a nitrogen atmosphere by reduction method by using $\text{W}(\text{CO})_6$ as a reducing agent. In contrast, in the second step, Pt_2NiCo NPs were uniformly dispersed on Vulcan carbon followed by stirring, which resulted in the formation of $\text{Pt}_2\text{NiCo}/\text{C}$ nanocatalysts. The measured SA and MA of the designed catalyst were around ~ 6.4 and ~ 2.2 times higher than that of Pt/C due to the synergic effect between different metals. It had a lower Tafel slope of $-56.2 \text{ mV dec}^{-1}$, which was quite similar to Pt/C ($-55.5 \text{ mV dec}^{-1}$), whereas it also had a lower overpotential than that of Pt/C. The ECSA of the designed nanocatalyst remained unchanged even after 5000 cycles, as observed by CO stripping. In contrast, there was around a 10% decrease in ECSA properties of Pt/C, which explained its stability in an acidic medium. According to the characteristics mentioned above, it was concluded that $\text{Pt}_2\text{NiCo}/\text{C}$ nanocatalyst can act as a viable candidate as a cathode electrode to use PEMFCs. Tyagi et al.



explained the synthesis of Al-substituted MnFe_2O_4 -based tertiary oxide and RGO known as MAF-RGO nanocomposite via in-situ co-precipitation and hydrothermal process, which was then tested for ORR electrocatalysis in the alkaline electrolyte.⁹² The electrocatalytic performance of MAF-RGO was further supported by the unique ORR peak positioned at 0.56 V vs. reversible hydrogen electrode (RHE) in CV experiments. The electrocatalyst also displayed methanol poisoning resistance of 82% and increased relative current stability of 86%, which was much better than the conventional Pt/C. It possessed the positive E_{onset} of 0.92 V, which was 0.11 V higher than Pt/C. The enhanced performance was only possible by the synergic interaction between the Al-substituted metallic oxide and the RGO sheets.

Metal-air batteries and regenerative fuel cells are viable green alternatives for replacing fossil fuel-based energy systems. Bifunctional electrocatalysts, which can work for OER and ORR, must work efficiently for these energy devices in an acidic medium. Thus, Geethalakshmi and co-workers synthesized carbon-supported trimetallic $\text{Ir}_{30}\text{Pd}_5\text{Pt}_{65}/\text{C}$ and $\text{Ir}_{50}\text{Pd}_5\text{Pt}_{45}/\text{C}$ NPs by in situ and ex-situ techniques to evaluate their OER and ORR activities.²¹⁶ Among the synthesized compositions, the in situ produced $\text{Ir}_{50}\text{Pd}_5\text{Pt}_{45}/\text{C}$ composite had a high limiting current density of 5.151 mA/cm^2 , Tafel slope of 121 mV/dec , and a half-wave potential of 0.931 V vs. RHE at 10 mA/cm^2 for ORR. Similarly, it outperformed OER above other compositions by providing a low Tafel slope of 127 mV/dec and a low overpotential of 80 mV at ten mA/cm^2 . Thus, a possible bifunctional electrocatalyst was an in-situ synthesized $\text{Ir}_{50}\text{Pd}_5\text{Pt}_{45}/\text{C}$ in acidic media.

Water Splitting

Water splitting has appeared as the most suitable sustainable hydrogen conversion technology in the twenty-first century because of its high hydrogen production purity and low environmental contamination.²¹⁷ The oxygen evolution reaction (OER) on the anode and the hydrogen evolution reaction (HER) on the cathode are two of the half-reactions involved in the water-splitting process.²¹⁸ The simplest method of producing hydrogen is to split water ($2\text{H}_2\text{O} + \text{O}_2 + 2\text{H}_2$) in an electrolyzer using the cathodic half-reaction of HER, which requires a two-electron transfer process in an alkaline electrolyte ($2\text{H}_2\text{O} + 2\text{e}^- + \text{H}_2 + 2\text{OH}^-$). From a kinetic perspective, the other half of the anodic reaction of OER involves the slow four proton-coupled electron transfer in the



alkaline electrolyte ($4\text{OH}^- + \text{O}_2 + 2\text{H}_2\text{O} + 4\text{e}^-$), which reduces the efficiency of overall water splitting.²¹⁹

Hydrogen Evolution Reaction (HER)

HER is one of the most widely studied electrochemical processes due to its significance in multiple branches of physical chemistry and its close ties with the heavily debated subject of renewable energy sources.²²⁰ Designing more active cathodes for HER is one of the critical challenges that must be overcome to improve electrolysis' efficiency and economic viability for large-scale production.²²¹ Noble metals are still favored over non-noble metals for the fundamental research of HER electrocatalysis despite their high cost and limited availability. They offer better activity and stability in electrochemical conditions and possess better-defined surface properties.²²² It was reported that Pt is considered the most viable electrode material for HER, followed by Re, Pd, Rh, and Ir.²²³ Therefore, to use Pt as a benchmark for HER electro catalysis, one of the primary research goals is undoubtedly to increase its activity while simultaneously reducing the proportion of Pt in catalysts as it is costly. Pt is alloyed by employing other metals to achieve both targets of forming bi- and trimetallic catalysts.²²⁴ The activity of the bi- and trimetallic catalysts increases because of the symbiotic interaction of the different metals, which further reduces the cost by lowering the use of Pt for HER. Transition metal sulphides²²⁵, selenides²²⁶, borides²²⁷, and nitrides²²⁸ are some promising electro catalysts that have been reported to be helpful in HER. Fu et al. described the colloidal synthesis of monodisperse IrNiFe nanoparticles (NPs) with a diameter of 2.2 nm.²²⁹ Due to the strong synergistic electronic effect of Ir, Ni, and Fe and narrow atomic size, the resulting IrNi_{0.57}Fe_{0.82} NPs displayed good activity and durability for both the OER and HER in acidic electrolyte. The overpotential of the HER and OER was 24, and 284 mV in 0.5 M HClO₄ was required to achieve a current density of 10 mA cm⁻². The Tafel slope possessed by this catalyst towards HER was 34.6 mV dec⁻¹, which was very close to Pt/C (29.6 mV dec⁻¹), whereas the Tafel slope towards OER which was smaller than standard Ir/C (76 mV dec⁻¹). Moreover, IrNi_{0.57}Fe_{0.82} NPs were successfully used as a bifunctional catalyst (HER and OER) for acidic overall water splitting, producing a stable current density of 10 mA cm⁻² at 1.64 V. Smiljanic et al. fabricated trimetallic Rh@Pd/Pt(poly) electrodes in an alkaline medium to boost the performance of bimetallic electrodes towards HER.²³⁰ The electrode was prepared by the co-deposition of Rh metal on the surface of the Pd/Pt(poly) electrode. The trimetallic catalyst was characterized using



CV and CO stripping voltammetry electrochemical techniques, and its activity towards HER was examined using linear sweep voltammetry in 0.1 M NaOH solution. In comparison to the initial Pt(poly) and the associated bimetallic Rh/Pt(poly) and Pd/Pt(poly) electrodes, the Rh@Pd/Pt(poly) catalyst has demonstrated improved catalytic activity for HER. The CO stripping revealed that the ECSA value of the bimetallic electrode was 0.27 cm^2 , which was increased to 0.33 in the case of trimetallic due to the layer formation of Rh on the Pd surface, resulting in an increase in more active sites for HER. Qin et al. fabricated the design of a NiFeMo alloy nanocatalyst to boost the overall performance of electrochemical water splitting via the hydrothermal deposition technique, as shown in **Fig. 12**.²³¹ A whole-cell structured on NiFeMo electrodes on the Ni surface exhibited a low voltage of 1.45 V at a current density of 10 mA/cm^2 , which resulted in low over-potentials for HER (45 mV) and OER (238 mV). The sensor also possessed a lower Tafel slope for OER (35 mV dec^{-1}) compared to IrO_2 (51 mV dec^{-1}), while the E_{onset} was 12 mV. The Ni-Fe-Mo (oxy)hydroxides were self-formed on the outer layer of the NiFeMo anode, which acted as active sites for OER. In contrast, the nanocrystals (Ni, Fe, and Mo) were closely linked at the atomic level, which enables the synergistic effect of metal for efficient HER.



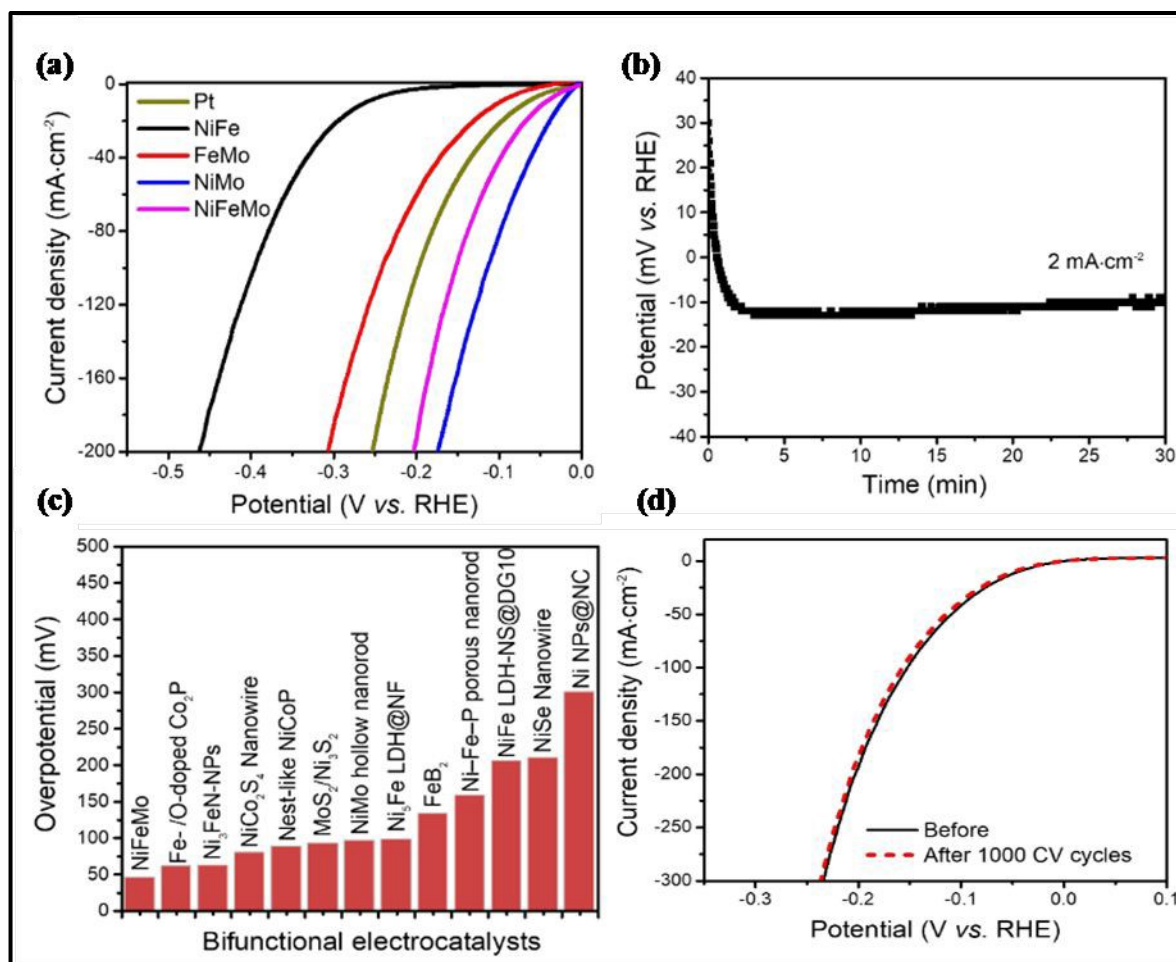


Fig. 12 HER performance of Pt plate, NiFe, FeMo, NiMo, and NiFeMo conducted in 1.0 M KOH. (a) polarization curves; (b) onset HER potential; (c) comparison with selected state-of-art water-splitting electrocatalysts; (d) polarization curves of NiFeMo before and after 1000 cyclic voltammetry cycles. This figure has been adapted/reproduced from ref ²³¹ with permission from American Chemical Society, copyright 2018.

Chen et al. designed AuPtPd nanodendrites (NDs) via the quick and easy wet-chemical synthesis in an alkaline medium at room temperature by employing ascorbic acid in terms of a reducing agent and L-proline as a guiding agent, respectively, for enhancing the performance towards HER and OER. ²³² The as-prepared AuPtPd (NDs) exhibited significantly higher ECSA ($27.65 \text{ m}^2\text{g}^{-1}$), SA (0.21 mA cm^{-2}), and MA (58.94 mA mg^{-1}) for HER and OER concerning standard Pt black (ECSA: $20.88 \text{ m}^2\text{g}^{-1}_{\text{metal}}$, SA: 0.13 mA cm^{-2} , MA: 26.68 mA mg^{-1}) which explained the improved results of the formed NDs towards OER and HER. The NDs also possessed lower over potential



(29 mV) and Tafel slope (36 mV dec^{-1}) for HER concerning Pt/C (46 mV and 43 mV dec^{-1}), which explained the enhanced electrocatalytic efficiency of AuPtPd NDs towards HER. Zhang et al. designed the synthesis of novel trimetallic FeNiMo encapsulated in carbon cages to improve its activity towards HER.²³³ The electrocatalyst was synthesized at room temperature via direct carbonization and hydrothermal reaction methods. Due to more active reaction sites, the designed electrocatalyst exhibits improved catalytic efficiency towards HER in alkaline and acidic mediums. It displays the desired potential of 246 mV at 10 mA cm^{-2} in acidic solution and 199 mV in alkaline solution, which was much lesser as compared to other bimetallic NPs but exceptionally higher than Pt/C, which resulted in better electrocatalytic performance towards HER. The NPs possessed better durability, stability, and recovery than others. Moreover, the immobilization of Mo transition metal on the bimetallic FeNi was also the reason behind the enhanced performance.

Until 2020, no studies have been done on NiV-based phosphides simultaneously doped with anionic (OER) and cationic (HER) elements, producing significant electrocatalytic activity for total water splitting. Fan et al. designed the synthesis of N-P heteroatom doping to produce trimetallic Ni-V-Fe for total water splitting (OER and HER) by hydrothermal method.²³⁴ The "embroidered" structure of nanosized NiVFe LDHs was then converted into a high-performance phospho-nitride electrocatalyst (N-NiVFeP/NFF) by $\text{N}_2\text{-PH}_3$ plasma doping. This technique successfully adds N-P and improves the stability, electrocatalytic activity, and the HER and OER performance of the N-NiVFeP/NFF catalysts under industry-relevant conditions. The electrocatalyst possesses lower overpotential of 79 mV and 229 mV as well as a smaller Tafel slope of 78.6 mV dec^{-1} and 72.6 mV dec^{-1} towards HER and OER as compared to other bimetallic and commercially available RuO_2 . Li et al. presented a straightforward two-step method for producing trimetallic Fe/Co/Cu-based phosphides implanted on nitrogen-doped carbon graphene (FeCoCuP@NC).²³⁵ The FeCoCuP@NC exhibited excellent electrocatalytic HER performance and long-term durability in acidic and alkaline media. The heterojunctions formed between various phosphides and the synergistic interaction between the N-doped carbon-graphene and active phosphides were responsible for better HER performance of FeCoCuP@NC s. The FeCoCuP@NC at 1 and 10 mA cm^{-2} current density exhibits the highest HER activity with lower overpotentials of 80 mV in acidic and 169 mV in an alkaline medium as well as possessed smaller Tafel slope of 47.6 mV dec^{-1} . The NCs had higher ECSA (789.4 cm^2), indicating the presence of higher active sites, and are responsible for excellent electrocatalytic performance compared to mono and



bimetallic phosphorous-doped NCs. Wang et al. designed the synthesis of Mo–Ni–Co trimetallic selenide ($\text{MoSe}_2\text{--NiSe}_2\text{--CoSe}_2/\text{PNCF}$) nanorod on the surface of Ni–Co foam treated with plasma.²³⁶ Furthermore, at 38 and 180 mV overpotentials, the electrocatalyst can deliver a current density of 10 and 100 mA cm^{-2} , respectively, which set a benchmark compared to other reported catalysts. The nanorod possessed a smaller Tafel slope of 38 mV dec^{-1} and a higher MA of 91 mA g^{-1} . The H_2 generation rate (2.6 mmol h^{-1}) was significantly higher than most previously reported electrocatalysts based on transition metals. When reactions were conducted continuously for more than 100 hours at a high current density (j_{100}), the catalyst exhibited improved long-term electrochemical stability with no obvious decay. It should be noted that HER exhibits better electrocatalytic activity when MoSe_2 , NiSe_2 , and CoSe_2 phases are combined rather than when a single-phase material is used.

One of the most promising methods for producing sustainable hydrogen energy is water electrolysis using electrocatalysts based on non-precious transition metals. Zhang et al. constructed high-performance catalysts made of trimetallic sulfide nanosheets ($\text{Ni}_3\text{S}_2\text{--FeS--CoS}$) enriched with bimetallic-nitroxide nanodots (NiCo(N,O)x) on a surface of 3D NiFeCo foam using in situ synthesis methods such as hydrothermal and plasma sulphurization and the dielectric barrier discharge (DBD) approaches, see **Fig. 13**.²³⁷ The final catalyst exhibited a remarkable electrocatalytic activity for total water splitting with overpotentials of 170 mV for OER and 82 mV for HER at a current density of 10 mA cm^{-2} , which set a benchmark in comparison to other existing non-noble metal electrocatalysts. The Tafel slopes for HER (68 mV dec^{-1}) and OER (76 mV dec^{-1}) were slightly higher than the standard Pt/C (36 mV dec^{-1}) and RuO_2 (45 mV dec^{-1}) but were lower than other catalysts. The nanocatalyst showed excellent stable electrochemical properties and structural durability with negligible changes after continuous OER or HER tests over 50 hours.



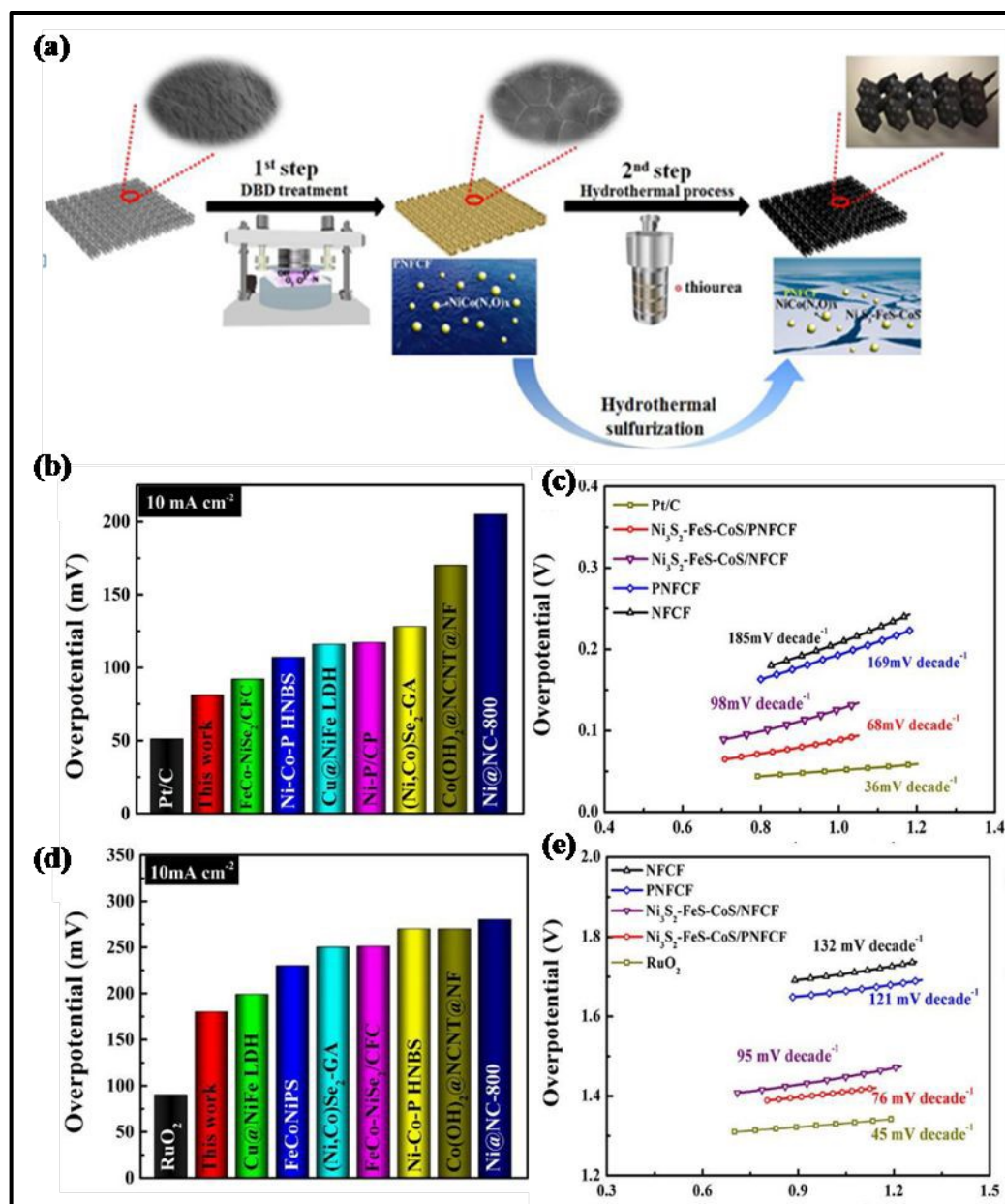


Fig. 13 (a) Schematic representation for *in situ* fabrication of tri-metallic sulfides; (b, d) overpotential comparison delivering j_{10} for different catalysts; (c, e) Tafel slopes for different catalysts at the current density j_{10} . This figure has been adapted/reproduced from ref ²³⁷ with permission from Wiley-VCH, copyright 2020.



Chen et al. designed a hollow alloyed 3D multipods (HAMPs) trimetallic PtNiCo with a rough surface in an alkaline medium via a one-pot solvothermal approach followed by acid etching.²³⁸ Due to their distinct morphologies and synergic effect of trimetal compositions, PtNiCo HAMPs outperformed commercial Pt/C catalysts, PtCo nanocrystals (NCs), and homemade PtNi HAMPs regarding HER performance. The TNP also had a smaller Tafel slope (46.3 mVdec^{-1}) and a lower overpotential (20 mV) at a current density of 10 mAcm^{-2} . The PtNiCo HAMPs showed excellent ECSA ($18.46 \text{ m}^2\text{g}^{-1}_{\text{Pt}}$) and higher MA ($0.44 \text{ mA } \mu\text{g}^{-1}_{\text{Pt}}$), which indicated the availability of more active sites for HER and also possessed improved durability with minimal loss after 10h continuous test of HER. Li et al. designed efficient and durable trimetallic oxyphosphide nanoparticles ($\text{Fe}_1\text{Co}_3\text{Mo}_3 \text{ P-O NPs}$) for overall water splitting in an alkaline medium via a simple hydrothermal approach.²³⁹ At a current density of 10 mA cm^{-2} in an alkaline medium (1.0 M KOH), the ideal $\text{Fe}_1\text{Co}_3\text{Mo}_3 \text{ P-O NPs}$ exhibited extremely low overpotentials for the HER (111 mV) and OER (231 mV) and smaller Tafel slope for both HER (58.2 mVdec^{-1}) and OER (54.5 mVdec^{-1}) respectively. The ECSA of $\text{Fe}_1\text{Co}_3\text{Mo}_3 \text{ P-O NPs}$ (3.39 mF cm^{-2}) towards OER was 1.42 and 1.22 times higher than $\text{Fe}_{0.5}\text{Co}_3\text{Mo}_3\text{P}$ and $\text{Fe}_3\text{Co}_3\text{Mo}_3 \text{ P-O}$ and possessed structural stability for minimum 50 h. Fu et al. fabricated Pt-inlaid Ni-Fe nanocatalysts for HER and OER by uniformly absorbing Pt nanoparticles on the Fe-Ni PBA cube structure and using AA as a reducing agent.²¹⁷ A porous structure was created on the PBA cube using the acid etching process, which increased the catalyst's exposed area and provided more active sites for HER and OER. The porous Ni-Fe-Pt nanocubes (NCs) demonstrated outstanding long-term stability and electro-catalytic activity towards OER and HER because of their porous structure, high ECSA, and uniformly embedded Pt nanoparticles. In this work, the Tafel slopes for HER and OER were 40 and 65 mVdec^{-1} , the η at a current density of 10 mA cm^{-2} were 463 and 339 mV, and the onset potential were 0.444 and 1.548 V, respectively. Thus, the designed nanocubes showed excellent durability and stability. Khalid et al. synthesized FeCoNi alloy nanocatalysts embedded in an N-doped carbon shell via a straightforward one-step chemical reaction using two organic linkers (2, 6-naphthalene dicarboxylic acid dipotassium and 2-methylimidazole) and three metals (Fe, Co, Ni) followed by pyrolysis.²⁴⁰ To produce a current density of 10 mA cm^{-2} in alkaline electrolyte, the synthesized catalyst ($\text{Fe}_{1.0}\text{Co}_{1.1}\text{Ni}_{1.4}\text{-NC}$) required a voltage of 1.52 V and overpotentials of 270 and 168 mV for OER and HER, respectively. The nanocatalyst offered a small Tafel slope for water splitting (168 mVdec^{-1} for HER and 60 mV dec^{-1} for OER). According to X-ray



photoelectron spectroscopy, Fe^{3+} ions were inherently linked to the strong catalytic activity of $\text{Fe}_{1.0}\text{Co}_{1.1}\text{Ni}_{1.4}\text{-NC}$.

Developing non-noble metal-based bifunctional (HER and OER) electrocatalysts in water splitting is still challenging. Ren et al. fabricated FeNiCo@NC/NF via the MOF-on-MOF technique, which included loading nickel foams with nitrogen-doped carbon nanotubes.²⁴¹ FeNiCo@NC/NF electrodes exhibited outstanding HER and OER activity at a current density of 10 mA cm^{-2} with a low overpotential of 145 and 245 mV and a small Tafel slope of 82 mV dec^{-1} for HER and 32 mV dec^{-1} for OER, respectively. It solely requires 1.61 V to obtain 10 mA cm^{-2} when employed for water splitting employing both anode and cathode, and it even outperforms the reference electrode couple of $\text{Pt/C}||\text{RuO}_2$ at greater current densities. The research concluded that trimetallic FeNiCo nanoparticles were responsible for increased synergetic metal active sites. In contrast, conductive Ni foam substrates lowered a material's internal impedance, and N-doped carbon nanotube arrays gave more effective electron transport channels. Yaseen et al. presented a straightforward and cost-effective approach for the in-situ production of Ni-Fe-Co-based nanoparticles enclosed in ultrathin carbon nanosheets (NFC@CNSs).²⁴² The NFC@CNSs were prepared using a simple pyrolysis process. The designed nanoparticles exhibited the low overpotential of 213 and 254 mV for HER and OER in alkaline solution at a current density of 10 mA cm^{-2} as well as produced a small tafel slope of 115.1 and $61.29 \text{ mV dec}^{-1}$ towards HER and OER. Furthermore, the NFC@CNSs-700 catalyst exhibited a hierarchical flower-like structure and had a broad SBET surface area of $145.39 \text{ m}^2 \text{ g}^{-1}$, enhancing the catalytic efficiency. The improved performances, such as robust stability and electronic structure, resulted from strong coupling between carbon nanosheets and TMNPs. Yang et al. described the synthesis of iron-based metal phosphides (IMPs) nanoparticles stabilized on phosphorus-doped vertically aligned graphene (IMPs/P-VG).²⁴³ The $\text{Fe}_{0.5}\text{Co}_{1.5}\text{Ni}_{0.5}\text{P/P-VG}$ nanocatalysts exhibited the best catalytic activities and durability towards HER and OER with a low overpotential of 56 mV and 340 mV and a small Tafel slope of 58.9 mV dec^{-1} and 63.9 mV dec^{-1} which was quite near too commercial nanocatalysts respectively in 1.0 M KOH electrolytic solution at 10 mA cm^{-2} current density. In addition, $\text{Fe}_{0.5}\text{Co}_{1.5}\text{Ni}_{0.5}\text{P/P-VG}$ exhibits good stability up to a 12-hour test without significant loss in various electrolytes. The designed nanocatalysts had exceptional VG structure created by directional freeze casting and helped stabilize the abundant active sites.



Oxygen Evolution Reaction (OER)

The OER is a crucial half-reaction involved in various electrocatalytic processes, including electrolytic water splitting, metal-air batteries, electrochemical reduction of CO₂ and N₂, and so on.²⁴⁴ Noble metal compounds like IrO₂ and RuO₂ have demonstrated outstanding OER performance in alkaline media, offering low overpotential, which set a benchmark compared to other metals. Still, their high cost, extremely low earth abundance, and poor durability at high current density operations restrict them from being used on an industrial scale²⁴⁵. Therefore, in recent years, researchers have worked hard to develop novel materials that are less expensive, stable, and perform better at high current densities towards OER²⁴⁶. In this regard, a wide range of electro-catalysts for the OER has been produced, including transition-metal-based alloys²⁴⁷, metal oxides²⁴⁸, nitrides²⁴⁹, sulfides²⁵⁰, selenides²⁵¹, hydroxides²⁵², tellurides²⁵³, phosphides²⁵⁴, and carbides.²⁵⁵

Yang et al. demonstrated the synthesis of stable Ni₆Fe₂Cr₁ LDH nanocatalyst to enhance the catalyst activity towards OER compared to other standard catalysts.²⁵⁶ Additionally, these nanostructures were produced directly on carbon paper, which offers a large surface area for 3D electrode, and this electrode required the lowest over potential as low as 225 mV to attain a catalytic current density of 25 mA cm⁻² in alkaline electrolyte and had a small Tafel slope of 69 mV dec⁻¹. Trimetallic NiFeCr LDH is among the most potent triggers for OER catalysts to date and is much more active than NiFe LDH because of the synergistic interactions between these metal centers. Wang et al. synthesized trimetallic Ni@Au@Pd core-shell electrocatalyst for ORR and OER.²⁵⁷ The catalyst was made up of bishell (Au@Pd) and Ni core using rGO as a substrate using a chemical reduction-replacement method. According to the research, it was concluded that Ni@Au@Pd-rGO displayed a half-wave potential (0.7713 V), which was similar to Ni@Pd-rGO and much better than industrial platinum (Pt/C). In addition, a higher limiting current (5.6 mA cm⁻²) was obtained for the designed catalyst compared to Ni@Pd-rGO and Pt/C, demonstrating its enhanced activity towards ORR. Among these three materials, Ni@Au@Pd-rGO had the lowest Tafel slope (0.199 V dec⁻¹), the lowest overpotential (0.52 V), and the lowest onset potential (E_{onset}) (1.5663 V) in OERs when observed in alkaline media. So, the results confirmed that the sensor worked effectively for OER and ORR. The stability and synergic effect of these three metals were the main reason behind their enhanced electrochemical activity. The electrocatalyst was also



employed in lithium-air (Li-O₂) batteries as a cathode electrocatalyst. It showed a specific capacity of 500 mAh g⁻¹, and the terminal voltage decreased after 207 cycles. It also exhibited 8077 mAh/gcatalyst capacity at a current density of 100mA g⁻¹. Lu et al. reported the formation of trimetallic N-doped carbon nanotubes via the reflux method for enhancing the OER activity compared to other reported nanocatalysts.²⁵⁸ Due to the addition of the third metal, the synergic interaction between the three metals increases, and thus, it also enhances its performance towards OER. The CoFeNi@CNTs required an overpotential of 287 mV to obtain a current density of 10 mA cm⁻², which was significantly lower than required by IrO₂ (355 mV), CoNi@CNTs (392 mV), and FeNi@CNTs (319 mV), respectively. The Tafel slopes for CoFeNi@CNTs was 32 mV dec⁻¹, which was smaller as compared to CoNi@CNTs (79 mV dec⁻¹), FeNi@CNTs (50 mV dec⁻¹), and IrO₂ (38 mV dec⁻¹) respectively. So, it was clear that CoFeNi@CNTs show a kinetically faster reaction with lower mass and electron transport barriers.

Li et al. fabricated ternary FeCoNi alloy nanoparticles enclosed in bamboo-like N-doped CNTs.²⁵⁹ To improve electrocatalytic performance for OER in alkaline media, FeCoNi alloy, and N-CNTs were combined to produce FeCoNi@N-CNTs, which had a substantial active surface area, highly high graphitic carbon content, and a lot of active metalC/N_x species. The optimized Fe₁Co₁Ni₁@N-CNTs exhibited a small onset potential (E_{onset}) of 1.43 V and an overpotential of 249 mV at a current density of 10 mA cm⁻². More importantly, a potential of just 1.62 V was required for the water electrolysis to achieve a current density of 10 mA cm⁻² when Fe₁Co₁Ni₁@N-CNTs act as the anode and their previously reported Fe₁Co₃Mo₃ P-O act as the cathode electrode which was comparable to the IrO₂ || Pt/C couple. Khodabakhshi et al. synthesized NiFeCu phosphide nanosheet on nanodendrite Ni₃S₂/NiF substrates as cathode via electrodeposition method by partially substituting Cu for Ni and Fe in NiFeP@Ni₃S₂/NiF to evaluate OER activity in an alkaline medium.²⁶⁰ Cu doping in place of Ni or Fe changes electron density and increases the conductivity and ESCA of designed nanocatalysts. The hierarchical electrocatalyst required an overpotential of just 230 mV to reach 10 mA cm⁻², which was one of the best OER results for metal phosphides and also possessed good OER stability at a current density of 20 mA cm⁻². Senthil Raja et al. designed [FeCoNi(OH)₃(BDC)_{1.5}]/NF MOF nanoslabs as working electrodes by the equimolar deposition of Fe, Co, and Ni metals via a one-step solvothermal technique, which allowed to grow on NF substrate and employing 1,4-benzenedicarboxylic acid as the organic linker.²⁶¹ The sensor had extremely low overpotentials of 196 and



284 mV at corresponding current densities of 10 and 1000 mA cm⁻². The sensor had a low Tafel slope of 29.5 mV dec⁻¹ in an alkaline medium. The catalyst showed only a 5% loss in current densities when tested at a high current density of 1000 mA cm⁻² for 50 hours continuously, which means the catalyst is stable.

Recent research has identified transition-metal phosphates and phosphides as potential components for electrochemical conversion, energy conversion storage, and chemical stability. Moreover, producing such materials frequently involves toxic precursors and enormous energy costs, which are considered disadvantages for practical use. In this paper, Kim et al. described the synthesis of transition-metal phosphates at ambient temperature for supercapacitors and the OER.²⁶² The trimetallic iron-doped porous nickel pyrophosphate (NFPy) nanoparticles were synthesized via a simple co-precipitation method. Ni, Fe, and pyrophosphate precursors were initially constantly stirred at ambient temperature. The Tafel slope and over the potential of NFPy towards OER was just 47.4 mV·dec⁻¹ and 0.210 V, which was less than the commercialized Ru₂O. The as-prepared nanocatalyst exhibited long-term stability and durability as it was exposed to air for around 8 months, and no change in electrochemical performance was observed. Zhang et al. designed a chain of hierarchical trimetallic LDHs comprised of monolayer nanosheets fabricated from oxalate MOFs formed on copper foil via in-situ conformal transformation.²⁶³ The octahedron shape of MOFs, which was made up of extremely thin nanosheets, was preserved by LDHs. In an alkaline electrolytic solution, these trimetallic LDHs exhibited excellent activity and stability towards OER. Compared to most previously reported catalysts, FeCo_{0.5}Ni_{0.5}-LDH exhibited the smallest overpotential of 248 mV and a small Tafel slope of 38 mV dec⁻¹. Hou et al. reported the synthesis of trimetallic nanosheets S|NiNx-PC/EG via pyrolysis of ternary dicyandiamide-thiophene-nickel salt, which was grown on electrochemically exfoliated graphene (EG) foil in an Ar atmosphere at 900 °C which further undergoes acid leaching process²¹⁹. The S|NiNx species were well dispersed on porous carbon (PC) and represented the presence of active sites for OER. The developed S|NiNxPC/EG nanosheets performed better towards OER than all previously reported transition metal-carbon catalysts, including the industry-standard Ir/C catalyst (1.59 V at 10 mA cm⁻²) in alkaline media. They represented a low overpotential of 1.51 V at 10 mA cm⁻² and a small Tafel slope of 45 mV dec⁻¹. Liu et al. designed trimetallic nitride nanocatalyst CoVFe/NF, which was grown on nickel foam to enhance its OER performance compared to expensive electrocatalyst RuO₂.²⁶⁴ The overpotential of CoVFeN@NF was relatively lower at 212 and 264



mV at 10 and 100 mA cm⁻² in alkaline media, respectively, as well as they had a small Tafel slope of 34.8 mV dec⁻¹ for OER. According to structural characterization, it was revealed that the superior catalytic activity was primarily caused by the development of oxyhydroxide species on the catalyst's surface as well as by the increased synergic effect of the trimetallic system. Wang et al. described a novel Janus-type nanoarchitecture made from trimetallic sulfide nanowires (Ni-Co-Fe-S/rGO) wrapped in rGO obtained from MOFs and followed by hydrothermal sulfidation for enhancing electrocatalytic OER performance and photocatalytic organic compound degradation (POD).²⁶⁵ It shows good durability and cyclic stability towards OER in aqueous solution as it also gave a small Tafel slope of 56.4 mV dec⁻¹ and a lower overpotential of 251 mV at 10 mA cm⁻². It also exhibited a high rate of photocatalytic degradation (96.06%) for the rhodamine B dye and can maintain this rate in cyclic degradation.

Kahnamouei and Shahrokhian reported the synthesis of NiCoFe nanocatalyst with an open-cage/3D frame-like structure for OER.⁶⁴ It was prepared by the sequential thermal treatment on the cage structure of CoFe Prussian blue (CoFe-PBA) under an argon (CoFeA-TT) atmosphere, followed by the electrochemical deposition of Ni-Co-sulphide (NiCo-S) nanosheets forming a shell layer on it. The electrochemical data indicated that the deposition of NiCo-S on CoFeA-TT (NiCo-S@CoFeA-TT) showed the best catalytic performance as compared to a standard RuO₂ catalyst, as it required only a low overpotential of 268 mV to reach a current density of 10 mA cm⁻² and had a Tafel slope of 62 mV dec⁻¹. It also demonstrated high catalytic stability in an alkaline media over a long period. Its remarkable electrocatalytic performances were due to active sites, cage-like structure, and synergic interaction between hybrid components.

Ramakrishnan et al. used a simple, efficient, and one-step in-situ hydrothermal procedure to design a unique method for synthesizing hierarchical iron cobalt molybdenum sulfide nanoflower enclosed in nitrogen-doped graphene (FeCoMoS@NG) as shown in **Fig. 14**.²⁶⁶ Due to its porous network, hierarchical nanostructures, and more significant specific active sites, the FeCoMoS@NG exhibited excellent catalytic activity as it requires an overpotential of only 238 mV for OER and 137 mV for HER to reach 10 mA cm⁻² and also showed a small Tafel slope of 60 mV dec⁻¹. FeCoMoS@NG cathode-based zinc-air batteries were also developed to check their use for overall water splitting. These rechargeable batteries were prepared using FeCoMoS@NG nanohybrid as the air cathode and commercial Zn foil as the anode. These turned out to be one of



the best batteries for overall water splitting in comparison to other Zn-based expensive metal batteries as they had a high-power density of 118 mW cm^{-2} , had an ultra-high open-circuit voltage of 1.44 V and also possessed long-term cyclic stability for over 70 h . So, FeCoMoS@NG turned out to be the inexpensive and easy method for water splitting.

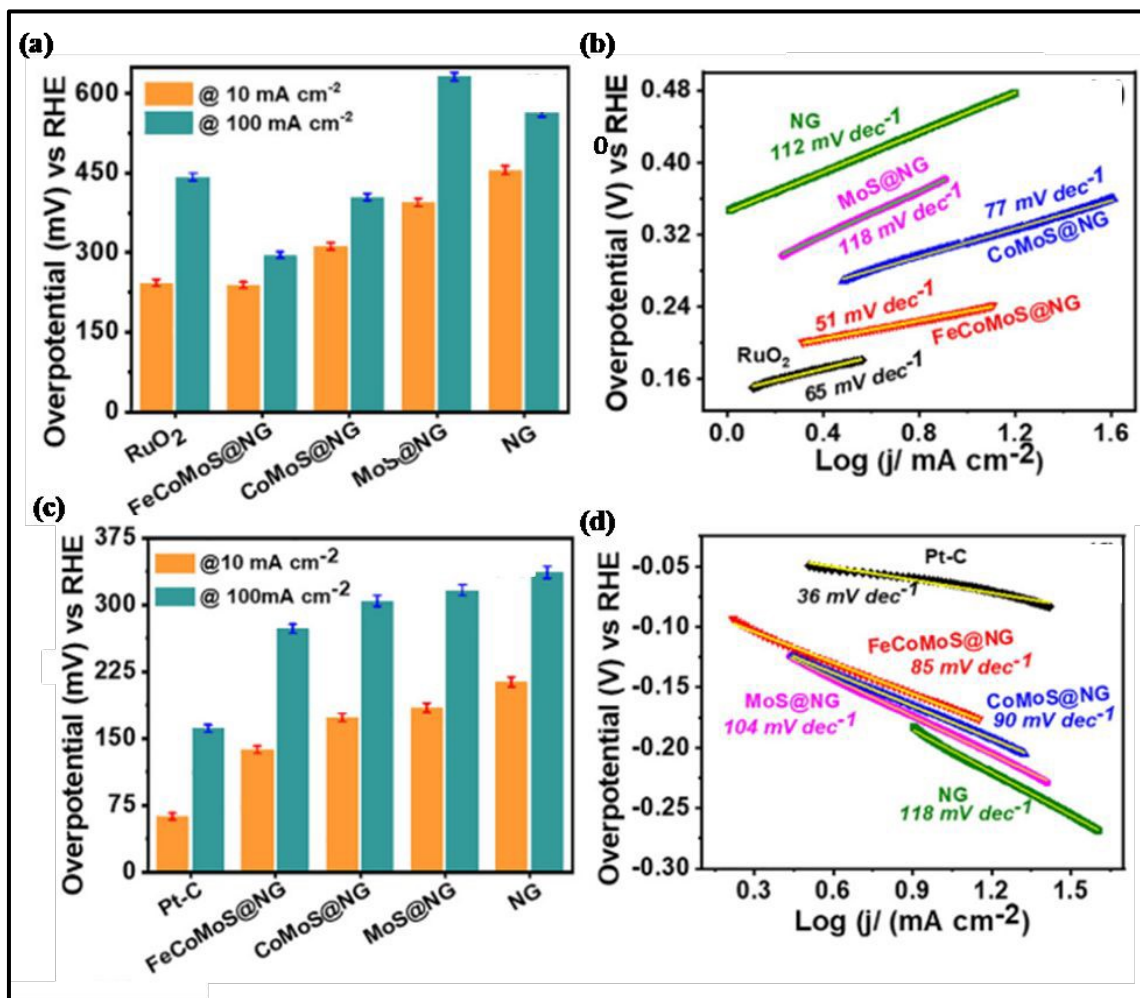


Fig. 14 (a) Bare chart for comparison OER overpotential; (b) Tafel plots of NG, MoS@NG, CoMoS@NG, FeCoMoS@NG and RuO₂ for OER in 1 M KOH; (c) bare chart for comparison HER overpotential; (d) Tafel plots of NG, MoS@NG, CoMoS@NG, FeCoMoS@NG and Pt-C for HER in 1 M KOH. This figure has been adapted/reproduced from ref²⁶⁶ with permission from Elsevier, copyright 2020.



Zhou et al. described the synthesis of a series of trimetallic Mn_xFe_yNi -MOF-74 electrodes in situ by a solvothermal method, which was grown on NF to evaluate bifunctional electrocatalysts for overall water splitting in a primary medium.²⁶⁷ The Mn was added to create a uniform film by controlling the morphology MOF-14, and more active sites were created by the oxidation of Fe^{2+} to Fe^{3+} ions. The optimized $Mn_{0.52}Fe_{0.71}Ni$ -MOF-74 film electrode needed an overpotential of just 99 mV to reach 10 mA cm⁻² current density for Her, whereas an overpotential of 267 mV was required to reach 100 mA cm⁻² OER, respectively. When it was formed as an electrolyzer, the electrode demonstrated good performance towards total water splitting as they required an overpotential of 462 mV and 245 mV to achieve a current density of 100 and 10 mA cm⁻², respectively. This research offers a new perspective on how to create multi-metal MOF-based electrocatalysts. Mao et al. synthesized trimetallic electrocatalyst made up of Fe, Co Ni stabilized on nanosheets made of polypyrrole and rGO (PPy/rGO) by one-step reduction method as they exhibited higher OER due to the synergic effect among metals as compared to other monometallic and bimetallic nanosheets.²⁶⁸ Additionally, FeCoNiBOx/PPy/rGO provides the lowest overpotential of 290 mV, as compared to IrO₂, which had a comparable overpotential of 288 mV and was much lower than the overpotential of FeCoNiBOx (366 mV) and FeCoNiBOx/rGO (311 mV) at current density 10 mA cm⁻², respectively. It also had the lowest Tafel slope of 47.0 mV dec⁻¹, which was comparable to commercial IrO₂ (48.4 mV dec⁻¹) and was much lower than rGO (78 mV dec⁻¹), PPy/rGO (115.1 mV dec⁻¹), FeCoNiBOx/rGO (78.0 mV dec⁻¹), and FeCoNiBOx (103.6 mV dec⁻¹). The synthesis of Ag@NiV_{0.2}Co_{0.2} nanosheets was designed on the surface of nickel foam and uniformly decorated by Ag NPs using the hydrothermal method for OER by Du et al.²⁶⁹ Furthermore, the surface reconstruction caused by the redox reaction and leaching of V metal in an alkaline solution resulted in a highly active oxygen-deficient (oxy)hydroxide layer on top of Ag@NiV_{0.2}Co_{0.2} nanosheets. Furthermore, the ECSA was adjusted by positioning the number of Ag NPs to exhibit more active sites. The Ag@NiV_{0.2}Co_{0.2} gave the Tafel slope of 38.3 mV dec⁻¹ and an overpotential of around 255 mV at 10 mA cm⁻² in an alkaline solution. The designed nanosheets exhibited higher catalytic performance as compared to other transition metal oxyhydroxides because of (i) the active (oxy)hydroxide layer on Ag@NiV_{0.2}Co_{0.2} nanosheets surface, (ii) the considerably enhanced charge ability as a result of the incorporation of Ag NPs; and (iii) the extensively exposed active sites. Keerthana et al. explained the synthesis of Cu₆Mo₅O₁₈ nanoparticles via schematic hydrothermal treatment for OER.²⁷⁰ The nanocatalyst



shape was investigated using surfactants like polyvinylpyrrolidone (PVP) and sodium lauryl sulfate (SDS). The PVP surfactant produced product (SDS- $\text{Cu}_3\text{Mo}_2\text{O}_9$) with better morphology and supports OER activity than the SDS-assisted (PVP- $\text{Cu}_2\text{Mo}_3\text{O}_{18}$) and pure sample ($\text{Cu}_3\text{Mo}_2\text{O}_9$). The PVP-assisted nanocatalysts had a very low overpotential of 124 V and a high current density of 227 mA/g at 10 mV/s. They also demonstrated long-term stability over 16 hours towards OER.

The synthesis of dendritic CoFeCu electrocatalyst was designed, and it was allowed to grow on nickel foam (NF) using the electrodeposition method for OER by Wang et al.²⁷¹ Initially, the synthesized CoFeCu/NF electrode catalyst had a rough surface and cracks, which was modified by adding different amounts of Cu metal, and it also possesses a more active surface site than CoFe/NF. When the optimized CoFeCu/NF obtained a current density (j) of 10 mA cm⁻² in an alkaline solution (1.0 M KOH), it exhibited outstanding electrocatalytic activity with an overpotential of 202 mV for OER. The nanocatalyst also showed a small Tafel slope of 75 mV dec⁻¹ compared to CoFe (80 mV dec⁻¹). It also possesses high ECSA and has a fast charge transfer rate. Chen et al. introduced MoS₂ and LDH on NiCrFe to form an improved NiCrFe-LDH/MoS₂ nanocatalyst using a hydrothermal method to enhance the OER performance.²⁷² Due to the insertion of Cr and MoS₂, the nanocatalyst possesses faster kinetics and improved charge transfer ratio. The potential of NiFeCr-LDH@MoS₂ was only 1.50 V, which was lower than that of a standard Ir/C catalyst (1.59 V) at 10 mA cm⁻², which demonstrated that the designed nanocatalyst had superior catalytic properties. The enhanced OER performance in alkaline solution was determined by low overpotential (270 mV) and lower Tafel slope (85 mV dec⁻¹) compared to other reported catalysts. Huang et al. reported the synthesis of porous Co-based ternary spinel oxide nano boxes (NiCo_{2-x} Fe_xO₄ NBs) by metal-organic framework (MOF) strategy to evaluate its performance towards OER, as shown in **Fig. 15**.²⁷³ This strategy included cation exchange and chemical etching and followed thermal oxidation processes. Due to the synergic effect of the structure, it has excellent electrocatalytic performance and good stability in an alkaline medium. It required an overpotential of only 274 mV to reach a current density of 10 mA cm⁻². In contrast, it also possesses a small Tafel slope of 42 mV dec⁻¹ compared to other Cu-based mono/bimetallic and even smaller than standard RuO₂, which were the characteristic features of nanocatalysts displaying good OER performance in water splitting.



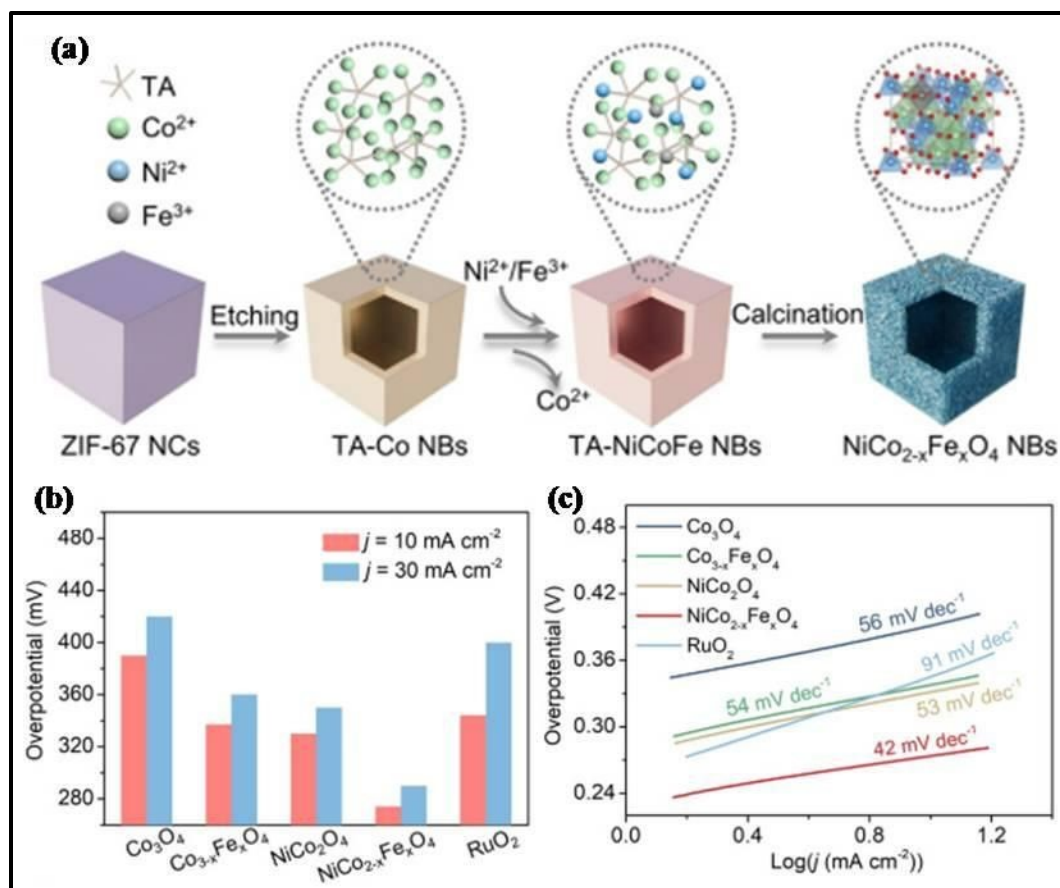


Fig. 15 (a) Schematic overview of trimetallic $\text{NiCo}_{2-x}\text{Fe}_x\text{O}_4$ NBs; (b) overpotentials at j_{10} and j_{30} ; (c) Tafel plots of different catalysts. This figure has been adapted/reproduced from ref²⁷³ with permission from Wiley-VCH, copyright 2021.

Sankar et al. described the fabrication of trimetallic zeolite imidazolate framework (ZIF) derived fibrous material (CoNiFe-ZIF-MFs) using a wet chemical approach, which further undergoes a dependable electro-spinning technique.²⁷⁴ Firstly, it was ensured that metals were successfully implanted into organic frameworks, and then they were used as an electrocatalyst for the OER in an alkaline media. At a current density of 10 mA cm^{-2} , the designed material displayed a lower overpotential of 273 mV and a small Tafel slope of 87 mV dec^{-1} . It also showed stability for 12 hours. So, it was quite evident that the morphology of the designed material was responsible for an increase in electrocatalytic properties towards OER.

Gopi et al. fabricated a trimetallic MOF nanocatalyst based on Ni, Co, and Zn utilizing BTC as a linker for expanding the performance of a single catalyst towards OER, 4-nitrophenol reduction,



and urea oxidation reactions (UOR).²⁷⁵ The team was also involved in the fabrication of its metal oxides, such as carbon composites, at various temperatures, including 600°C (TM-MOF-600), 700°C (TM-MOF-700), and 800°C (TM-MOF-800) by carbonization. The average particle size was measured to be 60-110 nm after calcination, resulting in an inconsistent agglomeration and irregular nanomaterial surface. As per electrochemical tests, it was concluded that TM-MOF-800 exhibited superior performance in both OER and UOR processes, with onset potentials (E_{onset}) of 1.37 V for UOR and 1.66 V for OER at a current density of 10 mA cm⁻². In the presence of an excess of NaBH₄, 4-nitrophenol was catalytically reduced to 4-amino phenol in a significantly less period. These catalysts had excellent stability over the long term when used in an alkaline media. Venkatkarthick et al. thoroughly examined the electrocatalytic activity of the standard NCM hydroxide materials for the two crucial compositions, NCM-523 and NCM-811, in an alkaline medium without adding lithium by a straightforward co-precipitation method for OER.²⁷⁶ For better OER kinetics, the NCM-811 composite had the lowest Tafel slope (91.7 mV dec⁻¹.) and onset potential (E_{onset}) (1.5 V). In contrast, the NCM-523 composite had a relatively higher Tafel slope (175.6 mV dec⁻¹) and onset potential (1.55 V). Moreover, this catalyst exhibited sustained catalytic performance of continuous water electrolysis for 25 hours. When lithium salts were calcinated with the standard hydroxide materials at higher temperatures, the resulting compositions were employed as practical cathodes in lithium-ion batteries (LIBs). However, it was observed that lithium-deficient NCM oxide (NCM-523 or LiNi_{0.5}Co_{0.2}Mn_{0.3}O₂) electrodes had a disordered structure and had superior electrocatalytic activity than its original structure for the OER.



Table 1. TMNPs-based modifiers for fuel cell applications.

S. No	Trimetallic Activity	Synthesis Methods	Electrode/ Electrolyte	Specific Activity (mA mg ⁻¹)		Mass Activity (mA mg ⁻¹)		ESCA (m ² g ⁻¹)		Tafel Slope (mV/dec)	Applications	Ref
1	PtTiMg alloy nanoparticles	Magnetron and co-sputtering method	Toray carbon paper substrates	-	-	-	-	239.5		-	Electrocatalysts in fuel cells	56
2	100-SDS Pt/Ti ₃ C ₂ Tx	Etching Method	Pt NPs	-	-	-	-	9.02		-	Electrocatalyst in fuel cells	151
3	NiPtAu HNCS	Simple Synthetic Method	—	3.29 mA cm ⁻²	0.87 mA cm ⁻²	1.31 A mg ⁻¹ _{Pt}	0.31 A mg ⁻¹ _{Pt}	39.8 m ² g ⁻¹	35.6 m ² g ⁻¹	-	Electrocatalyst in fuel cells	176
4	Ag@PtRh Ag NC	Solvothermal reduction	Ag nanocubes	3.29 mA cm ⁻²	0.87 mA cm ⁻²	1.31 A mg ⁻¹ _{Pt}	0.31 A mg ⁻¹ _{Pt}	39.8 m ² g ⁻¹	35.6 m ² g ⁻¹	-	Electrocatalyst in fuel cells	177
5	PtNiCo/rGO nanocomposites	Microwave-assisted technique	Reduced Graphene	-	-	102.96 mA mg ⁻¹	44 mA mg ⁻¹ for PtNiCo	87.41 m ² g ⁻¹	58.8 m ² g ⁻¹	-	Electrocatalyst in fuel cells	178
6	PtPbBi HNPs	Solvothermal technique	—	251.1 mA cm ⁻²	19.7 mA cm ⁻²	8870 mA mg ⁻¹ _{Pt} for EOR and	696.5 mA mg ⁻¹ _{Pt} for EOR	-	-	-	Electrocatalyst in fuel cells	192

				for EOR	for EOR	10,225 mA mg ⁻¹ _{Pt} for EGOR	and 5510 mA mg ⁻¹ _{Pt} for EGOR					
7	PdNiAg@rGO/CoMoO ₄	Hydrothermal technique followed by calcination	rGO/CoMoO ₄	-	-	-	-	30.44 m ² g ⁻¹	-	-		195
8	Ir ₅₀ Pd ₅ Pt ₄₅ /C and Ir ₃₀ Pd ₅ Pt ₆₅ /C	In situ and ex-situ synthesis	Acidic medium	-	-	-	-	-	-	121 and 118	ORR	209
9	MnFe ₂ O ₄ rGO	Co-precipitation followed by a hydrothermal process	Alkaline medium	-	-	-	-	-	-	-	ORR	88
10	Pt ₂ Fe ₃ Ni ₃ /C	Microwave-assisted polyol method, followed by thermal annealing process	Acidic medium	0.77 mA cm ⁻² _{Pt}	0.55 mA cm ⁻² _{Pt}	0.73 A mg ⁻¹ _{Pt}	0.20 A mg ⁻¹ _{Pt}	110 m ² g ⁻¹ _{Pt}	80 m ² g ⁻¹ _{Pt}	-	ORR	59





11	Pt ₂ NiCo/C nanocatalysts	Chemical synthesis	Acidic medium	1.78±0.11	0.28	0.53±0.05	0.24	29.88±1.74	87.1	-56.2	ORR	208
12	NiPdPt NPs	Synthetic chemical route	Acidic medium	250.8 ± 8.7 mA cm ⁻² _{Pt}	206.4 mA cm ⁻² _{Pt}	202.3 ± 2 mA mg ⁻¹ _{Pt}	121.2 mA mg ⁻¹ _{Pt}	80.78 ± 3.5 m ² g ⁻¹ _{Pt}	58.70 m ² g ⁻¹ _{Pt}	68.9	ORR	204
13	PtPdNi MTONs	Co-reduction followed by etching of Pd cores	Alkaline medium	1.52 mA cm ⁻²	0.23 mA cm ⁻²	1.14 mA mg ⁻¹ _{Pt}	0.17 mA mg ⁻¹ _{Pt}	55.7	52.1	67.5	ORR	205
14	Au@PdPt NPs	Catalytic reduction method followed by metallic replacement reaction	Acidic medium	Acidic medium	3.06 mA cm ⁻²	2.32 mA cm ⁻²	598.53 mA mg ⁻¹ _{Pt}	98.30 mA mg ⁻¹ _{Pt}	-	-	ORR	206
15	Ag@NiV _{0.2} Co _{0.2} nanosheets	Hydrothermal method	Alkaline medium							38.3 mV dec ⁻¹	OER	262
16	Cu ₃ Mo ₂ O ₉ , SDS-Cu ₃ Mo ₂ O ₉ , and PVP-Cu ₂ Mo ₃ O ₁₈	Electrochemical water oxidation approach	Alkaline medium							42 mV dec ⁻¹ for pure 38 mV dec ⁻¹ for SDS	OER	263

										and 34 mV dec ⁻¹ for PVP		
17	CoFeCu/N F	Electrodeposited method	Alkaline medium							75 mV dec ⁻¹	OER	264
18	NiFeCr- LDH@Mo S ₂	Co- precipitation and the hydrothermal method	Alkaline medium							85 mV dec ⁻¹	OER	265
19	NiCo ₂ x FexO ₄ NBs	Chemical etching, cation exchange, and subsequent thermal oxidation processes	Alkaline medium								OER	266
20	CoNiFe- ZIF-MFs	Wet chemical method followed by the electrospinning method	Alkaline medium							42 mV dec ⁻¹	OER	267





21	TM-MOF-800	-	Alkaline medium							197 mV dec ⁻¹ for OER and 137 mV dec ⁻¹ for UOR	OER	268
22	Rh@Pd/Pt(poly) electrode	Co-deposition	-					0.33		-50	HER	223
23	AuPtPd NDs	Wet-chemical synthesis	Alkaline medium					75 mF cm ⁻²		35 mV dec ⁻¹ for OER	HER	225
24	IrNi _{0.57} Fe _{0.82} NPs	Co-reduction followed by decomposition	Acidic medium							34.6 for HER and 48.6 for OER	HER	222
25	FeNiMoC	Hydrothermal method	Acidic and alkaline medium							-75 mV dec ⁻¹ in acidic and 16.9 mV dec ⁻¹ in alkaline	HER	226
26	N-NiVFeP/NFF	Hydrothermal deposition	Alkaline medium							78.6 mV dec ⁻¹ for HER and 72.6 mV dec ⁻¹ for OER	HER	227

27	FeCoCuP@NC's	Direct pyrolysis	Acidic and Alkaline					789.4 cm ²		47.6 mV dec ⁻¹	HER	228
28	Fe ₁ Co ₃ Mo ₃ P-O NPs	Hydrothermal approach	Alkaline medium					3.39 mF cm ⁻² for OER		58.2 mVdec ⁻¹ for HER and 54.5 mVdec ⁻¹ for OER	HER	232



Supercapacitors

Researchers have recently gained much attention on Supercapacitors due to their specific energy, high-specific power, excellent cycling performance, faster charging time, and ecological safety features over conventional batteries.² SCs are employed in hybrid electric vehicles and several power-stabilizing applications because of their excellent operating temperature range and steady cycling behavior. Nonetheless, it bridges the gap between ordinary batteries and capacitors, which have poor power densities and low energy densities, respectively. Numerous research has been carried out to improve the capacitance and energy density of supercapacitors, with an emphasis on electrode materials. Carbon materials (carbon aerogels, activated carbon, carbon nanotubes (CNTs), and graphene) possess a large surface area and store charges through the electronic double-layer capacitance (EDLC) mechanism, which involves the adsorption and desorption of electrolyte ions at the electrode/electrolyte interfaces. The two key performances that determined the factors for SCs devices are the suitable selection of the electrode material and the appropriate selection of the substrate as shown in Table 2.

Ishaq et al. designed an NF-based fluorinated graphene TMNPs (Ni-Co-Fe Nitride) prepared via a one-step nitrogenization process, which acted as an electrode for supercapacitors (SCs).²⁷⁷ An asymmetric supercapacitor (ASC) device was designed using activated carbon-supported NF (AC@NF) as the anode and NCF-N@FG/NF- 3/500 °C hybrid as the cathode. The optimal NCF-N@FG/NF hybrid yielded a rate capability of 87.2 % at 20 A/g, specific capacitance (capacity) of 2110 F/g at 1 A/g, and capacitance retention of 97.6 % after 5000 cycles. The device showed outstanding cycling stability with only 11.5% capacitance loss after 10,000 cycles and a stable potential window of 1.5 V. Moreover, it attained a power density of 374.6 W/kg and an energy density of 56.3 Wh/kg at 0.5 A/g. The device maintained a power density of 7484.2 W/kg and an energy density of 39.5 Wh/ kg at 10 A/g. The designed supercapacitor demonstrated excellent electrode stability and electrochemical activity in real-time applications.

Chen et al. designed a supercapacitor electrode using Prussian blue analog (PBA)@NiCo layered double hydroxide (NiCoLDH) nanocomposite electrode material via a hydrothermal approach.²⁷⁸ Initially, nickel foam (NF) was used to create three-dimensional (3D) controlled NiCo-LDH nanosheets with large interlayer spaces under mild conditions. The target PBA@NiCoLDH/NF



nanocomposite electrode was created in situ from the precursor by a simple thermal ion exchange reaction with potassium ferricyanide. The best electrochemical performance was demonstrated by the PBA@Ni_{0.4}Co_{0.6}-LDH electrode, with an area capacitance of 2004.26 mF cm² at 1 mA cm², which was significantly about three times better than the characteristics of any one component. The SC electrode shows higher cyclic stability. Gonçalves et al. designed NiVCe-layered double hydroxide NPs, which were synthesized by the sol-gel method, and the designed material turned out to be the best electrode material for sensor applications, OER, and hybrid Supercapacitors.¹⁰⁷ The NiVCe-LDH NPs had shown good potential as an electrode material for hybrid energy storage devices, delivering a specific charge of 740 C g⁻¹ at 10 A g⁻¹ and charge retention of 68.7% at 100 A g⁻¹. Furthermore, as demonstrated by their low Tafel slope of 47 mV dec⁻¹. Additionally, NiVCe-LDH nanoparticles have been effectively employed as a prototype for OER. Finally, using a quick and easy batch injection analysis approach, trimetallic NiVCe-LDH-based screen-printed electrodes were designed to detect hydrogen peroxide directly in an accurate mouthwash sample. They were able to achieve a recovery value of approximately 98%.

Zhao et al. prepared a series of Ni-Zn-Co-S hollow nanocages by sequential nickel nitrate etching, co-precipitation, and vulcanization using a bimetallic zeolitic imidazolate framework (Zn-Co-ZIF) with varied Zn/Co ratios as the template.²⁷⁹ The Ni-Zn-Co-S-0.25 electrode successfully served as an electrode material for a three-electrode SC in an aqueous alkaline electrolyte, achieving an extremely high specific capacitance of 1930.9 at 1 A with a reasonable rate performance of 64.5% at 10 A g⁻¹. The Ni-Zn-Co-S-0.25 material was assembled into an asymmetric energy storage device using an activated carbon (AC) anode to demonstrate its advantages further. The Ni-Zn-Co-S-0.25/AC cell has an exceptional capacity for energy storage (32.8 W h kg⁻¹ at 864.8 W kg⁻¹) and an excellent cycle life (keeping 92.2% of the starting capacitance after 10,000 cycles). The Ni-Zn-Co-S-0.25 had excellent electrochemical performance due to the trimetallic sulfide hollow nanocage, i.e., a large active surface area, good electronic conductivity, fast charge transfer, and the synergic effect of different metal ions. Zhang and co-workers worked on designing excellent battery material for hybrid supercapacitors by constructing flower-like structures using an anion exchange approach.²⁸⁰ The amounts of Mn had been adjusted to control the performance of sulfides. It was discovered that Mn doping produces pure phase sulfide while preserving the same floral structure. Mn-doping improved sulfides' specific capacity and cycling stability, and the resultant sulfides maintained a low charge transfer resistance. A specific capacity of 339.5 C g⁻¹



was attained when the specific current was increased 50 times to 50 A g⁻¹ in Mn-doped sulfides, with a maximum specific capacity of 657.7 C g⁻¹ at 1 A g⁻¹. A hybrid supercapacitor with decreased graphene oxide had been formed using the NiCoMn-based sulfide, achieving a maximum specific energy of 36.3 Wh kg⁻¹. It also exhibits long-term cycle stability. Thakur and co-workers prepared Cu-Ni-Co (CNCu) oxide nanowires on carbon cloth (CC) via hydrothermal with a subsequent calcination approach.²⁸¹ The CNCu delivered excellent supercapacitive performance on conducting scaffold, with specific capacitance as high as 2535 Fg⁻¹ at a current density of 1 Ag⁻¹ and outstanding rate capability of 94% at 5 Ag⁻¹ even after 5000 cycles. The CNCu was further considered a reliable and valuable electrode material for constructing a symmetric supercapacitor. The manufactured device exhibited exceptional cyclic stability (capacitance retention of more than 100% after 10000 cycles) and a specific energy of 39 Wh/kg at a particular power of 0.45 KW/kg. The synergistic effect that influenced the rate of redox charge transfer and enhanced the cyclic stability and rate capability was strengthened by the coordination of metal ions. Al Shoaibi and co-workers designed a Co₃O₄@MnO₂@NiO/GO nanocomposite via a hydrothermal approach, a suitable supercapacitor material.²⁸² Further, GO was added to enhance the applications of this nanocomposite for electrode production. The synergistic combination of these composites with GO improves the performance, longevity, and stability of the electrode. The supercapacitor had a specific capacitance of 215-732 F g⁻¹ at current density 1 A g⁻¹ and a potential window of 0-0.8V.

Table 2. TMNPs-based modifiers for supercapacitor applications.

S. No	Trimetallic Activity	Synthesis Methods	Electrode/ Electrolyte	Specification	Ref
1	NF-based fluorinated graphene trimetallic NPs (Ni-Co-Fe Nitride)	Hydrothermal method	carbon-supported NF (AC@NF) as the anode and NCF-N@FG/NF- 3/500 °C hybrid as the cathode.	Specific capacitance - 2110 F/g at 1 A/g	270
2	Prussian blue analog (PBA)@NiCo layered double hydroxide (NiCoLDH) nanocomposite	Hydrothermal approach	PBA@NiCoLDH/NF nanocomposite electrode	Specific capacitance - 2004.26 mF cm ² at one mA cm ²	271



3	NiVCo-layered double hydroxide NPs	Sol-gel method	NiVCo- LDH NPs	Specific capacitance - 740 C g ⁻¹ at 10 A g ⁻¹	103
4	Ni-Zn-Co-S hollow nanocages	Sequential nickel nitrate etching, co-precipitation, and vulcanization	Ni-Zn-Co-S-0.25 electrode	Specific capacitance - 1930.9 at 1 A g ⁻¹	272
5	Ni-Co-Mn sulfide nanoflower-like structure	Anion exchange approach	-	Specific capacitance - 657.7 C g ⁻¹ at 1 A g ⁻¹	273
6	Cu-Ni-Co (CNCo) oxide NWs	Hydrothermal method	CNCo	Specific capacitance - 2535 Fg ⁻¹ at a current density of 1 Ag ⁻¹	274
7	Co ₃ O ₄ @MnO ₂ @NiO/GO nanocomposite	Hydrothermal method	-	Specific capacitance - 215-732 F g ⁻¹ at current density 1 A g ⁻¹	275



Electrochemical sensing application

The growth of complex microfluidics instruments for identifying a wide range of biological molecules appeared as a vital strategy for the real-time monitoring of various diseases. The fabrication of smart devices relying on bio-nanomaterials is considered the result of transdisciplinary work from the materials science to the medical field, as the target analytes recognized by these devices are proteins, enzymes, antibodies, DNA/RNA probes, microorganisms, which can be detected with features low detection limits, great accuracy, and sensitivity. By the biochemical mechanism involved in the detection, the bio-detection system can be developed as a bio-catalytic or bio-affinity-based system. In the first scenario, the bioreceptor (proteins, enzymes, or cells) engages in a catalytic reaction with the analyte. In contrast, equilibrium is reached in the latter case due to a particular binding mechanism between the bioreceptor (aptamer, antibody) and the analyte. Based on the transduction routes, the biosensors can be divided into electrochemical, piezoelectric, optoelectronic, and calorimetric types.

Han et al. designed the trimetallic PtAuPd NPs via an easy technique for the electrochemical detection of glucose in human serum, as shown in **Fig. 16**.²⁸³ The PtAuPd NPs were reduced on the surface of β -lactoglobulin (BLG)-functionalized rGO to form BLG-PtAuPd-RGO nanocomposite. The glucose sensor was designed by immobilizing glucose oxidase (GOx), which was further modified on GCE. The BLG-PtAuPd-RGO sensor showed a linear range of 0.005 to 9 mM, a lower LOD of 0.13 μ M, and a remarkable sensitivity of 63.29 μ A mM⁻¹ cm⁻² (4.43 μ A mM⁻¹). The ECSA of designed NPs was 1.5 and 1.2 times higher than bare GC electrode and BLG-RGO/GCE, respectively. The developed sensor exhibited excellent stability and reproducibility. Thus, the results indicated that it showed excellent results for sensing glucose in real human serum and can be used to diagnose diabetes.



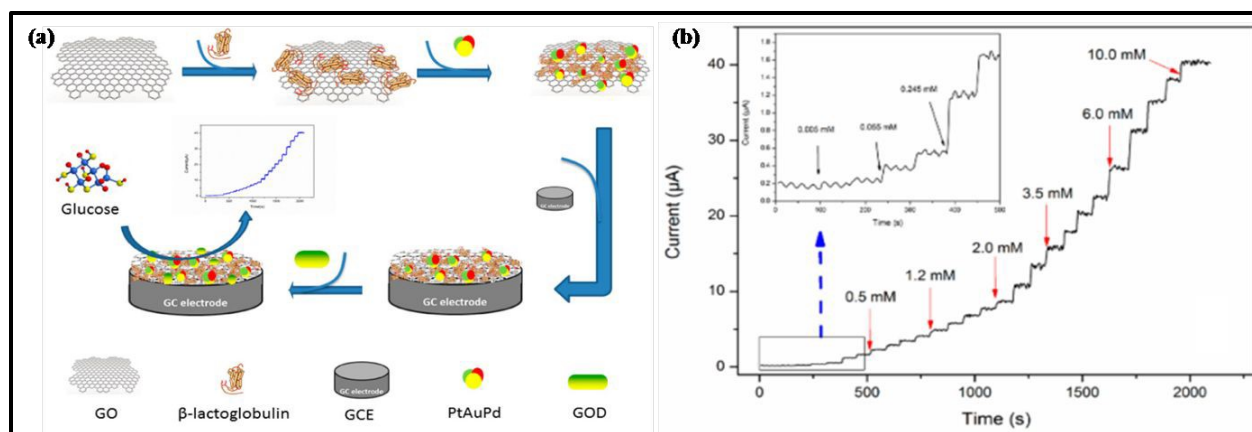


Fig. 16 (a) Synthesis overview of glucose sensor; **(b)** amperometric response of GOD-BLG-PtAuPd-RGO/GC electrode upon successive additions of glucose from 0.005 to 9 mM. This figure has been adapted/reproduced from ref²⁸³ with permission from Elsevier, copyright 2018.

Dong et al. synthesized AuPtPd/rGO trimetallic nanocomposites (NCs) via a one-step method for the electrochemical detection of H_2O_2 released from living breast cancer cells (MDA-MB-231 and T47D).²⁸⁴ The H_2O_2 was released from the cancer cell lines by adding AA, which the designed NCS further detected. The AuPtPd NCs were prepared on modified rGO and GCE by physical adsorption. Superior catalytic efficacy for the reduction of H_2O_2 was demonstrated by the AuPtPd/rGO-modified GCE, which also had a wide linear range of $0.005\mu\text{M}$ to 6.5 mM , a low detection limit of 2 nM . Additionally, after 20 days of storage at room temperature, the as-prepared sensor still had 87% of its initial response current, demonstrating that the suggested sensors had acceptable repeatability and good stability. Shi et al. explained the synthesis of PtAuRu nanoparticles using a simple one-pot method and a glassy carbon electrode (GCE) to detect caffeic acid (CA) via an electrochemical process.²⁸⁵ The synthesized NPs were uniform, and the PtAuRu/GCE showed a photocurrent response towards visible light illumination. The PtAuRu/GCE demonstrated a higher anodic current in 0.1 M phosphate buffer solution, which contains 0.5 mM of CA, as compared to the bare GCE, which suggested that modifying the GCE with synthesized PtAuRu NPs could improve the electrochemical activity towards the detection of CA. This was most likely caused by the high conductivity of metal NPs and the increased surface area because of the synthesized PtAuRu NPs. The linear range and limit of detection (LOD) of the TMNPs were 0.0087 mM to 16.6 mM and $3.9\times 10^{-7}\text{ M}$, respectively. These facts add an essential potential for light illumination to improve the electrochemical detection capabilities of metallic



nanocomposites-based sensors. Barman et al. synthesized Pd@Au@Pt NPs, which were electrodeposited on – COOH terminated functionalized rGO for the electrochemical detection of cancer biomarkers (prostate-specific antigen (PSA) and carcinoembryonic antigen (CEA)) in human serum.²⁸⁶ It was discovered that proper COOH-rGO treatment on Pd@Au@Pt NPs, followed by further EDC/NHS activation, resulted in improved selectivity and stability of the sensing platform. The designed sensor had a sensitivity of $0.099 \pm 0.007 \mu\text{A ng}^{-1} \text{ ml}$, LOD of 8 pg ml^{-1} , and linear range of 12 pg ml^{-1} to 85 ng ml^{-1} for CEA, while for PSA, the sensitivity was $0.267 \pm 0.02 \mu\text{A ng}^{-1} \text{ ml}$, LOD was 2 pg ml^{-1} , and the linear range was three pg ml^{-1} to 60 ng ml^{-1} , respectively. This sensor was used for PSA and CEA biomarkers and other biomarkers. Annalakshmi and coworkers explained the synthesis of NiFeCo nano alloy sensor via a hydrothermal approach for the electrochemical detection of hydrazine in water samples.²⁸⁷ It was discovered that the NFC-fabricated electrode had excellent electro-chemical sensing ability toward HY, which may be due to its low impedance behavior and synergistic interaction with the metallic nanoparticles. The designed sensor demonstrated acceptable analytical performance with a wide linear change of $0.020\text{--}3080 \mu\text{M}$, low LOD (6.4 Nm), and low detection time, i.e., 2 s . The designed sensor demonstrated the results with high accuracy and sensitivity as it was helpful for the detection of HY in various water samples such as lakes, rivers, tap water, and sewage water. Alkahtani and co-workers designed the synthesis of AuPdPt NPs@rGO/GCE nanocomposite for the sensing of Retigabine (REG) oxidation in human plasma and urine samples.²⁸⁸ The AuPdPt NPs were synthesized using the wet chemical method and then uniformly dispersed on rGO. The sensor possessed superior electrocatalytic activity, stability, and sensitivity towards REG oxidation due to the synergic effect of various metals. The AuPdPt NPs@rGO/GCE exhibited a wide linear range of $2.0\text{--}40.0 \times 10^{-7} \text{ M}$, LOD of $0.001 \mu\text{g mL}^{-1}$, and LOQ of $0.003 \mu\text{g mL}^{-1}$. After being stored for 18 days, the modified electrode lost 1.5% of its initial response, demonstrating that the constructed sensor could detect REG over this time. This work was anticipated to provide a new platform for the straightforward one-pot reduction approach of combining non-metals and metals.

Fan et al. designed an electrochemical sensor to detect and sense serum human epididymis protein 4 (HE4), a diagnostic biomarker for ovarian cancer, which was made up of AgPtCo NDs and magnetic nanocomposites ($\text{Fe}_3\text{O}_4\text{@SiO}_2\text{@Au}$ MNCs) by the one-pot method.²⁸⁹ AgPtCo NDs offered a large surface to immobilize secondary antibodies because of their unique dendritic structure. The LOD and linear range of the sample were 0.487 ng ml^{-1} and $0.001\text{--}50 \text{ ng mL}^{-1}$,



respectively. It is interesting that this immunosensor was able to examine HE4 in real samples and displayed strong agreement with clinical studies. Therefore, the suggested electrochemical immunosensor could serve as a viable POCT platform for tumor patients, which is essential for the early diagnosis, treatment, and prognosis monitoring of cancer patients. Ye et al. designed the Cu/Au/Pt NPs for the colorimetric detection of glucose and cancer via the NaBH_4 co-reduction method.²⁹⁰ A colorimetric assay technique was initially proposed to detect glucose based on the catalysis of Cu/Au/Pt TMNPs during the reaction of hydrogen peroxide (H_2O_2) and 3,3',5,5'-tetramethylbenzidine (TMB). A novel theranostic probe was also created by coating Cu/Au/Pt TMNPs with thiolated aptamers. This probe exhibited good photothermal killing performance for the target cancer cells and could successfully realize selective, visual, and sensitive analysis. The LOD for glucose and Cancer cells were 25 μM and 200 cells, while the linear range for the same was 0 to 200 μM and 0–10000 cells, respectively. It was believed that these NPs could be used for various bio-sensing applications and theranostics. Sharifuzzaman et al. synthesized $\text{COOH-AgPtPd/NH}_2\text{-rGO}$ NPs for electrochemical detection of H_2O_2 and prostate-specific antigen (PSA) by a green method.²⁹¹ Firstly, with the help of the layer method, the amino-functionalized rGO ($\text{NH}_2\text{-rGO}$) and carboxylic surface-modified AgPtPd (COOH-AgPtPd) NPs were synthesized, which were used as sensors for various probes. The enhanced synergic effect between $\text{NH}_2\text{-rGO}$ and COOH-AgPtPd raises the electron transport rate and electrocatalytic activity. The LOD and linear range of the sensor towards H_2O_2 were 0.0002 μM and 0.001 to 500 μM , while towards PSA were 0.000004 ng mL^{-1} and 0.000004 ng mL^{-1} to 300 ng mL^{-1} . This sensor was claimed to be used for other applications, too. Salman and co-workers synthesized PdCoAg/C nanostructures using the polyol method, which acted as an electrocatalyst that helped electrochemical sensing of glucose concentration in fruit juices and carbonated drinks.²⁹² The sensor was distinguished by a range of methods, such as X-ray diffraction, SEM, and TEM, and the results concluded that the insertion of the third metal changed the electronic state of the PdCoAg/C nanocatalyst. Due to the synergistic interaction of the ternary metals, the obtained enzyme-free sensor showed outstanding catalytic activity towards glucose with a low LOD (0.003 mmol L^{-1}), broad detection range (0.005 to 0.35 mmol L^{-1}), high sensitivity (4156.34 $\mu\text{A}\cdot\text{mmol}^{-1}\cdot\text{L}\cdot\text{cm}^{-2}$), as well as long-term durability (10 days).

Sharifuzzaman et al. designed a new, facile, green approach for synthesizing $\text{grGO/MoS}_2\text{-NRs/AuPdAg NCs}$ for the electrochemical detection of ochratoxin A.²⁹³ Firstly, a unique method



was discovered for the synthesis of GO, which was prepared by oxidation with NaIO₄ and used as a substrate for the growth of MoS₂. The resultant grGO/MoS₂-NRs nanocomposite demonstrates outstanding electrocatalytic activity because of the excellent electrical coupling activity of grGO and the exposed active edge sites of MoS₂-NRs. The sensor exhibited a lower detection limit of 0.000005 ng mL⁻¹ and a linear range of 0.00001–150 ng mL⁻¹, which was much better than other reported sensors. Qiu et al. designed new trimetallic nanotubes (PtAuAg NTs) to sense methanol in alcoholic beverages.¹⁰² The PtAuAg NTs were synthesized via a simple galvanic replacement reaction using Ag NRs as the self-sacrificed template, obtained using the hydrothermal method. The PtAuAg NTs demonstrated an exceptionally high catalytic efficiency towards MOR, with a LOD of 0.02 mM, high sensitivity of 24.3 mA mM⁻¹ cm⁻², linear range of 0.05–1.8 mM, and a low working potential of -0.2 V. The electron transfer from Au to Pt may have caused the Au component enhancement effect, which encouraged the creation of active oxygen species on Pt. Additionally, the methanol sensor showed outstanding selectivity, repeatability, and storage stability. The stability of this sensor was examined by continuously testing it for 21 days, and the response current was evaluated after three days. The electrode kept 92.3% of its initial response over this time frame. The technique provided a well-organized route for chemical sensors to effectively identify harmful substances on a large scale. Nie et al. synthesized PdCuAu NPs via a one-step synthesis method for the colorimetric detection of H₂O₂ and glucose.²⁹⁴ The produced PdCuAu NPs exhibited good catalytic activity for peroxidase-like enzymes. In the presence of H₂O₂, TMB can rapidly accelerate and be oxidized into a visible blue product (oxTMB). This study used the colorimetric PdCuAu NPs platform to detect glucose and hydrogen peroxide depending on its distinct peroxidase-like characteristics. The LOD for glucose and H₂O₂ was 25 and 5 nM, respectively, and the linear range was 0.5–500 μM and 0.1–300 μM. This rapid and facile technique offers a promising future for detecting glucose and H₂O₂ in real-world applications. Abdelwahab et al. designed a susceptible and novel electrochemical sensor that was capable of determining acetaminophen (AP), dopamine (DA), ascorbic acid (AA), and tryptophan (TP) simultaneously in human blood serum.²⁹⁵ The sensor comprised evenly capped trimetallic (Au, Ag, and Pd) NPs in electroplated graphene oxide (EPGrO). The nanocomposite electrode demonstrated excellent repeatability and greater stability, reflecting the present sensor's efficacy for identifying AA, DA, AP, and TP. The linear range and LOD exhibited by the sensor were 5–650 μM and 0.24 ± 0.03 for AA, 1–700 μM and 0.02 ± 0.01 for DA, 5–700 μM and 0.12 ± 0.04 for AP, 1–600 μM and 0.03



$\pm 0.01 \mu\text{M}$, respectively. Finally, the (Au/Ag/Pd)NPs/EPGrO nanocomposite electrodes were effectively used for determining the concentration of AP, DA, AA, and TP in a real sample of human blood serum. Wu et al. described the fabrication of new Cu/Au/Pt TNs-encapsulated DNA hydrogel by NaBH_4 co-reduction method for colorimetric microcystin-LR (MC-LR) detection in fresh fish tissue and water samples.²⁸⁹ The MC-LR aptamer was hybridized with two main DNA strands on linear polyacrylamide chains to create the DNA hydrogel network. The hydrogel dissolves and releases the preloaded Cu/Au/Pt TNs, which may catalyze the interaction between H_2O_2 and TMB to create color changes if MC-LR is present. This Cu/Au/Pt TNs-encapsulated DNA hydrogel-based colorimetric biosensor may achieve quantitative detection of MC-LR due to this sensitive methodology. The results showed that this colorimetric biosensor, with a linear range of $4.0 \times 10^4 \text{ ng L}^{-1}$ and a detection limit of 3.0 ng L^{-1} , could sensitively detect MC-LR. Using this target-responsive and signal-amplification technique, colorimetric biosensors may be developed for different targets, demonstrating the sensor's significant potential for MC-LR detection.

Elayappan et al. worked on the synthesis of ultrasonication-dry synthesis of gold (Au) NPs-supported copper ferrite (CF) on rGO(Au-CF@rGO). A modified Au-CF@rGO/GCE electrode was also created to conduct the electrochemical analysis to detect dopamine in banana milk samples. The glassy carbon electrode of Au-CF@rGO/GCE (modified electrode) demonstrates remarkable sensing properties, including a wide linear range of $0.001\text{--}119.6 \mu\text{M}$, an LOD of 0.34 nM , and enhanced sensitivity of $\mu\text{A} \mu\text{Mcm}^{-2}$. On the other hand, the modified Au-CF@rGO/GCE electrode exhibited high selectivity, reproducibility, repeatability, and outstanding storage stability. Ma and coworkers explained the synthesis of sandwich-type Au@PdPt Nanocubes for detecting Neuron-Specific Enolase (NSE).²⁹⁰ To enhance the immobilization of the primary antibody (Ab1), the Au@MOFs were used as the substrate. In addition, the insertion of Au NPs enhanced the MOF conductivity and sped up electron transmission at the interface. Secondary antibodies were labeled with sub-30 nm trimetallic Au@PdPt NCs placed onto ultrathin MnO_2 nanosheets ($\text{MnO}_2 \text{ UNs/Au@PdPt NCs}$). Hydroquinone (HQ) oxidation by catalytic H_2O_2 reduction was boosted by the $\text{MnO}_2 \text{ UNs/Au@PdPt NCs}$, which acted as amplification labels to magnify the reductive current signal effectively. The immune sensor demonstrated a low LOD (4.17 fg mL^{-1}), broad detection range (10 fg mL^{-1} to 100 ng mL^{-1}), and good repeatability and stability. These findings suggested that the immune sensor has a promising future in the early



clinical diagnosis of NSE. Chen et al. designed an electrochemiluminescence (ECL) immunosensor made up of Au@Pd@Pt NP for sensing ractopamine (RAC) in the peroxydisulfate/oxygen system.²⁹¹ The TNMP core shell was used as a catalyst, and further, to increase the performance, a layer of norfloxacin-L-cysteine (NC) was coated on Au@Pd@Pt NPs. As a result, the suggested immunosensor had a low LOD ($0.00003 \text{ ng mL}^{-1}$) and a broad linear range (0.0001 to 1000 ng mL^{-1}). Subhan et al. synthesized a trimetallic oxide $\text{MoO}_2\text{-Fe}_3\text{O}_4\text{-CuO}$ nanocomposite by the co-precipitation method for sensing para-nitrophenol (p-NP).²⁹² After synthesis, the nanocomposite was coated onto a GCE for the electrochemical detection of (p-NP) by enhancing the conductivity of $\text{MoO}_2\text{-Fe}_3\text{O}_4\text{-CuO}$. The p-NP content was checked in real samples, such as drinking water from a plastic bottle and industrial effluent water. The sensor possessed excellent sensitivity ($5.2430 \text{ mA mM}^{-1} \text{ cm}^{-2}$), wide linear range (1.0 pM to 0.01 mM), and low LOD (0.2 pM) in significantly less reaction time. The sensor displayed excellent stability and consistency.

Han et al. designed a TMNPs AuPdPt functionalized MWCNTs-AuPdPt for the detection of *Staphylococcus aureus* (*S. aureus*) in food samples to prevent foodborne diseases in humans by ensuring food safety.²⁹³ By depositing AuPdPt TNP on the surface of MWCNTs, the MWCNTs-AuPdPt nanocomposite was created using an in-situ growth technique. The synthesized MWCNTs-AuPdPt had excellent conductivity and exceptional catalytic activity for hydrogen peroxide. Anti-*S. aureus* antibodies were used to functionalize further the MWCNTs-AuPdPt nanocomposite, which already had good biocompatibility and a high specific surface area. The immobilized antibodies effectively attracted *S. aureus* to the modified electrode through an immunological response, which led to a shift in the strength of the catalytic current to enable the sensitive detection of *S. aureus*. The sensor possessed low LOD (39 CFU mL^{-1}) and a wide linear range (1.1×10^2 to $1.1 \times 10^7 \text{ CFU mL}^{-1}$). The proposed immunosensor was also effectively used to identify *S. aureus* in real samples with satisfactory outcomes. So, this sensor effectively determines *S. aureus* and other pathogens in real samples. Cen and co-workers synthesized AuPtPd fluffy-like nanodendrites (FNDs) by a one-pot thymine-mediated method for the highly selective and sensitive electrochemical detection of cardiac troponin I (cTnI).²⁹⁴ The immunosensor was constructed by employing $\text{K}_3[\text{Fe}(\text{CN})_6]$ as a signal probe, which was then tested on dilute serum samples. Such nanostructures demonstrated a high specific surface area to boost the loading of the cTnI Ab, and the electrochemical signals of the probe were enhanced because of the structural



advantages, electronic effects, and synergetic catalysis of the trimetals. The sensor demonstrated a broad linear range ($0.01 \sim 100.0 \text{ ng mL}^{-1}$) and low LOD (3 pg mL^{-1}). Additionally, this biosensor offers a reliable platform for investigating other cardiac indicators in real-world samples. Akhter and team reported a biosensor for the detection of the anticancer agent nilutamide (NLM) that was based on a tri-metallic organic framework (MOF).²⁹⁵ The tri-metallic Co-Ni-Cu-MOF was grown on an NF substrate along with the single metal Ni-MOF, Co-MOF, and Cu-MOF by a solvothermal method. The Co-Ni-Cu-MOF/NF sensor showed vigorous electrocatalytic activity. It displayed a broad concentration range from $0.5\text{--}70 \text{ }\mu\text{M}$ and $70\text{--}900 \text{ }\mu\text{M}$, a low LOD of $0.48 \pm 0.02 \text{ nM}$, and a high sensitivity of $10.712 \text{ }\mu\text{A }\mu\text{M}^{-1} \text{ cm}^{-2}$. These results demonstrated the excellent selectivity and sensitivity of the tri-metallic MOF for the detection of NLM in serum samples. Zhang et al. worked on synthesizing trimetallic Ni/Ag/Zn nano-sensors by green microwave-assisted co-precipitation reduction method for detecting dopamine (DA).²⁹⁶ By analysis of the microstructure, morphological variations resulting from various metal composition ratios were discovered. The elemental and phase composition of the synthesized samples were determined using XRD, XPS, and FT-IR. The modified GCE had good sensing capability for DA, the sensor sensitivity was $0.96 \text{ }\mu\text{A}/\mu\text{M}\cdot\text{cm}^2$, the LOD was $0.3\mu\text{M}$, and the linear range was $1\mu\text{M}\text{--}25 \text{ }\mu\text{M}$. This sensor possessed good anti-interference and selectivity for ascorbic acid (AA), uric acid (UA), and other ion-simulated biological settings. Zhang and co-workers designed the one-pot novel synthesis of $\text{Au}_{1.5}\text{Pt}_1\text{Co}_1$ NPs at room temperature, the co-reduction of Co^{2+} , PtCl_6^- , and AuCl_4^- with hydrazine hydrate for the sensing of hydroquinone in real water samples.²⁹⁷ The morphology, element mapping, and surface roughness of the coated poly-L-cysteine (P-L-Cys) layer on the $\text{Au}_{1.5}\text{Pt}_1\text{Co}_1/\text{GCE}$ surface were examined to confirm continuous electrode modification processes. The sensor possessed two linear ranges for HQ, which were 0.1 to 30 and $30\text{--}200 \text{ }\mu\text{M}$, with a low LOD of $0.045 \text{ }\mu\text{M}$, while the sensitivity of the sensor was $4.247 \text{ }\mu\text{A }\mu\text{M}^{-1} \text{ cm}^{-2}$, which confirmed the excellent catalytic behaviour of the sensor. The designed sensor also possessed excellent selectivity, stability, reproducibility, and repeatability. The sensor might develop into a valuable instrument for detecting electro-active substances in tiny amounts in food or environmental samples. The core/shell structured bimetallic NPs are often reported to have high catalytic activity for partial hydrogenation of diene to olefin owing to the ligand effect between the core and shell atoms. A similar strategy, when applied to TMNPs, can result in the sequential dispersion of the electronic charge among the layers, which can be confirmed by XPS data.³⁰⁵ The electron density



of the surface element in TMNPs could be influenced by the electronic level of elements present within the inner layers. In case the electronic levels of three elements are aligned for enhancing the overall electronic charge shift, TMNPs possessing a triple core/shell structure, a sequential potential field will assist in delivering the highest activity in terms of ligand effect.³⁰⁶ Table 3 gives a summary of the most relevant trimetallic nanostructure-based sensing platforms and their analytical performance.



Table 3. Overview of trimetallic nanostructure-based sensing platforms and their analytical performance.

S.No.	Trimetal	Detection	sample	Type	fabrication Technique	Electrode	Modifier/S ubstrate/ Chromoge nic Substrate	LQD	LOD	Linear range	Sensitiv ity	Ref .
1.	BLG- PtAuPd- RGO	Glucose	Human Serum	Electr oche mical	-	glassy carbon electrode (GCE)	β - lactoglobul in (BLG) and rGO	-	0.13 μ M	0.005 to 9 mM	63.29 μ AmM ⁻¹ cm ⁻² (4.43 μ AmM ⁻¹)	³
2.	AuPtPd nanocom posites	Breast Cancer	Living Cells	Electr oche mical	physical adsorption	GCE	rGO and GCE	-	2 nM	0.005 μ M to 6.5 mM		⁴
3.	PtAuRu nanoparti cles	Caffeic acid	-	Electr oche mical	One-step synthesis	GCE	glassy carbon electrode (GCE)	-	3.9×10^{-7} M	0.0087 mM to 16.6 mM	-	⁵





4.	Pd@Au @Pt nanocomposites	Cancer Biomarkers (CEA and PSA)	Human Serum	Electrochemical	Electrodeposition Method	anti-CEA/EDC/NHS/PdAuPt/COOH-rGO/Au and anti-PSA/EDC/NHS/PdAuPt/COOH-rGO/Au electrodes	Au		8pg ml ⁻¹ (for CEA) and 2 pg ml ⁻¹ (for PSA)	12 pg ml ⁻¹ to 85 ng ml ⁻¹ (for CEA) and 3 pg ml ⁻¹ to 60 ng ml ⁻¹ (for PSA)	0.099 ± 0.007 μA ng ⁻¹ ml (for CEA) and 0.267 ± 0.02 μA ng ⁻¹ ml (for PSA)	⁶
5.	NiFeCo (NFC) nanospheres	Hydrazine	Water samples	Electrochemical	Hydrothermal Method	platinum wire (AE); Ag/AgCl (RE) and GCE, rotating disk electrode (WE)	-	21.6 nM	6.4 nM	0.020–3080 μM	-	⁷

6.	AuPdPt @RGO/ GCE	Retigabine (REG)	Human Plasma and Urine Sample s	Electr oche mical	Wet Chemical Method	platinum wire (AE); Ag/AgCl (RE) and GCE (WE)	rGO	0.003 $\mu\text{g mL}^{-1}$	0.001 $\mu\text{g mL}^{-1}$	2.0– 40.0 \times 10^{-7} M	-	⁸
7.	AgPtCo nanodend rites (NDs)	Cancer Biomarker (serum human epididymi s protein 4 (HE4)	Real Sample s	Electr oche mical	One-step synthesis	MGCE (WE), Pt wire (CE), Ag/AgCl (RE)	Magnetic glassy carbon electrode (MGCE)		0.487 pg mL^{-1}	0.001– 50 ng mL^{-1}	-	⁹
8.	Cu/Au/Pt NPs	Glucose and Cancer	-	Chlor ometr ic	NaBH_4 Co- reduction method	-	-	-	25 μM for Glucose, 200 cells for	0-200 μM for Glucose, 0– 10000 cells for cancer	-	¹⁰



									cancer.			
9.	COOH-AgPtPd/ NH ₂ -rGO NCs	H ₂ O ₂ and prostate-specific antigen (PSA)	Human Serum Samples	Electrochemical	layer-by-layer (LBL) assembly		rGO	-	0.0002 μ M for H ₂ O ₂ and 0.000004 ng mL ⁻¹ for PSA	0.001 to 500 μ M for H ₂ O ₂ and 0.000004 ng mL ⁻¹ to 300 ng mL ⁻¹ for PSA	-	¹¹
10.	PdCoAg NPs	Glucose determination	fruit juices and carbonated beverages	Electrochemical	Polyol method	GCE (WE) Pt wire (CE), Ag/AgCl (RE)			0.003 mmol \cdot L ⁻¹	0.005 to 0.35 mmol \cdot L ⁻¹	4156.34 μ A \cdot mmol ⁻¹ \cdot L \cdot cm ⁻²	¹²

11.	grGO/MoS ₂ -NRs/AuPdAg NCs	ochratoxin A	spiked corn and coffee samples	Electrochemical	layer-by-layer (LBL) assembly	-	rGO	-	0.000 005 ng mL ⁻¹	0.0000 1–150 ng mL ⁻¹	-	¹³
12.	PtAuAg nanotubes	Methanol	Alcoholic Beverages	Electrochemical	Galvanic Replacement	platinum foil (CE) Ag/AgCl (RE), GCE (WE)	-	-	0.02 mM	0.05–1.8 mM	24.3 mA mM ⁻¹ cm ⁻²	¹⁴
13.	PdCuAu NPs	H ₂ O ₂ and Glucose	-	Colorimetric	-	-	TMB	-	5 nM for H ₂ O ₂ and 25 nM for glucose	0.1–300 μM for H ₂ O ₂ and 0.5–500 μM for glucose	-	¹⁵

14.	(Au/Ag/Pd)NPs	ascorbic acid (AA), dopamine (DA), acetaminophen (AP), and tryptophan (TP)	Human Blood Serum	Electrochemical	-	Ag/AgCl (RE), Pt wire (CE), Au/Ag/Pd NPs/EPGrO/GCE, EPGrO/GCE and bare GCE (WE)	rGO	-	0.24 ± 0.03 for AA, 0.02 ± 0.01 for DA, 0.12 ± 0.04 for AP, 0.03 ± 0.01 μM, for TP respe	5–650 Mm for AA, 1–700 μM for DA, 5–700 μM, for AP, 1–600 μM for TP	-	16
-----	---------------	--	-------------------	-----------------	---	---	-----	---	--	---	---	----

									ctivel y			
15.	Cu/Au/Pt NPs	microcystin-LR (MC-LR)	fresh fish tissue and water samples	Color imetri c	NaBH ₄ Co- reduction method	-	TMB	-	3.0 ng L ⁻¹	4.0 - 10000 ng L ⁻¹	-	¹⁷
16.	Au- CF@rGO /GCE modified electrode	dopamine (DA)	Banana Milk Sample s	Electr oche mical	ultrasonicat ion-dry synthesis techniques	Au- CF@rGO/ GCE (WE), Pt rod (CE), Ag AgCl (RE)	rGO	-	0.34 nM	0.001 to 119.6 μM	8.743 μAμM ⁻¹ cm ⁻² .	¹⁸
17.	Au@PdP t Nanocub es	Neuron- Specific Enolase (NSE)	Human Serum	Electr oche mical	-	-	Au@MOFs		4.17 fg mL ⁻¹	10 fg mL ⁻¹ to 100 ng mL ⁻¹	-	¹⁹



18.	Au@Pd @Pt nanoparticles	ractopamine (RAC)	peroxy disulfate/oxygen	electrochemical luminescence (ECL)				-	0.000 03 ng mL ⁻¹	0.0 0 01 to 10 0 0 ng mL ⁻¹	-	²⁰
19.	MoO ₂ - Fe ₃ O ₄ - CuO nanocomposite	para-nitrophenol		Electrochemical	co-precipitation method	Pt wire (CE), MoO ₂ - Fe ₃ O ₄ - CuO/GCE (WE)	Nafion	-	0.2 pM	1.0 pM to 0.01 mM	5.2430 mA mM ⁻¹ cm ⁻²	²¹
20.	MWCNTs-AuPdPt	Staphylococcus aureus	Food Samples (Yogurt ; pure milk; and infant milk	Electrochemical	In situ growth	GCE (WE), Pt wire (AE), and a saturated calomel electrode (RE)	MWCNTs	-	39 CFU mL ⁻¹	1.1 × 102 to 1.1 × 107 CFU mL ⁻¹	-	²²

			powder)									
21.	AuPtPd fluffy- like nanodendrites	cardiac troponin I (cTnI)	Real Sample s	Electrochemical	one-pot thymine-mediated method	-	-	-	3 pg mL ⁻¹	0.01 ~ 100.0 ng mL ⁻¹	-	²³
22.	Co-Ni- Cu-MOF	anticancer agents nilutamide (NLM)	Real serum sample	Electrochemical	Solvothermal method	Co-Ni-Cu-MOF (WE), Ag/AgCl (RE), Pt wire (CE)	Nafion	-	0.48 ± 0.02 nM	0.5–70 μM and 70–900 μM	of 10.712 μA μM ⁻¹ cm ⁻²	²⁴
23.	Ni/Ag/Zn nano-sensor	Dopamine (DA)		Electrochemical	green microwave-assisted co-precipitation reduction method			-	0.3 μM	1 μM- 25 μM	0.96 μA/μM· cm ²	²⁵



24.	P-L-Cys/Au _{1.5} Pt ₁ Co ₁ /GCE NPs	Hydroquinone (HQ)	real water samples (mineral water, tap water, and lake water)	Electrochemical	co-reduction method	a bare or modified GCE (WE), a saturated calomel electrode (SCE) (RE), and a Pt electrode (CE)	P-L-Cys film	-	0.045 μ M,	0.1 to 30 and 0–200 μ M	4.247 μ A μ M ⁻¹ ·cm ⁻²	²⁶
-----	--	-------------------	---	-----------------	---------------------	--	--------------	---	----------------	-----------------------------	---	---------------

Comparison of the electrocatalytic sensitivity of mono-/bi-metallic nanoparticles with TMNPs

The electrocatalytic sensitivity of mono- and bimetallic nanoparticles had been compared with that of trimetallic systems, and clear performance advantages of the latter had been observed across major electrochemical reactions, as shown in **Table 4**. Bimetallic catalysts such as Ni–Fe for OER and Ni–Mo for HER had already exhibited enhanced activity over their monometallic counterparts; however, their overpotentials typically remained in the ranges of 230–320 mV for OER and 60–150 mV for HER at $10 \text{ mA} \cdot \text{cm}^{-2}$. In contrast, trimetallic compositions such as Ni–Fe–Co, Ni–Fe–Mo, and Ni–Mo–Fe had demonstrated further improvements due to additional synergistic effects, showing reduced OER overpotentials of 150–280 mV and HER values as low as 20–120 mV. Similarly, in overall two-electrode water splitting, trimetallic Ni–Fe–Mo electrodes had delivered a lower cell voltage ($\sim 1.45 \text{ V}$) compared to conventional NiFe/NiMo combinations ($\sim 1.6\text{--}1.8 \text{ V}$). In noble-metal systems, Pt–Ni–Co trimetallic catalysts had surpassed Pt/C benchmarks by offering significantly higher ORR mass activity. These improvements were attributed to enhanced electronic modulation, increased active-site density, improved charge-transfer properties, and superior structural stability provided by the third metal. Overall, TMNPs had consistently shown higher electrocatalytic sensitivity and durability than mono- and bimetallic systems, confirming the beneficial role of multi-metallic synergy.^{27,28}

Table 4. Comparison of electrocatalytic sensitivity of monometallic/bimetallic nanoparticles with TMNPs.

Property	Monometallic / Bimetallic NPs	Electrocatalytic sensitivity	Trimetallic NPs	Electrocatalytic sensitivity
OER activity (alkaline)	Bimetallic Ni–Fe (LDH / oxides / derived) — widely used OER benchmark	230–320 mV @ $10 \text{ mA} \cdot \text{cm}^{-2}$ ³⁰⁷	Ni–Fe–Co / Ni–Fe–Mo (oxides, selenides, sulfides)	150–280 mV @ $10 \text{ mA} \cdot \text{cm}^{-2}$ ³⁰⁸



HER activity (alkaline / overall cell cathode)	Ni–Mo (alloys, LDH-derived) — common earth-abundant HER choice	60–150 mV @ 10 mA·cm ⁻² ³⁰⁹	Ni–Mo–Fe / Ni–Mo–Co	20–120 mV @ 10 mA·cm ⁻² ³¹⁰
Two-electrode water-splitting	NiFe (OER) + NiMo (HER) cell	1.6–1.8 V @ 10 mA·cm ⁻² ³¹¹	Ni–Fe–Mo (both electrodes)	1.45 V @ 10 mA·cm ⁻² ³¹²
ORR activity (acid / PEM relevant, Pt-based)	Pt/C industry baseline	0.1–0.5 A·mg ⁻¹ ³¹³	Pt–Ni–Co (trimetallic nanocages / branched)	1.03 A·mg ⁻¹ ³¹⁴
Specific/activity tunability (binding energy / d-band tuning)	Bimetallic gives good tunability vs monometallic (electronic modulation by 2nd metal)	Moderate tunability; can shift adsorption energies and increase active-site density. ³¹⁵	Trimetallic offers higher degrees of electronic tuning (third element enables finer control of active site & stability)	Often higher, enables simultaneous optimization of adsorption energy, conductivity, and corrosion resistance (qualitative advantage; numeric effect depends on system). ³¹⁶
Active site density/surface area	Single- or two-metal systems can be engineered with high surface area (nano-porous, LDH, supports)	Good, but sometimes limited by phase segregation or agglomeration. ³¹⁷	Trimetallic nanoalloys / heterostructures often expose more diverse active sites and prevent	Frequently higher accessible active site variety and synergistic sites, reported to increase intrinsic activity



			agglomeration	per geometric area in many studies. ³¹⁸
Electrical conductivity / charge transfer	Metals or conductive supports provide good conductivity; oxides/hydroxides moderate	Good (metallic), moderate (oxide/hydroxide). ³¹⁹	Third metal often added to improve conductivity (e.g., Mo, Co)	Improved charge transfer / lower R_{ct} frequently reported for trimetallics. ³²⁰
Stability / durability	Monometallic often less stable under harsh conditions; bimetallic usually show improved corrosion resistance	Stability varies: tens to hundreds of hours depending on system and testing protocol. ³²¹	Trimetallic often engineered for higher stability (stabilizing element suppresses dissolution)	Many reports show equal or improved stability (100s of hours possible in optimized electrodes); but depends on support and testing. ³²²
Resistance to poisoning / selectivity	Single metal more susceptible to specific poisons; bimetallic can give improved tolerance	Moderate. https://doi.org/10.1016/j.trac.2024.117757	Trimetallic can tailor surface to resist adsorbates / intermediates	Often better tolerance to specific poisons (qualitative). ³²²
Synthesis complexity & scale-up	Monometallic simplest; bimetallic moderate	Easier to scale for monometallic/bimetallic NPs. ¹⁸⁴	Trimetallic generally more complex (precise composition control,	Higher synthesis complexity; scalable examples exist but require more careful



			phase homogeneity needed)	synthesis/annealing steps. ¹⁸⁴
Cost (material & processing)	Monometallic (earth-abundant) cheapest; Pt-based expensive	Cheaper for earth-abundant metals; Pt is expensive. ³²³	Trimetallic (if noble-metal-free) can be cost-competitive; Pt-containing trimetallic remain costly but use Pt more efficiently	Can lower noble-metal loading by mass-activity improvement. ³²³



Summary

The compiled table (**Table 3**) highlights recent advancements in trimetallic nanomaterial-based sensing platforms across electrochemical and colorimetric techniques. These studies demonstrate the synergistic combinations of three metals significantly enhance catalytic activity, conductivity, selectivity, and analytic performance. As evident from the reported LODs, linear ranges, and sensitivities, trimetallic nanostructures exhibit remarkable detection capabilities for a wide spectrum of analytes, including biomarkers, environmental pollutants, pharmaceuticals, and food contaminants. The versatility of fabrication strategies, ranging from hydrothermal and electrodeposition methods to green synthesis and one-pot routes, further underscores the adaptability of these materials for practical sensing applications. Overall, the summarized literature establishes trimetallic nanomaterials as powerful transducers with strong potential for the next-generation high-performance analytical sensors.

Conclusion

TMNPs have emerged as superior electrocatalysts, outperforming traditional monometallic and bimetallic counterparts in various energy conversion processes, including fuel cells, water splitting, and CO₂ reduction. The synergistic interactions among the three constituent metals lead to a unique electronic structure and optimized binding energies for reaction intermediates, significantly enhancing catalytic activity and selectivity.

1. For instance, Pt-Pd-Au TMNPs have shown remarkable activity in the ORR in PEMFCs, attributed to the modified d-band center and reduced poisoning by intermediates.
2. Similarly, Ni-Co-Fe TMNPs have demonstrated excellent performance in the proton exchange OER due to their high conductivity, large electrochemically active surface area (ECSA), and robust structural integrity under harsh electrochemical conditions.
3. Beyond catalysis, TMNPs have shown exceptional potential in sensing applications, leveraging their unique physicochemical properties. The high surface area, enhanced electron transfer rates, and tunable surface chemistry of TMNPs enable the detection of analytes with high sensitivity, selectivity, and rapid response times. For example, Au-Pt-Pd nanoparticles have been effectively employed in electrochemical sensors for glucose detection, demonstrating superior performance to commercial sensors.



4. Additionally, TMNPs have been utilized in environmental monitoring to detect pollutants such as heavy metals and organic contaminants with high accuracy. Incorporating TMNPs in sensor devices improves detection limits and enhances durability and resistance to fouling, making them ideal for long-term monitoring applications.

Despite the numerous advancements, several challenges associated with utilization of TMNPs are yet to be addressed -

1. One such major challenge is the complexity involved in their synthesis procedures. The production of TMNPs often demands precise control over various criteria, including reaction conditions, stabilizing agents, and ratios of different metals. The involvement of numerous parameters often results in variations in shape, size and operational properties of the TMNPs, thereby generating non-reproducible results with reduced stability.
2. Lower precision in controlling size, shape and distribution employing conventional methods such as co-reduction, impregnation, and sol-gel techniques for the synthesis of TMNPs.
3. Gaining ample interpretation regarding synergistic effects between different metals in TMNPs is another persistent challenge that has limited their utilisation in electrocatalytic applications.
4. Low compatibility with existing industrial processes, hindering the development of robust protocols for integrating TMNPs into commercial devices.
5. There is a lack of characterization techniques for understanding the constituents and particle makeup, and only a handful of reports based on machine learning (ML) approach are available.
6. Few reports focusing are available highlighting the role of individual elements involved towards promoting activity many of which have various inconsistencies, mainly in high-entropy systems.
7. Another major hurdle is gaining control over elemental distribution, phase purity, and surface termination, all of which are highly essential parameters while designing application-specific TMNPs.

Recent innovations have introduced advanced techniques such as seed-mediated growth, galvanic replacement, and atomic layer deposition (ALD). The adoption of these sophisticated methods



offers unparalleled control over nanoparticle morphology, composition, and crystallinity. For instance, seed-mediated growth enables the formation of core-shell structures with controlled thickness. At the same time, ALD allows for atomic-level precision in layering different metals, thus tailoring the surface properties for specific catalytic reactions. Such advancements have paved the way for designing TMNPs with enhanced surface area, active sites, and stability, which are crucial for high-performance applications.

The evolution of trimetallic nanoparticles (TMNPs) has marked a significant milestone in nanotechnology, characterized by groundbreaking advancements in synthesis methodologies, electrocatalytic performance, and sensing capabilities.³²⁴ In the current research scenario, various electrochemical-based applications, including H₂O₂ generation, HER, overall water splitting, drug degradation, electrochemical synthesis, supercapacitors, and battery-based applications involving the utilization of 2D materials, are being extensively explored.^{325,326,327} The journey from rudimentary synthesis techniques to sophisticated, precise control over nanoparticle morphology and composition has been pivotal in optimizing catalytic activity and enhancing the overall functional properties of TMNPs.^{328,329,330}

Future perspectives

Continued research into alternative, cost-effective synthesis methods, such as green chemistry approaches and bio-templates, is being adopted for reducing production costs and environmental impact. Additionally, advancements in computational modelling and machine learning can accelerate the discovery and optimization of new TMNP compositions and structures, tailoring them for specific applications as shown in Fig.17. In summary, the multifaceted capabilities of TMNPs underscore their pivotal role in advancing fundamental research and practical applications.



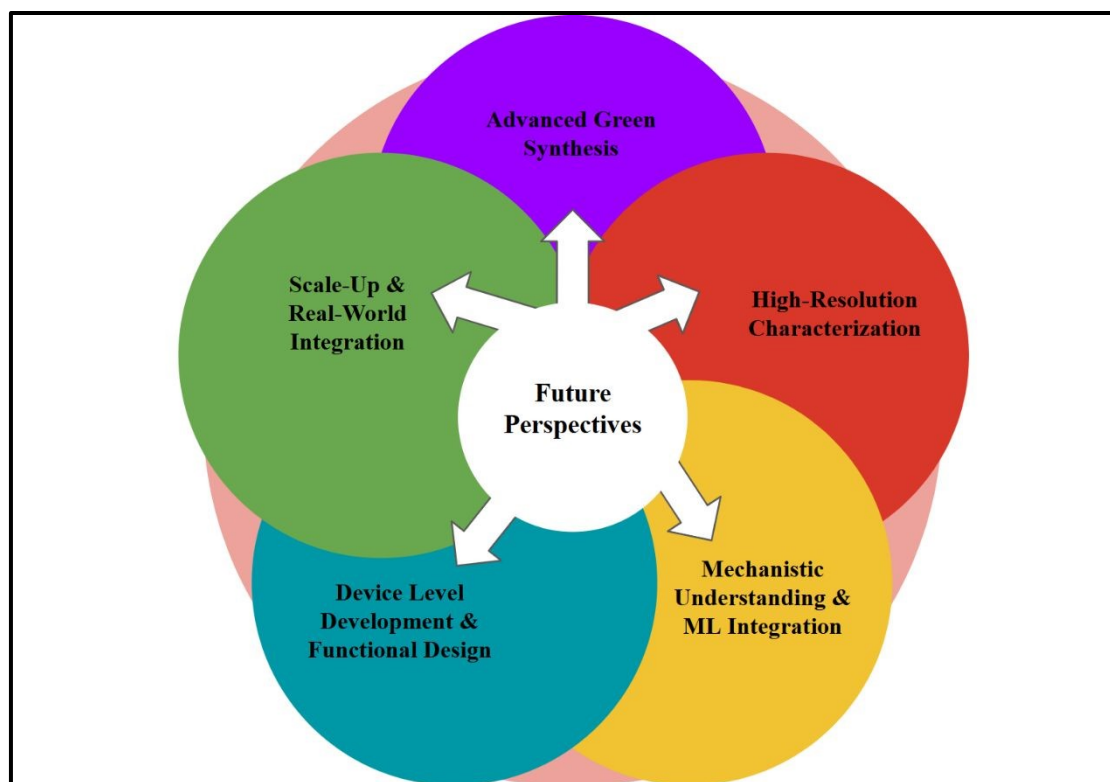


Fig. 17 A Schematic map for the future trajectory in research for TMNPs: from advanced green synthesis methods, followed by advanced high-resolution and in-situ characterization, mechanistic understanding aided by machine learning, device integration, and deployable, scalable real-world applications.

Their superior electrocatalytic performance and exceptional sensing capabilities make them promising candidates for next-generation technologies for sustainable development and precision diagnostics. Utilization of advanced characterization techniques, including in situ /operando studies, can be used for tracking structural and electronic variations occurring during reactions with respect to the catalytic performance and to establish direct links between structure and function. Incorporation of ML/deep learning can help in initial theoretical screening followed by rational design of catalysts and subsequently optimise various parameters, such as the d-band center, which directly influences the reactivity. In case of applications demanding structural advantages, making ambient use of the flexibility and structural stability of TMNPs can prove to be highly instrumental in conditions where consistency and long-term stability are essential. Similarly, TMNPs can be ideal candidates for applications requiring interfacial or multifunctional catalysis as they can improve synergistic effects at interfaces, causing an overall upliftment in



catalytic performance and durability. As we continue to refine synthesis techniques, enhance catalytic properties, and expand their functional applications, TMNPs hold the potential to revolutionize various technological domains. Developing automated testing platforms for experimentally substantiating theoretical predictions and constructing a comprehensive structure–activity dataset could be highly beneficial. By addressing current challenges through collaborative, interdisciplinary efforts, we can unlock the full potential of TMNPs, driving innovation and fostering their integration into diverse applications for a sustainable future.

The authors declare that they have no known competing financial interests or personal relationships that could have appeared to influence the work reported in this article.

Acknowledgements

The authors thank CHRIST University for providing the necessary facilities for conducting this work.

Disclosure statement

The authors declare that they have no known competing financial interests or personal relationships that could have appeared to influence the work reported in this article.

Funding

No funding was acquired for this review work



References

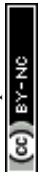
- 1 H. Du, O. U. Akakuru, C. Yao, F. Yang and A. Wu, *Transl Oncol*, 2022, **15**, 101264.
- 2 A. Selmani, D. Kovačević and K. Bohinc, *Adv Colloid Interface Sci*, 2022, **303**, 102640.
- 3 P. K. Dikshit, J. Kumar, A. K. Das, S. Sadhu, S. Sharma, S. Singh, P. K. Gupta and B. S. Kim, *Catalysts*, DOI:10.3390/CATAL11080902.
- 4 X. Ye, X. He, Y. Lei, J. Tang, Y. Yu, H. Shi and K. Wang, *Chemical Communications*, 2019, **55**, 2321–2324.
- 5 M. A. Emamhadi, M. Sarafraz, M. Akbari, V. N. Thai, Y. Fakhri, N. T. T. Linh and A. Mousavi Khaneghah, *Food and Chemical Toxicology*, 2020, **146**, 111825.
- 6 S. Ali, A. S. Sharma, W. Ahmad, M. Zareef, M. M. Hassan, A. Viswadevarayalu, T. Jiao, H. Li and Q. Chen, *Crit Rev Anal Chem*, 2021, **51**, 454–481.
- 7 R. Rajeev, R. Datta, A. Varghese, Y. N. Sudhakar and L. George, *Microchemical Journal*, 2021, **163**, 105910.
- 8 U. Shedbalkar, R. Singh, S. Wadhvani, S. Gaidhani and B. A. Chopade, *Adv Colloid Interface Sci*, 2014, **209**, 40–48.
- 9 A. T. Mathew, V. S. Bhat, A. K. B, S. S, M. T, A. Varghese and G. Hegde, *Electrochim Acta*, 2020, **354**, 136624.
- 10 M. Shah, D. Fawcett, S. Sharma, S. K. Tripathy and G. E. J. Poinern, *Materials 2015, Vol. 8, Pages 7278-7308*, 2015, **8**, 7278–7308.
- 11 H. You, S. Yang, B. Ding and H. Yang, *Chem Soc Rev*, 2013, **42**, 2880–2904.
- 12 N. Kulkarni and U. Muddapur, *J Nanotechnol*, DOI:10.1155/2014/510246.
- 13 W. Wang, Y. Cai, P. Tian, J. Xu and F. Xuan, *J Colloid Interface Sci*, 2025, **698**, 138046.
- 14 Y. C. Cheng, Y. Q. Dou and T. S. Deng, *Journal of Nanoparticle Research 2025 27:7*, 2025, **27**, 177-.
- 15 A. H. Hashem, E. Saied, B. M. Badr, M. S. Dora, M. A. Diab, A. M. Abdelaziz, F. M. Elkady, M. A. Ali, N. I. Issa, Z. A. Hamdy, M. E. Nafea, A. N. Khalifa, A. Adel, A. Hasib, A. M. Hawela, M. M. El-Gazzar, M. A. Nouh, A. A. Nahool and M. S. Attia, *Archives of Microbiology 2025 207:3*, 2025, **207**, 50-.
- 16 T. S. Merjan and Z. T. A. Ali, *Desalination Water Treat*, 2025, **322**, 101082.



- 17 K. Aranishi, H. L. Jiang, T. Akita, M. Haruta and Q. Xu, *Nano Res*, 2011, **4**, 1233–1241.
- 18 M. Tang, S. Luo, K. Wang, H. Du, R. Sriphathoorat and P. Shen, *Nano Res*, 2018, **11**, 4786–4795.
- 19 S. Khanal, N. Bhattarai, J. J. Velázquez-Salazar, D. Bahena, G. Soldano, A. Ponce, M. M. Mariscal, S. Mejía-Rosales and M. José-Yacamán, *Nanoscale*, 2013, **5**, 12456–12463.
- 20 P. dos Santos Araújo, G. B. Belini, G. P. Mambrini, F. M. Yamaji and W. R. Waldman, *Int J Biol Macromol*, 2019, **140**, 749–760.
- 21 G. Allaedini, S. M. Tasirin and P. Aminayi, *Chemical Papers*, 2015, **70**, 231–242.
- 22 X. L. Cai, C. H. Liu, J. Liu, Y. Lu, Y. N. Zhong, K. Q. Nie, J. L. Xu, X. Gao, X. H. Sun and S. D. Wang, *Nanomicro Lett*, 2017, **9**, 1–10.
- 23 W. T. Ralston, W. C. Liu, S. Alayoglu and G. Melaet, *Topics in Catalysis 2018 61:9*, 2018, **61**, 1002–1015.
- 24 I. Shmarakov, I. Mukha, N. Vityuk, V. Borschovetska, N. Zhyshchynska, G. Grodzyuk and A. Eremenko, *Nanoscale Res Lett*, 2017, **12**, 1–10.
- 25 K. Suwannarat, K. Thongthai, S. Ananta and L. Srisombat, *Colloids Surf A Physicochem Eng Asp*, 2018, **540**, 73–80.
- 26 K. Chatterjee, J. M. Howe, W. C. Johnson and M. Murayama, *Acta Mater*, 2004, **52**, 2923–2935.
- 27 W. He, J. Cai, H. Zhang, L. Zhang, X. Zhang, J. Li and J. J. Yin, *ACS Appl Nano Mater*, 2018, **1**, 222–231.
- 28 M. Tsuji, M. Matsunaga, H. Kumagai, M. Ogino, S. Hikino, Y. Yoshida and T. Ishizaki, *CrystEngComm*, 2013, **15**, 1345–1351.
- 29 X. Zhang, F. Zhang and K. Y. Chan, *Catal Commun*, 2004, **5**, 749–753.
- 30 B. Li and S. H. Chan, *Int J Hydrogen Energy*, 2013, **38**, 3338–3345.
- 31 Y. Y. Shen, Y. Sun, L. N. Zhou, Y. J. Li and E. S. Yeung, *J Mater Chem A Mater*, 2014, **2**, 2977–2984.
- 32 H. Zhang, L. Lu, Y. Cao, S. Du, Z. Cheng and S. Zhang, *Mater Res Bull*, 2014, **49**, 393–398.
- 33 M. A. Matin, J. H. Jang and Y. U. Kwon, *Int J Hydrogen Energy*, 2014, **39**, 3710–3718.
- 34 Z. L. Wang, Y. Ping, J. M. Yan, H. L. Wang and Q. Jiang, *Int J Hydrogen Energy*, 2014, **39**, 4850–4856.



- 35 J. Tayal, B. Rawat and S. Basu, *Int J Hydrogen Energy*, 2011, **36**, 14884–14897.
- 36 Z. Khan, *Int J Hydrogen Energy*, 2019, **44**, 11503–11513.
- 37 C. V. Rao and B. Viswanathan, *Journal of Physical Chemistry C*, 2010, **114**, 8661–8667.
- 38 B. Karthikeyan and M. Murugavelu, *Sens Actuators B Chem*, 2012, **163**, 216–223.
- 39 P. P. Fang, S. Duan, X. D. Lin, J. R. Anema, J. F. Li, O. Buriez, Y. Ding, F. R. Fan, D. Y. Wu, B. Ren, Z. L. Wang, C. Amatore and Z. Q. Tian, *Chem Sci*, 2011, **2**, 531–539.
- 40 R. M. Navarro, M. A. Peña, C. Merino and J. L. G. Fierro, *Topics in Catalysis* 2004 30:1, 2004, **30**, 481–486.
- 41 X. Zhang, F. Zhang and K. Y. Chan, *Catal Commun*, 2004, **5**, 749–753.
- 42 J. Y. Lee, D. H. Kwak, Y. W. Lee, S. Lee and K. W. Park, *Physical Chemistry Chemical Physics*, 2015, **17**, 8642–8648.
- 43 C. Venkateswara Rao and B. Viswanathan, *J Colloid Interface Sci*, 2012, **367**, 337–341.
- 44 Y. Suo, L. Zhuang and J. Lu, *Angewandte Chemie*, 2007, **119**, 2920–2922.
- 45 W. Hong, Y. Liu, J. Wang and E. Wang, *J Power Sources*, 2013, **241**, 751–755.
- 46 J. De Deken, P. G. Menon, G. F. Froment and G. Haemers, *J Catal*, 1981, **70**, 225–229.
- 47 M. C. J. Bradford and M. A. Vannice, *J Catal*, 1998, **173**, 157–171.
- 48 G. Sharma, D. Kumar, A. Kumar, A. H. Al-Muhtaseb, D. Pathania, M. Naushad and G. T. Mola, *Materials Science and Engineering C*, 2017, **71**, 1216–1230.
- 49 Z. Khan, S. A. AL-Thabaiti and M. Z. A. Rafiquee, *Int J Hydrogen Energy*, 2021, **46**, 39754–39767.
- 50 S. Akhter, N. K. Mohd Zain, M. Shalauddin, V. K. Singh, I. I. Misnon, R. K. Sharma, S. Das, W. J. Basirun, M. R. Johan and R. Jose, *Sens Actuators A Phys*, 2021, **325**, 112711.
- 51 S. Hagos Gebre and M. Getaye Sendeku, *Journal of Energy Chemistry*, 2022, **65**, 329–351.
- 52 D. Yao, Y. Wang, Y. Li, A. Li, Z. Zhen, J. Lv, F. Sun, R. Yang, J. Luo, Z. Jiang, Y. Wang and X. Ma, *Nature Communications* 2023 14:1, 2023, **14**, 1–11.
- 53 H. Zhang, M. Okumura and N. Toshima, *Journal of Physical Chemistry C*, 2011, **115**, 14883–14891.



- 54 K. H. Huynh, X. H. Pham, J. Kim, S. H. Lee, H. Chang, W. Y. Rho and B. H. Jun, *Int J Mol Sci*, 2020, **21**, 1–29.
- 55 I. Ijaz, E. Gilani, A. Nazir and A. Bukhari, <http://mc.manuscriptcentral.com/tgcl>, 2020, **13**, 59–81.
- 56 R. Ferrando, J. Jellinek and R. L. Johnston, *Chem Rev*, 2008, **108**, 845–910.
- 57 C. Pannu, M. Bala, S. A. Khan, S. K. Srivastava, D. Kabiraj and D. K. Avasthi, *RSC Adv*, 2015, **5**, 92080–92088.
- 58 K. W. Park, Y. E. Sung and M. F. Toney, *Electrochem commun*, 2006, **8**, 359–363.
- 59 G. Sharma, A. Kumar, S. Sharma, M. Naushad, R. Prakash Dwivedi, Z. A. ALOthman and G. T. Mola, *J King Saud Univ Sci*, 2019, **31**, 257–269.
- 60 G. Liu, L. Peng, L. Fan, J. Wang, Y. Fu, L. Cao and W. Wu, *Catalysis Surveys from Asia*, 2022, **26**, 183–192.
- 61 M. Zhu, M. T. Nguyen, W. J. Sim and T. Yonezawa, *Mater Adv*, DOI:10.1039/d2ma00688j.
- 62 P. Srinoi, Y. T. Chen, V. Vittur, M. D. Marquez and T. R. Lee, *Applied Sciences* 2018, Vol. 8, Page 1106, 2018, **8**, 1106.
- 63 P. Gao, Y. Cai, F. Wang, H. Zhu and M. Pu, *Int J Hydrogen Energy*, 2020, **45**, 16039–16048.
- 64 M. Hafezi Kahnamouei and S. Shahrokhian, *ACS Appl Mater Interfaces*, 2020, **12**, 16250–16263.
- 65 R. Wang, T. Hughes, S. Beck, S. Vakil, S. Li, P. Pantano and R. K. Draper, <https://doi.org/10.3109/17435390.2012.736547>, 2012, **7**, 1272–1281.
- 66 V. Elayappan, S. Muthusamy, G. Mayakrishnan, R. Balasubramaniam, Y. S. Lee, H. S. Noh, D. Kwon, M. M. Mussa and H. Lee, *Appl Surf Sci*, 2020, **531**, 147415.
- 67 Y. Wen, F. Ren, T. Bai, H. Xu and Y. Du, *Colloids Surf A Physicochem Eng Asp*, 2018, **537**, 418–424.
- 68 N. Basavegowda, K. Mishra and Y. R. Lee, *J Alloys Compd*, 2017, **701**, 456–464.
- 69 I. Călinescu, D. Martin, D. Ighigeanu, A. I. Gavrilă, A. Trifan, M. Patrascu, C. Munteanu, A. Diacon, E. Manaila and G. Craciun, *Central European Journal of Chemistry*, 2014, **12**, 774–781.
- 70 A. G. M. Da Silva, T. S. Rodrigues, S. J. Haigh and P. H. C. Camargo, *Chemical Communications*, 2017, **53**, 7135–7148.
- 71 R. G. Weiner and S. E. Skrabalak, *Chemistry of Materials*, 2016, **28**, 4139–4142.



- 72 K. Ding, Y. Li, Y. Zhao, J. Zhao, Y. Chen and Q. Wang, *Int. J. Electrochem. Sci*, 2015, **10**, 8844–8857.
- 73 K. Bhunia, S. Khilari and D. Pradhan, *Dalton Transactions*, 2017, **46**, 15558–15566.
- 74 S. Park, D. Yoon, H. Baik and K. Lee, *CrystEngComm*, 2015, **17**, 6852–6856.
- 75 P. Qiao, S. Xu, D. Zhang, R. Li, S. Zou, J. Liu, W. Yi, J. Li and J. Fan, *Chemical Communications*, 2014, **50**, 11713–11716.
- 76 B. Sen, B. Demirkan, A. Şavk, S. Karahan Gülbay and F. Sen, *Int J Hydrogen Energy*, 2018, **43**, 17984–17992.
- 77 X. Zhang, F. Zhang and K. Y. Chan, *Catal Commun*, 2004, **5**, 749–753.
- 78 K. Eid, Y. H. Ahmad, H. Yu, Y. Li, X. Li, S. Y. AlQaradawi, H. Wang and L. Wang, *Nanoscale*, 2017, **9**, 18881–18889.
- 79 X. Wang, F. Zhu, Y. He, M. Wang, Z. Zhang, Z. Ma and R. Li, *J Colloid Interface Sci*, 2016, **468**, 200–210.
- 80 Z. Razmara and F. Razmara, <https://doi.org/10.1080/24701556.2019.1599400>, 2019, **49**, 163–168.
- 81 S. H. Gebre, *New Journal of Chemistry*, 2022, **46**, 5438–5459.
- 82 H. B. Ahmed, *Int J Biol Macromol*, 2019, **140**, 265–277.
- 83 B. Karthikeyan and B. Loganathan, *Journal of Nanoparticles*, DOI:10.1155/2013/168916.
- 84 D. C. Onwudiwe, *Heliyon*, 2019, **5**, e01413.
- 85 A. A. Womiloju, C. Höppener, U. S. Schubert, S. Hoepfner, A. A. Womiloju, U. S. Schubert, S. Hoepfner and C. Höppener, *Particle & Particle Systems Characterization*, 2020, **37**, 2000019.
- 86 T. S. Alomar, N. AlMasoud, G. Sharma, Z. A. AlOthman and M. Naushad, *J Mol Liq*, 2021, **336**, 116274.
- 87 N. Yadav, A. K. Jaiswal, K. K. Dey, V. B. Yadav, G. Nath, A. K. Srivastava and R. R. Yadav, *Mater Chem Phys*, 2018, **218**, 10–17.
- 88 P. Basumatary, U. H. Lee, D. Konwar and Y. S. Yoon, *Int J Hydrogen Energy*, 2020, **45**, 32770–32779.
- 89 B. Safdar, I. R. Jo, S. H. Kang and K. S. Ahn, *Appl Surf Sci*, 2020, **530**, 147251.



- 90 X. Y. Wang, Y. G. Feng, A. J. Wang, L. P. Mei, X. Luo, Y. Xue and J. J. Feng, *Bioelectrochemistry*, 2021, **140**, 107802.
- 91 D. Ying, Y. Li, R. Ding, W. Shi, Q. Xu, Y. Huang, Z. Jia, W. Yu, X. Sun, P. Gao, E. Liu and X. Wang, *Adv Funct Mater*, 2021, **31**, 1–14.
- 92 A. Tyagi, Y. K. Penke, P. Sinha, I. Malik, K. K. Kar, J. Ramkumar and H. Yokoi, *Int J Hydrogen Energy*, 2021, **46**, 22434–22445.
- 93 S. Ravichandran, N. Bhuvanendran, Q. Xu, T. Maiyalagan and H. Su, *Electrochim Acta*, 2021, **394**, 139148.
- 94 K. Peng, N. Bhuvanendran, S. Ravichandran, W. Zhang, Q. Ma, L. Xing, Q. Xu, L. Khotseng and H. Su, *Int J Hydrogen Energy*, 2020, **45**, 22752–22760.
- 95 A. Elsheikh and J. McGregor, *Nanomaterials*, DOI:10.3390/nano11092244.
- 96 M. A. Zeb Gul Sial, M. A. Ud Din and X. Wang, *Chem Soc Rev*, 2018, **47**, 6175–6200.
- 97 H. Xu, H. Shang, C. Wang and Y. Du, *Adv Funct Mater*, 2020, **30**, 2006317.
- 98 H. B. Ahmed and H. E. Emam, *Polym Test*, 2020, **89**, 106720.
- 99 C. Chen, T. Song, H. Shang, Q. Liu, M. Yuan, C. Wang and Y. Du, *Int J Hydrogen Energy*, 2020, **45**, 26920–26928.
- 100 X. Yang, L. T. Roling, M. Vara, A. O. Elnabawy, M. Zhao, Z. D. Hood, S. Bao, M. Mavrikakis and Y. Xia, *Nano Lett*, 2016, **16**, 6644–6649.
- 101 J. Cai, Y. Zeng and Y. Guo, *J Power Sources*, 2014, **270**, 257–261.
- 102 Q. Qiu, N. Jiang, L. Ge, X. Li and X. Chen, *J Mater Sci*, 2020, **55**, 15681–15694.
- 103 S. Shahrokhian and S. Rezaee, *Electroanalysis*, 2017, **29**, 2591–2601.
- 104 S. Devarajan, P. Bera and S. Sampath, *J Colloid Interface Sci*, 2005, **290**, 117–129.
- 105 L. P. Singh, S. K. Bhattacharyya, R. Kumar, G. Mishra, U. Sharma, G. Singh and S. Ahalawat, *Adv Colloid Interface Sci*, 2014, **214**, 17–37.
- 106 D. C. O. Cdo, Z. Nanoparticles, G. E. Process and H. M. Marwani, .
- 107 J. M. Gonçalves, I. S. Lima, N. F. B. Azeredo, D. P. Rocha, A. de Siervo and L. Angnes, *Front Mater*, 2021, **8**, 1–12.
- 108 Y. Shi and B. Zhang, *Chem Soc Rev*, 2016, **45**, 1529–1541.



- 109 J. Conti, P. Holtberg, J. Diefenderfer, A. LaRose, J. T. Turnure and L. Westfall, DOI:10.2172/1296780.
- 110 B. Liu, Y. F. Zhao, H. Q. Peng, Z. Y. Zhang, C. K. Sit, M. F. Yuen, T. R. Zhang, C. S. Lee and W. J. Zhang, *Advanced Materials*, 2017, **29**, 1606521.
- 111 D. Liu, X. Li, S. Chen, H. Yan, C. Wang, C. Wu, Y. A. Haleem, S. Duan, J. Lu, B. Ge, P. M. Ajayan, Y. Luo, J. Jiang and L. Song, *Nature Energy* 2019 4:6, 2019, **4**, 512–518.
- 112 M. Li, J. Wang, F. Wang, Y. Zhai, X. Zhang, H. Lv, T. Yu and G. Lv, *Appl Surf Sci*, 2021, **568**, 150900.
- 113 M. Liu, R. Zhang and W. Chen, *Chem Rev*, 2014, **114**, 5117–5160.
- 114 M. K. Debe, *Nature* 2012 486:7401, 2012, **486**, 43–51.
- 115 H. Yang, Y. Ko, W. Lee, A. Züttel and W. Kim, *Mater Today Energy*, 2019, **13**, 374–381.
- 116 R. von Helmolt and U. Eberle, *J Power Sources*, 2007, **165**, 833–843.
- 117 W. Niu, Y. Gao, W. Zhang, N. Yan and X. Lu, *Angewandte Chemie International Edition*, 2015, **54**, 8271–8274.
- 118 W. Du, G. Yang, E. Wong, N. A. Deskins, A. I. Frenkel, D. Su and X. Teng, *J Am Chem Soc*, 2014, **136**, 10862–10865.
- 119 Y. C. Shi, J. J. Feng, X. X. Lin, L. Zhang, J. Yuan, Q. L. Zhang and A. J. Wang, *Electrochim Acta*, 2019, **293**, 504–513.
- 120 S. Jing, X. Guo and Y. Tan, *J Mater Chem A Mater*, 2016, **4**, 7950–7961.
- 121 M. F. R. Hanifah, J. Jaafar, M. H. D. Othman, A. F. Ismail, M. A. Rahman, N. Yusof, F. Aziz and N. A. Rahman, *J Alloys Compd*, 2019, **793**, 232–246.
- 122 Y. Zhou, M. Niu, S. Zhu, Y. Liang, Z. Cui, X. Yang and A. Inoue, *Electrochim Acta*, 2019, **296**, 397–406.
- 123 H. Xu, J. Wang, B. Yan, S. Li, C. Wang, Y. Shiraishi, P. Yang and Y. Du, *Nanoscale*, 2017, **9**, 17004–17012.
- 124 S. Zhang, L. Liu, J. Yang, Y. Zhang, Z. Wan and L. Zhou, *Appl Surf Sci*, 2019, **492**, 617–625.
- 125 P. Song, L. Liu, A. J. Wang, X. Zhang, S. Y. Zhou and J. J. Feng, *Electrochim Acta*, 2015, **164**, 323–329.
- 126 F. Wang, J. Qiao, J. Wang, H. Wu, Z. Wang, W. Sun and K. Sun, *J Alloys Compd*, 2019, **811**, 151882.



- 127 X. Yu and P. G. Pickup, *J Power Sources*, 2008, **182**, 124–132.
- 128 T. Gunji and F. Matsumoto, *Inorganics (Basel)*, DOI:10.3390/INORGANICS7030036.
- 129 S. Yao, G. Li, C. Liu and W. Xing, *J Power Sources*, 2015, **284**, 355–360.
- 130 C. Li, Q. Yuan, B. Ni, T. He, S. Zhang, Y. Long, L. Gu and X. Wang, *Nature Communications* 2018 9:1, 2018, **9**, 1–9.
- 131 S. Luo and P. K. Shen, *ACS Nano*, 2017, **11**, 11946–11953.
- 132 N. Abbasi, P. Shahbazi and A. Kiani, *J Mater Chem A Mater*, 2013, **1**, 9966–9972.
- 133 B. Ulas, A. Caglar, A. Kivrak, N. Aktas and H. Kivrak, *Ionics (Kiel)*, 2020, **26**, 3109–3121.
- 134 X. Weng, Q. Liu, J. J. Feng, J. Yuan and A. J. Wang, *J Colloid Interface Sci*, 2017, **504**, 680–687.
- 135 S. Luo and P. K. Shen, *ACS Nano*, 2017, **11**, 11946–11953.
- 136 H. Xu, B. Yan, K. Zhang, J. Wang, S. Li, C. Wang, Y. Shiraishi, Y. Du and P. Yang, *Int J Hydrogen Energy*, 2017, **42**, 20720–20728.
- 137 B. Ulas, A. Caglar, O. Sahin and H. Kivrak, *J Colloid Interface Sci*, 2018, **532**, 47–57.
- 138 S. Luo, W. Chen, Y. Cheng, X. Song, Q. Wu, L. Li, X. Wu, T. Wu, M. Li, Q. Yang, K. Deng and Z. Quan, *Advanced Materials*, 2019, **31**, 1903683.
- 139 L. Y. Zhang, X. Meng, H. Wu, F. Wang, H. Huang, Y. Ouyang, W. Yuan, C. X. Guo and C. M. Li, *Mater Today Energy*, DOI:10.1016/j.mtener.2020.100558.
- 140 A. Pei, L. Ruan, B. Liu, W. Chen, S. Lin, B. Chen, Y. Liu, L. H. Zhu and B. H. Chen, *Int J Hydrogen Energy*, 2020, **45**, 22893–22905.
- 141 X. Hu, J. Zou, H. Gao and X. Kang, *J Colloid Interface Sci*, 2020, **570**, 72–79.
- 142 Z. Zhang, D. Fang, H. Yang, J. Liu and F. Liu, *ACS Appl Nano Mater*, 2025, **8**, 8283–8293.
- 143 S. Z. Jilani, C. P. Cohen, E. E. Iyanobor, D. Zager, R. Zheng, K. M. Frankenfield and Y. Y. J. Tong, *Langmuir*, 2020, **36**, 5902–5907.
- 144 M. Li, D. A. Cullen, K. Sasaki, N. S. Marinkovic, K. More and R. R. Adzic, *J Am Chem Soc*, 2013, **135**, 132–141.
- 145 W. Chen, Y. Zhang and X. Wei, *Int J Hydrogen Energy*, 2015, **40**, 1154–1162.
- 146 R. O'Hayre, S.-W. Cha, W. Colella and F. B. Prinz, *Fuel Cell Fundamentals*, 2016, 481–516.



- 147 A. Brouzgou, A. Podias and P. Tsiakaras, *Journal of Applied Electrochemistry* 2012 43:2, 2012, **43**, 119–136.
- 148 T. Jurzinsky, E. D. Gomez-Villa, M. Kübler, M. Bruns, P. Elsässer, J. Melke, F. Scheiba and C. Cremers, *Electrochim Acta*, 2019, **298**, 884–892.
- 149 A. N. Geraldes, D. F. Da Silva, L. G. D. A. E Silva, E. V. Spinacé, A. O. Neto and M. C. Dos Santos, *J Power Sources*, 2015, **293**, 823–830.
- 150 M. H. M. T. Assumpção, S. G. Da Silva, R. F. B. De Souza, G. S. Buzzo, E. V. Spinacé, M. C. Santos, A. O. Neto and J. C. M. Silva, *J Power Sources*, 2014, **268**, 129–136.
- 151 H. Lv, L. Sun, L. Zou, D. Xu, H. Yao and B. Liu, *Chem Sci*, 2019, **10**, 1986–1993.
- 152 R. M. Castagna, J. M. Sieben, A. E. Alvarez, M. D. Sanchez and M. M. E. Duarte, *Mater Today Energy*, 2020, **15**, 100366.
- 153 C. V. S. Almeida, G. Tremiliosi-Filho, K. I. B. Eguiluz and G. R. Salazar-Banda, *J Catal*, 2020, **391**, 175–189.
- 154 G. Ren, Z. Zhang, Y. Liu, Y. Liang, X. Zhang, S. Wu and J. Shen, *J Alloys Compd*, 2020, **830**, 154671.
- 155 T. Song, F. Gao, L. Jin, Y. Zhang, C. Wang, S. Li, C. Chen and Y. Du, *J Colloid Interface Sci*, 2020, **560**, 802–810.
- 156 B. Yang, T. Qin, Z. Bao, W. Lu, J. Dong, D. Bin and H. Lu, *Nanomaterials*, DOI:10.3390/nano11123174.
- 157 M. B. Gawande, A. Goswami, T. Asefa, H. Guo, A. V. Biradar, D. L. Peng, R. Zboril and R. S. Varma, *Chem Soc Rev*, 2015, **44**, 7540–7590.
- 158 L. Lu, S. Chen, S. Thota, X. Wang, Y. Wang, S. Zou, J. Fan and J. Zhao, *Journal of Physical Chemistry C*, 2017, **121**, 19796–19806.
- 159 F. Nosheen, B. Ni, X. Xu, H. Yang, Z. Zhang and X. Wang, *Nanoscale*, 2016, **8**, 13212–13216.
- 160 C. Dai, Y. Yang, Z. Zhao, A. Fisher, Z. Liu and D. Cheng, *Nanoscale*, 2017, **9**, 8945–8951.
- 161 C. Wang, L. Zhang, H. Yang, J. Pan, J. Liu, C. Dotse, Y. Luan, R. Gao, C. Lin, J. Zhang, J. P. Kilcrease, X. Wen, S. Zou and J. Fang, *Nano Lett*, 2017, **17**, 2204–2210.
- 162 B. Narayanamoorthy, K. K. R. Datta, M. Eswaramoorthy and S. Balaji, *ACS Catal*, 2014, **4**, 3621–3629.



- 163 Y. Liu, Z. Chen, C. Liu, J. Zhang, X. Han, C. Zhong, D. Rao, Y. Wang, W. Hu and Y. Deng, *ACS Appl Energy Mater*, 2019, **2**, 1588–1593.
- 164 M. Zeng, X. X. Wang, Z. H. Tan, X. X. Huang and J. N. Wang, *J Power Sources*, 2014, **264**, 272–281.
- 165 Y. Yang, J. J. Du, L. M. Luo, R. H. Zhang, Z. X. Dai and X. W. Zhou, *Electrochim Acta*, 2016, **212**, 966–972.
- 166 J. M. Zhang, J. J. He, X. Q. Wang, Y. J. Fan, X. J. Zhang, J. P. Zhong, W. Chen and S. G. Sun, *Int J Hydrogen Energy*, 2019, **44**, 28709–28719.
- 167 J. Zhu, M. Xiao, K. Li, C. Liu and W. Xing, *Chemical Communications*, 2015, **51**, 3215–3218.
- 168 H. Liu, X. Liu, Y. Li, Y. Jia, Y. Tang and Y. Chen, *Nano Res*, 2016, **9**, 3494–3503.
- 169 H. Li, Y. Pan, D. Zhang, Y. Han, Z. Wang, Y. Qin, S. Lin, X. Wu, H. Zhao, J. Lai, B. Huang and L. Wang, *J Mater Chem A Mater*, 2020, **8**, 2323–2330.
- 170 Y. Xu, Y. Li, X. Qian, D. Yang, X. Chai, Z. Wang, X. Li, L. Wang and H. Wang, *Nanoscale*, 2019, **11**, 4781–4787.
- 171 C. Li, H. Wang, Y. Li, H. Yu, S. Yin, H. Xue, X. Li, Y. Xu and L. Wang, *Nanotechnology*, 2018, **29**, 255404–255421.
- 172 B. Jiang, C. Li, M. Imura, J. Tang, Y. Yamauchi, B. Jiang, C. Li, M. Imura, J. Tang and Y. Yamauchi, *Advanced Science*, 2015, **2**, 1500112.
- 173 B. Jiang, H. Ataee-Esfahani, C. Li, S. M. Alshehri, T. Ahamad, J. Henzie and Y. Yamauchi, *Chemistry – A European Journal*, 2016, **22**, 7174–7178.
- 174 B. Jiang, C. Li, V. Malgras and Y. Yamauchi, *J Mater Chem A Mater*, 2015, **3**, 18053–18058.
- 175 L. M. Luo, R. H. Zhang, D. Chen, Q. Y. Hu and X. W. Zhou, *ACS Appl Energy Mater*, 2018, **1**, 2619–2629.
- 176 Y. Liu, G. Ren, M. Wang, Z. Zhang, Y. Liang, S. Wu and J. Shen, *J Alloys Compd*, 2019, **780**, 504–511.
- 177 Z. Chen, D. Rao, J. Zhang, Y. Liu, Y. Wang, C. Liu, W. Hu and Y. Deng, *ACS Appl Energy Mater*, 2019, **2**, 4763–4773.
- 178 J. Lan, C. Li, T. Liu and Q. Yuan, *Journal of Saudi Chemical Society*, 2019, **23**, 43–51.
- 179 M. Nie, S. Du, Q. Li, M. Hummel, Z. Gu and S. Lu, *J Electrochem Soc*, 2020, **167**, 044510.



- 180 H. J. Yin, Z. P. Zhang, Y. Guo, K. Yuan and Y. W. Zhang, *Mater Chem Front*, 2020, **4**, 1985–1992.
- 181 C. Liu, Z. Chen, D. Rao, J. Zhang, Y. Liu, Y. Chen, Y. Deng and W. Hu, *Sci China Mater*, 2021, **64**, 611–620.
- 182 Z. Wang, S. Hu, A. Ali, H. Chen and P. K. Shen, *ACS Appl Energy Mater*, 2021, **4**, 1085–1092.
- 183 K. Y. Shih, J. J. Wei and M. C. Tsai, *Nanomaterials*, 2021, **11**, 2206–2222.
- 184 Y. Chen, A. Zohaib, H. Sun and S. Sun, *Chemical Communications*, 2025, **61**, 12097–12114.
- 185 K. Thongthai, P. Pakawanit, N. Chanlek, J. H. Kim, S. Ananta and L. Srisombat, *Nanotechnology*, 2017, **28**, 375602.
- 186 T. Xia, J. Liu, S. Wang, C. Wang, Y. Sun, L. Gu and R. Wang, *ACS Appl Mater Interfaces*, 2016, **8**, 10841–10849.
- 187 F. Gao, Y. Zhang, P. Song, J. Wang, T. Song, C. Wang, L. Song, Y. Shiraishi and Y. Du, *J Mater Chem A Mater*, 2019, **7**, 7891–7896.
- 188 W. Hong, C. Shang, J. Wang and E. Wang, *Energy Environ Sci*, 2015, **8**, 2910–2915.
- 189 H. Xu, B. Yan, K. Zhang, J. Wang, S. Li, C. Wang, Z. Xiong, Y. Shiraishi, Y. Du and P. Yang, *ACS Sustain Chem Eng*, 2017, **5**, 10490–10498.
- 190 L. Wang, H. Meng, P. K. Shen, C. Bianchini, F. Vizza and Z. Wei, *Physical Chemistry Chemical Physics*, 2011, **13**, 2667–2673.
- 191 J. Mao, W. Chen, D. He, J. Wan, J. Pei, J. Dong, Y. Wang, P. An, Z. Jin, W. Xing, H. Tang, Z. Zhuang, X. Liang, Y. Huang, G. Zhou, L. Wang, D. Wang and Y. Li, *Sci Adv*, DOI:10.1126/SCIADV.1603068/SUPPL_FILE/1603068_SM.PDF.
- 192 P. Wang, S. Yin, Y. Wen, Z. Tian, N. Wang, J. Key, S. Wang and P. K. Shen, *ACS Appl Mater Interfaces*, 2017, **9**, 9584–9591.
- 193 K. Bhunia, S. Khilari and D. Pradhan, *ACS Sustain Chem Eng*, 2018, **6**, 7769–7778.
- 194 K. J. Ju, L. Liu, J. J. Feng, Q. L. Zhang, J. Wei and A. J. Wang, *Electrochim Acta*, 2016, **188**, 696–703.
- 195 L. Liu, X. X. Lin, S. Y. Zou, A. J. Wang, J. R. Chen and J. J. Feng, *Electrochim Acta*, 2016, **187**, 576–583.
- 196 Y. Lu, W. Wang, X. Chen, Y. Zhang, Y. Han, Y. Cheng, X. J. Chen, K. Liu, Y. Wang, Q. Zhang and S. Xie, *Nano Res*, 2019, **12**, 651–657.



- 197 J. J. Duan, X. X. Zheng, H. J. Niu, J. J. Feng, Q. L. Zhang, H. Huang and A. J. Wang, *J Colloid Interface Sci*, 2020, **560**, 467–474.
- 198 X. Yang, L. T. Roling, M. Vara, A. O. Elnabawy, M. Zhao, Z. D. Hood, S. Bao, M. Mavrikakis and Y. Xia, *Nano Lett*, 2016, **16**, 6644–6649.
- 199 Z. Zhu, F. Liu, J. Fan, Q. Li, Y. Min and Q. Xu, *ACS Appl Mater Interfaces*, 2020, **12**, 52731–52740.
- 200 Y. Chen, X. X. Zheng, X. Y. Huang, A. J. Wang, Q. L. Zhang, H. Huang and J. J. Feng, *J Colloid Interface Sci*, 2020, **559**, 206–214.
- 201 H. S. Ferreira, M. Gocyla, H. S. Ferreira, R. G. O. Araujo, C. V. S. Almeida, M. Heggen, R. E. Dunin-Borkowski, K. I. B. Eguiluz, P. Strasser and G. R. Salazar-Banda, *J Nanosci Nanotechnol*, 2020, **20**, 6274–6285.
- 202 Z. Wan, X. Bai, H. Mo, J. Yang, Z. Wang and L. Zhou, *Colloids Surf A Physicochem Eng Asp*, 2021, **614**, 126048.
- 203 Y. Wang, K. S. Chen, J. Mishler, S. C. Cho and X. C. Adroher, *Appl Energy*, 2011, **88**, 981–1007.
- 204 K. Scott and A. K. Shukla, *Rev Environ Sci Biotechnol*, 2004, **3**, 273–280.
- 205 K. Wang, H. Chen, X. Zhang, Y. Tong, S. Song, P. Tsiakaras and Y. Wang, *Appl Catal B*, DOI:10.1016/j.apcatb.2019.118468.
- 206 H. Cruz-Martínez, M. M. Tellez-Cruz, O. X. Guerrero-Gutiérrez, C. A. Ramírez-Herrera, M. G. Salinas-Juárez, A. Velázquez-Osorio and O. Solorza-Feria, *Int J Hydrogen Energy*, 2019, **44**, 12477–12491.
- 207 A. Chen and P. Holt-Hindle, *Chem Rev*, 2010, **110**, 3767–3804.
- 208 Y. Kang, J. Snyder, M. Chi, D. Li, K. L. More, N. M. Markovic and V. R. Stamenkovic, *Nano Lett*, 2014, **14**, 6361–6367.
- 209 K. Sasaki, H. Naohara, Y. Choi, Y. Cai, W. F. Chen, P. Liu and R. R. Adzic, *Nature Communications 2012 3:1*, 2012, **3**, 1–9.
- 210 H. Wang, S. Yin, Y. Li, H. Yu, C. Li, K. Deng, Y. Xu, X. Li, H. Xue and L. Wang, *J Mater Chem A Mater*, 2018, **6**, 3642–3648.
- 211 H. Cruz-Martínez, M. M. Tellez-Cruz, H. Rojas-Chávez, C. A. Ramírez-Herrera, P. Calaminici and O. Solorza-Feria, *Int J Hydrogen Energy*, 2019, 12463–12469.



- 212 H. Wang, Y. Li, K. Deng, C. Li, H. Xue, Z. Wang, X. Li, Y. Xu and L. Wang, *ACS Appl Mater Interfaces*, 2019, **11**, 4252–4257.
- 213 X. Li, C. Zhang, C. Du, Z. Zhuang, F. Zheng, P. Li, Z. Zhang and W. Chen, *Sci China Chem*, 2019, **62**, 378–384.
- 214 J. J. Duan, J. J. Feng, L. Zhang, J. Yuan, Q. L. Zhang and A. J. Wang, *Int J Hydrogen Energy*, 2019, **44**, 27455–27464.
- 215 H. M. Alfaro-López, M. A. Valdés-Madrigal, H. Rojas-Chávez, H. Cruz-Martínez, M. A. Padilla-Islas, M. M. Tellez-Cruz and O. Solorza-Feria, *Catalysts*, 2020, **10**, 1–13.
- 216 M. Geethalakshmi, M. Ganeshbabu, D. Kalpana and A. Stephen, *Electrocatalysis*, 2022, **13**, 328–337.
- 217 M. Fu, Q. Zhang, Y. Sun, G. Ning, X. Fan, H. Wang, H. Lu, Y. Zhang and H. Wang, *Int J Hydrogen Energy*, 2020, **45**, 20832–20842.
- 218 V. R. Stamenkovic, D. Strmcnik, P. P. Lopes and N. M. Markovic, *Nature Materials* 2017 16:1, 2016, **16**, 57–69.
- 219 Y. Hou, M. Qiu, M. G. Kim, P. Liu, G. Nam, T. Zhang, X. Zhuang, B. Yang, J. Cho, M. Chen, C. Yuan, L. Lei and X. Feng, *Nat Commun*, 2019, **10**, 1–9.
- 220 A. Eftekhari, *Int J Hydrogen Energy*, 2017, **42**, 11053–11077.
- 221 R. Crețu, A. Kellenberger and N. Vaszilcsin, *Int J Hydrogen Energy*, 2013, **38**, 11685–11694.
- 222 F. Safizadeh, E. Ghali and G. Houlachi, *Int J Hydrogen Energy*, 2015, **40**, 256–274.
- 223 W. Sheng, M. Myint, J. G. Chen and Y. Yan, *Energy Environ Sci*, 2013, **6**, 1509–1512.
- 224 N. Du, C. Wang, X. Wang, Y. Lin, J. Jiang and Y. Xiong, *Advanced Materials*, 2016, **28**, 2077–2084.
- 225 W. Dong, H. Zhou, B. Mao, Z. Zhang, Y. Liu, Y. Liu, F. Li, D. Zhang, D. Zhang and W. Shi, *Int J Hydrogen Energy*, 2021, **46**, 10773–10782.
- 226 K. S. Bhat and H. S. Nagaraja, *Int J Hydrogen Energy*, 2018, **43**, 19851–19863.
- 227 A. Paksoy, S. F. Kurtoğlu, A. K. Dizaji, Z. Altıntaş, S. Khoshshima, A. Uzun and Ö. Balci, *Int J Hydrogen Energy*, 2021, **46**, 7974–7988.
- 228 Z. Zhao, J. Zhao, H. Wang, X. Li, L. Yang, Z. Zhao, X. Liu, Y. Liu, P. Liu and Z. Cai, *Int J Hydrogen Energy*, 2020, **45**, 14199–14207.
- 229 L. Fu, G. Cheng and W. Luo, *J Mater Chem A Mater*, 2017, **5**, 24836–24841.



- 230 M. Smiljanić, Z. Rakočević and S. Štrbac, *Int J Hydrogen Energy*, 2018, **43**, 2763–2771.
- 231 F. Qin, Z. Zhao, M. K. Alam, Y. Ni, F. Robles-Hernandez, L. Yu, S. Chen, Z. Ren, Z. Wang and J. Bao, *ACS Energy Lett*, 2018, **3**, 546–554.
- 232 H. Y. Chen, A. J. Wang, L. Zhang, J. Yuan, Q. L. Zhang and J. J. Feng, *Int J Hydrogen Energy*, 2018, **43**, 22187–22194.
- 233 Z. Zhang, L. Cong, Z. Yu, L. Qu, M. Qian and W. Huang, *Mater Adv*, 2020, **1**, 54–60.
- 234 H. Fan, W. Chen, G. Chen, J. Huang, C. Song, Y. Du, C. Li and K. (Ken) Ostrikov, *Appl Catal B*, 2020, **268**, 118440.
- 235 S. Li, Q. Zhang, J. Sun and J. Guan, *Mater Today Energy*, 2020, **17**, 100464.
- 236 G. Wang, W. Chen, G. Chen, J. Huang, C. Song, D. Chen, Y. Du, C. Li and K. K. Ostrikov, *Nano Energy*, 2020, **71**, 104637.
- 237 Q. Zhang, W. Chen, G. Chen, J. Huang, C. Song, S. Chu, R. Zhang, G. Wang, C. Li and K. K. Ostrikov, *Appl Catal B*, 2020, **261**, 118254.
- 238 H. Y. Chen, H. J. Niu, Z. Han, J. J. Feng, H. Huang and A. J. Wang, *J Colloid Interface Sci*, 2020, **570**, 205–211.
- 239 Z. Li, G. Qiu, Y. Shen, X. Wang, W. Zhuang, J. Li, M. Song, P. Wang and L. Tian, *J Alloys Compd*, 2020, **820**, 153161.
- 240 M. Khalid, A. M. B. Honorato, G. Tremiliosi Filho and H. Varela, *J Mater Chem A Mater*, 2020, **8**, 9021–9031.
- 241 S. Ren, X. Duan, F. Ge, M. Zhang and H. Zheng, *J Power Sources*, 2020, **480**, 228866.
- 242 W. Yaseen, N. Ullah, M. Xie, B. A. Yusuf, Y. Xu, C. Tong and J. Xie, *Surfaces and Interfaces*, 2021, **26**, 101361.
- 243 Z. Yang, X. Ren, K. Guo, F. Shaik and B. Jiang, *Int J Hydrogen Energy*, 2021, **46**, 35559–35570.
- 244 N. T. Suen, S. F. Hung, Q. Quan, N. Zhang, Y. J. Xu and H. M. Chen, *Chem Soc Rev*, 2017, **46**, 337–365.
- 245 T. Reier, M. Oezaslan and P. Strasser, *ACS Catal*, 2012, **2**, 1765–1772.
- 246 A. Khan, I. Khan, M. Y. Khan, H. Dafallah and A. Qurashi, *Int J Hydrogen Energy*, 2020, **45**, 24045–24053.



- 247 C. L. Huang, X. F. Chuah, C. T. Hsieh and S. Y. Lu, *ACS Appl Mater Interfaces*, 2019, **11**, 24096–24106.
- 248 A. Rebekah, E. Ashok Kumar, C. Viswanathan and N. Ponpandian, *Int J Hydrogen Energy*, 2020, **45**, 6391–6403.
- 249 C. Panda, P. W. Menezes, M. Zheng, S. Orthmann and M. Driess, *ACS Energy Lett*, 2019, **4**, 747–754.
- 250 G. Fu and J. M. Lee, *J Mater Chem A Mater*, 2019, **7**, 9386–9405.
- 251 Z. Fang, L. Peng, H. Lv, Y. Zhu, C. Yan, S. Wang, P. Kalyani, X. Wu and G. Yu, *ACS Nano*, 2017, **11**, 9550–9557.
- 252 A. M. Smith, L. Trotochaud, M. S. Burke and S. W. Boettcher, *Chemical Communications*, 2015, **51**, 5261–5263.
- 253 Z. Xue, X. Li, Q. Liu, M. Cai, K. Liu, M. Liu, Z. Ke, X. Liu and G. Li, *Advanced Materials*, 2019, **31**, 1900430.
- 254 X. Zhang, L. Zhang, G. G. Zhu, Y. X. Zhu and S. Y. Lu, *ACS Appl Mater Interfaces*, 2020, **12**, 7153–7161.
- 255 Y. J. Tang, C. H. Liu, W. Huang, X. L. Wang, L. Z. Dong, S. L. Li and Y. Q. Lan, *ACS Appl Mater Interfaces*, 2017, **9**, 16977–16985.
- 256 Y. Yang, L. Dang, M. J. Shearer, H. Sheng, W. Li, J. Chen, P. Xiao, Y. Zhang, R. J. Hamers and S. Jin, *Adv Energy Mater*, 2018, **8**, 1–9.
- 257 F. Wang, J. Qiao, J. Wang, H. Wu, Z. Wang, W. Sun and K. Sun, *J Alloys Compd*, 2019, **811**, 151882.
- 258 M. Lu, Y. Li, Y. Wu, H. Xu, J. Gao and S. Xu, *ChemNanoMat*, 2020, **6**, 1496–1501.
- 259 Z. Li, L. Cai, M. Song, Y. Shen, X. Wang, J. Li, J. Wang, P. Wang and L. Tian, *Electrochim Acta*, 2020, **339**, 135886.
- 260 M. Khodabakhshi, S. Chen, T. Ye, H. Wu, L. Yang, W. Zhang and H. Chang, *ACS Appl Mater Interfaces*, 2020, **12**, 36268–36276.
- 261 D. Senthil Raja, C. L. Huang, Y. A. Chen, Y. M. Choi and S. Y. Lu, *Appl Catal B*, 2020, **279**, 119375.
- 262 D. Kim, J. Kang, B. Yan, K. dong Seong and Y. Piao, *ACS Sustain Chem Eng*, 2020, **8**, 2843–2853.



- 263 W. Da Zhang, H. Yu, T. Li, Q. T. Hu, Y. Gong, D. Y. Zhang, Y. Liu, Q. T. Fu, H. Y. Zhu, X. Yan and Z. G. Gu, *Appl Catal B*, 2020, **264**, 118532.
- 264 D. Liu, H. Ai, J. Li, M. Fang, M. Chen, D. Liu, X. Du, P. Zhou, F. Li, K. H. Lo, Y. Tang, S. Chen, L. Wang, G. Xing and H. Pan, *Adv Energy Mater*, 2020, **10**, 1–9.
- 265 B. Wang, Y. Chen, X. Wang, J. Ramkumar, X. Zhang, B. Yu, D. Yang, M. Karpuraranjith and W. Zhang, *J Mater Chem A Mater*, 2020, **8**, 13558–13571.
- 266 S. Ramakrishnan, J. Balamurugan, M. Vinothkannan, A. R. Kim, S. Sengodan and D. J. Yoo, *Appl Catal B*, 2020, **279**, 119381.
- 267 W. Zhou, Z. Xue, Q. Liu, Y. Li, J. Hu and G. Li, *ChemSusChem*, 2020, **13**, 5647–5653.
- 268 H. Mao, X. Guo, Y. Fu, H. Yang, Y. Zhang, R. Zhang and X. M. Song, *J Mater Chem A Mater*, 2020, **8**, 1821–1828.
- 269 X. Du, J. Guo, M. Chen, W. C. Cheong, Y. Chen, D. Liu, S. Chen, X. Wang, K. Ho Lo, J. S. Hu and H. Pan, *Chemical Engineering Journal*, DOI:10.1016/j.cej.2021.131662.
- 270 S. P. Keerthana, B. J. Rani, R. Yuvakkumar, G. Ravi, Y. Shivatharsiny, E. S. Babu, H. S. Almoallim, S. A. Alharbi and D. Velauthapillai, *Int J Hydrogen Energy*, 2021, **46**, 7701–7711.
- 271 Y. Wang, R. Zhu, Z. Wang, Y. Huang and Z. Li, *J Alloys Compd*, 2021, **880**, 160523.
- 272 S. Chen, C. Yu, Z. Cao, X. Huang, S. Wang and H. Zhong, *Int J Hydrogen Energy*, 2021, **46**, 7037–7046.
- 273 Y. Huang, S. L. Zhang, X. F. Lu, Z. Wu, D. Luan and X. W. (David) Lou, *Angewandte Chemie*, 2021, **133**, 11947–11952.
- 274 S. S. Sankar, K. Manjula, G. Keerthana, B. Ramesh Babu and S. Kundu, *Cryst Growth Des*, 2021, **21**, 1800–1809.
- 275 S. Gopi, S. Perumal, E. M. Al Olayan, O. D. AlAmri, A. S. Aloufi, M. Kathiresan and K. Yun, *Chemosphere*, DOI:10.1016/j.chemosphere.2020.129243.
- 276 R. Venkatkarthick, J. Niu, A. Sriksaow, C. Sriprachuabwong, S. Vasudevan, A. Tuantranont and J. Qin, *ACS Appl Energy Mater*, 2021, **4**, 6520–6530.
- 277 M. Ishaq, M. Jabeen, W. Song, L. Xu, W. Li and Q. Deng, *Electrochim Acta*, 2018, **282**, 913–922.
- 278 C. Chen, S. C. Wang, D. Xiong, M. Gu and F. Y. Yi, *Dalton Transactions*, 2020, **49**, 3706–3714.
- 279 X. Zhao, Q. Bi, C. Yang, K. Tao and L. Han, *Dalton Transactions*, 2021, **50**, 15260–15266.



- 280 J. Zhang, C. Li, M. Fan, T. Ma, H. Chen and H. Wang, *Appl Surf Sci*, 2021, **565**, 150482.
- 281 S. Thakur, S. Maiti, K. Sardar, N. Besra, P. Bairi, K. Panigrahi, K. Chanda, T. Paul and K. K. Chattopadhyay, *J Energy Storage*, 2021, **35**, 102249.
- 282 A. Alshoaibi, C. Awada, F. Ahmed, R. M. Obodo, M. Maaza and F. I. Ezema, *Crystals (Basel)*, DOI:10.3390/cryst12060874.
- 283 B. Han, M. Pan, J. Zhou, Y. Wang, Z. Wang, J. Jiao, C. Zhang and Q. Chen, *Nanomaterials*, DOI:10.3390/nano8090724.
- 284 W. Dong, Y. Ren, Z. Bai, Y. Yang, Z. Wang, C. Zhang and Q. Chen, *Talanta*, 2018, **189**, 79–85.
- 285 Y. Shi, H. Xu, J. Wang, S. Li, Z. Xiong, B. Yan, C. Wang and Y. Du, *Sens Actuators B Chem*, 2018, **272**, 135–138.
- 286 S. C. Barman, M. F. Hossain, H. Yoon and J. Y. Park, *Biosens Bioelectron*, 2018, **100**, 16–22.
- 287 M. Annalakshmi, P. Balasubramanian, S. M. Chen and T. W. Chen, *Sens Actuators B Chem*, 2019, **296**, 126620.
- 288 S. A. Alkahtani, M. M. El-Wakil, A. M. Mahmoud, M. H. Mahnashi and M. Oraby, *J Electrochem Soc*, 2019, **166**, H521–H526.
- 289 L. Fan, Y. Yan, B. Guo, M. Zhao, J. Li, X. Bian, H. Wu, W. Cheng and S. Ding, *Sens Actuators B Chem*, 2019, **296**, 126697.
- 290 X. Ye, X. He, Y. Lei, J. Tang, Y. Yu, H. Shi and K. Wang, *Chemical Communications*, 2019, **55**, 2321–2324.
- 291 Md. Sharifuzzaman, S. C. Barman, M. T. Rahman, Md. A. Zahed, X. Xuan and J. Y. Park, *J Electrochem Soc*, 2019, **166**, B983–B993.
- 292 F. Salman, H. C. Kazici and H. Kivrak, *Front Chem Sci Eng*, 2020, **14**, 629–638.
- 293 Md. Sharifuzzaman, S. C. Barman, Md. A. Zahed, N. J. San and J. Y. Park, *J Electrochem Soc*, 2019, **166**, B249–B257.
- 294 F. Nie, L. Ga, J. Ai and Y. Wang, *Front Chem*, 2020, **8**, 1–10.
- 295 A. A. Abdelwahab, A. M. Elseman, N. F. Alotaibi and A. M. Nassar, *Microchemical Journal*, 2020, **156**, 104927.
- 296 P. Wu, S. Li, X. Ye, B. Ning, J. Bai, Y. Peng, L. Li, T. Han, H. Zhou, Z. Gao and P. Ding, *Anal Chim Acta*, 2020, **1134**, 96–105.



- 297 E. Ma, P. Wang, Q. Yang, H. Yu, F. Pei, Y. Zheng, Q. Liu, Y. Dong and Y. Li, *ACS Biomater Sci Eng*, 2020, **6**, 1418–1427.
- 298 J. Chen, G. Cheng, K. Wu, A. Deng and J. Li, *Electrochim Acta*, 2020, **361**, 137061.
- 299 M. A. Subhan, P. Chandra Saha, J. Ahmed, A. M. Asiri, M. Al-Mamun and M. M. Rahman, *Mater Adv*, 2020, **1**, 2831–2839.
- 300 E. Han, Y. Zhang, J. Cai and X. Zhang, *Micromachines (Basel)*, DOI:10.3390/mi12040446.
- 301 S. Y. Cen, X. Y. Ge, Y. Chen, A. J. Wang and J. J. Feng, *Microchemical Journal*, 2021, **169**, 106568.
- 302 S. Akhter, N. K. Mohd Zain, M. Shalauddin, V. K. Singh, I. I. Misnon, R. K. Sharma, S. Das, W. J. Basirun, M. R. Johan and R. Jose, *Sens Actuators A Phys*, 2021, **325**, 112711.
- 303 W. Zhang, G. Sharma, A. Kumar, M. I. Shekh and F. J. Stadler, *Mater Today Commun*, 2021, **29**, 102726.
- 304 B. Zhang, N. She, J. Du, M. Zhang, G. Fang and S. Wang, *Ecotoxicol Environ Saf*, 2021, **207**, 111251.
- 305 N. Toshima, R. Ito, T. Matsushita and Y. Shiraishi, *Catal Today*, 2007, **122**, 239–244.
- 306 N. Toshima, *Macromol Symp*, 2008, **270**, 27–39.
- 307 NiFe-LDH as a bifunctional electrocatalyst for efficient water and seawater electrolysis: enhanced oxygen evolution and hydrogen evolution reactions - *Nanoscale Advances* (RSC Publishing) DOI:10.1039/D5NA00350D, <https://pubs.rsc.org/en/content/articlehtml/2025/na/d5na00350d>, (accessed 2 December 2025).
- 308 Q. Li, W. Zhang, J. Shen, X. Zhang, Z. Liu and J. Liu, *J Alloys Compd*, 2022, **902**, 163670.
- 309 M. Pratheeksha, H. Nj, S. Dongre S, S. K. Sahoo, R. G. Balakrishna and R. Shwetharani, *EnFue*, 2025, **39**, 6930–6941.
- 310 M. Luo, J. Yang, X. Li, M. Eguchi, Y. Yamauchi and Z. L. Wang, *Chem Sci*, 2023, **14**, 3400–3414.
- 311 B. Guo, Y. Ding, H. Huo, X. Wen, X. Ren, P. Xu and S. Li, *Nano-Micro Letters* 2023 **15**:1, 2023, **15**, 57-.
- 312 F. Qin, Z. Zhao, M. K. Alam, Y. Ni, F. Robles-Hernandez, L. Yu, S. Chen, Z. Ren, Z. Wang and J. Bao, *ACS Energy Lett*, 2018, **3**, 546–554.
- 313 M. Ruan, J. Liu, P. Song and W. Xu, *Chinese Journal of Catalysis*, 2022, **43**, 116–121.



- 314 H. Ma, Z. Zheng, H. Zhao, C. Shen, H. Chen, H. Li, Z. Cao, Q. Kuang, H. Lin and Z. Xie, *J Mater Chem A Mater*, 2021, **9**, 23444–23450.
- 315 Y. Zhou, R. Abazari, J. Chen, M. Tahir, A. Kumar, R. R. Ikreedeegh, E. Rani, H. Singh and A. M. Kirillov, *Coord Chem Rev*, 2022, **451**, 214264.
- 316 Y. Shi, D. Zhang, H. Miao, T. Zhan and J. Lai, *Electrochemical Science Advances*, 2022, **2**, e2100052.
- 317 A. Wang, Y. Ma and D. Zhao, *ACS Nano*, 2024, **18**, 22829–22854.
- 318 S. Hagos Gebre and M. Getaye Sendeku, *Journal of Energy Chemistry*, 2022, **65**, 329–351.
- 319 M. Godara, S. Chowdhury, P. Cheng, R. Xin, B. Yulianto, Y. Yamauchi, Y. V. Kaneti and N. Ray, *Advanced Energy and Sustainability Research*, 2025, **6**, 2300301.
- 320 H. P. Dang, L. Tran, L. H. Bao and H. N. T. Le, *RSC Adv*, 2025, **15**, 14463–14476.
- 321 Y. T. Pan and H. Yang, *Nano Today*, 2020, **31**, 100832.
- 322 G. Sharma, D. Kumar, A. Kumar, A. H. Al-Muhtaseb, D. Pathania, M. Naushad and G. T. Mola, *Materials Science and Engineering: C*, 2017, **71**, 1216–1230.
- 323 J. Guo, Y. Haghshenas, Y. Jiao, P. Kumar, B. I. Yakobson, A. Roy, Y. Jiao, K. Regenauer-Lieb, D. Nguyen and Z. Xia, *Advanced Materials*, 2024, **36**, 2407102.
- 324 S. Kaushal, P. Pal Singh and N. Kaur, *Environ Nanotechnol Monit Manag*, 2022, **18**, 100727.
- 325 Z. Fang, C. Peng, Q. Zhou and Z. Liu, *The Chemical Record*, 2025, **25**, e202500066..
- 326 Y. Li, J. Bu, Y. Sun, Z. Huang, X. Zhu, S. Li, P. Chen, Y. Tang, G. He and S. Zhong, *Sep Purif Technol*, 2025, **356**, 129945.
- 327 G. Wang, A. Chen, Y. Chen, F. Qiao, J. Wang, N. Yang, H. Zhang and Z. Wen, *eScience*, 2025, **5**, 100333.
- 328 T. Ramachandran, R. K. Raji and M. Rezeq, *J Mater Chem A Mater*, 2025, **13**, 12855–12890.
- 329 T. Ramachandran, F. Hamed, Y. A. Kumar, R. K. Raji and H. H. Hegazy, *J Energy Storage*, 2023, **73**, 109299.
- 330 T. Ramachandran, F. Hamed, R. K. Raji, S. M. Majhi, D. Barik, Y. A. Kumar, R. M. Jauhar, M. P. Pachamuthu, L. Vijayalakshmi and S. Ansar, *Journal of Physics and Chemistry of Solids*, 2023, **180**, 111467.



Electrocatalytic Advancements with Trimetallic Nanoparticles: Design Strategies and Roadmap

[View Article Online](#)

DOI: 10.1039/D5NA00936G

Sonali Garg^{a†}, Aafreen Nakai^{b†}, Rijo Rajeev^{b*}, Anitha Varghese^{b*}, Manvinder Kaur^{ac*}

^aDepartment of Chemistry, Chandigarh University, Gharuan, Punjab-140413, India

^bDepartment of Chemistry, CHRIST University Bangalore, Karnataka- 560029, India

^cChitkara University Institute of Engineering and Technology, Chitkara University, Rajpura-140401, Punjab, India

[†] Equally contributed to the manuscript

Data availability

All data supporting the findings of this study are available within the article.

